Thesis

A Study on the Electronic Structures and the Fermi Surfaces of the Rare-Earth and Actinide Materials via a Relativistic Linear Augmented-Plane-Wave Method

Masahiko Higuchi

Course of Industrial Science
Graduate School of Science and Technology
Niigata University

Contents

1. Introduction

Some of the rare-earth and actinide compounds form the heavy-electron system or the strongly-correlated-electron system, and their anomalous physical properties have been studied both theoretically and experimentally. The Heavy-electron metals exhibit local moment behavior at high temperatures, but at low temperatures they have the very large electronic specific heat linear in T which corresponds to the large Pauli-like susceptibility. The observed value of the electronic specific heat coefficient is two to three orders of magnitude larger than that of usual metals. This means that the effective mass becomes far heavier than the free-electron mass, which is the origin of a term " heavy-electron ". One of the most attractive features in the heavy-electron system is the rich variety of different types of the ground states, i.e. Fermi liquid state, ferromagnetism, antiferromagnetism and superconductivity (Lee *et al.* 1986). It is obvious that these characteristic properties originate from the existence of the *f* electrons which are inherent in the rare-earth and actinide atoms. The *f* electrons in the rare-earth and actinide compounds exist under the delicate condition where they are itinerant or localized (or mixed valent[1]). The nature of the *f* electrons influences all of the physical properties including anomalies in the heavy-electron system. Therefore, in order to reveal the origin of its anomalies, it is necessary to study on the nature of the *f* electrons. Especially, the studies on the electronic band structure and the Fermi surface can play a basic role on better understanding of the electronic states in the heavy-electron system.

Efforts of this thesis focus on the investigation of the electronic states for the *f* electrons in the rare-earth and actinide materials by using a relativistic band theory. Moreover, by comparing our calculated results

[1] This concept has been suggested by several workers, but it is different from our point of view, i.e. on the band theory picture, the *f* electrons are treated as completely itinerant or completely localized .

with the de Haas-van Alphen (dHvA) effect experiments, we examine what a relativistic band theory within the local-density approximation (LDA) can say about the nature of the *f* electrons in these systems.

The energy band structure and the Fermi surface for the *f*-electron compound are generally complicated, because its *f* bands lie in the vicinity of the Fermi energy and have very flat dispersion. Furthermore, not a few *f*-electron compounds have the complicated crystal structures. Therefore the method of the band calculation for the *f*-electron compounds should be improved so as to perform more stably and more rapidly.

The standard augmented-plane-wave (APW) method has been originally proposed by Slater (1937). In this method, the muffin-tin approximation (MTA) is adopted. There are two major difficulties in computations, i.e. one is the energy dependence of the Hamiltonian and overlap matrices, and the other is the singular behavior of the secular equation which occurs when a node of the radial solution falls at the boundary of the muffin-tin sphere.[2] Furthermore, the basis functions of the original APW method have discontinuous slope across the boundary of the muffin-tin sphere, which is apparently an unphysical property. In order to overcome these difficulties, several authors have proposed linearized methods as an improvement on the APW method. Such linearized methods are called the linear augmented-plane-wave (LAPW) method. Marcus (1967) proposed to employ the radial wave function and its energy derivative for the expansion inside the muffin-tin sphere. Andersen (1975), as well as Koelling and Arbman (1979), successfully implemented this scheme. This simple inclusion of an additional energy derivative could eliminate two major difficulties and one minor one. Instead of the wave function and its energy derivative, Takeda and Kubler (1979) introduced two or more energy-independent wave

---

[2] For the detailed explanations, see, Mattheiss *et al.* (1968).

functions which are the solutions belonging to given energies of the Schrodinger equation. The formulation of this LAPW method also results in the elimination of the difficulties, like the former LAPW method which is accompanied with the energy derivative. It is shown that the LAPW method of Andersen (1975) or that of Koelling and Arbman (1979) can be obtained in a special limit from the formulation of Takeda and Kubler (1979).

As for the relativistic calculations, Loucks (1967) derived a relativistic augmented-plane-wave (RAPW) method which is based on the Dirac equation. This method makes it possible to take the relativistic effects fully into account in the energy band, i.e. the relativistic energy shifts, the relativistic screening effects and the spin-orbit interaction. More useful expressions to perform the calculation were given by Dimmock (1971). Yamagami and Hasegawa (1990) improved Loucks' RAPW method by incorporating the symmetrization with double space groups and a self-consistent calculation. This method has been applied to many rare-earth compounds and some actinide compounds, and consequently its reliability has been verified (Hasegawa 1993, Hasegawa and Yamagami 1992, Yamagami 1991).

As in the nonrelativistic case, the RAPW method has also some difficulties in computations because the exact solution of the Dirac equation which corresponds to the true eigenvalue is used as the basis function, i.e. the matrix elements become inevitably dependent on the true eigenvalue. Although this property assures the high accuracy of the eigenvalues, they should be determined by finding zeros of the RAPW determinant. As an approximate method of the RAPW method, Andersen (1975) also has suggested a linearized technique containing the relativistic effects. This method is based on the usage of the solutions belonging to given energies of the Schrodinger equation as the

basis function. The relativistic effects are treated as the Pauli approximation, i.e. the Dirac Hamiltonian is linearized with respect to the spin-orbit interaction. MacDonald *et al.* (1980) have practically implemented the Koelling-Harmon method (Koelling and Harmon 1977) for the central-field Dirac equation, which is the relativistic version for the Koelling and Arbman linearized APW band structure method (Koelling and Arbman 1975). But, in this method, the spin-orbit interaction is treated as a perturbation. Yanase and Harima (1992) have proposed another relativistic LAPW method, but neither it exceeds the perturbation theory. It is not sufficient to treat the relativistic effects within the perturbation theory, as is shown in Chapter 2 in this thesis. In order to consider the relativistic effects fully, Takeda (1978, 1979) has extended the LAPW method of Takeda and Kubler (1979) to a relativistic case. Similar to the nonrelativistic method of Takeda and Kubler (1979), this method relies on the fact that the four-component relativistic APW basis function can be represented reasonably well by a linear combination of the solutions of the Dirac equation for two energy values which are chosen appropriately within a limited range of energy. The augmentation is applied to both large and small components of the wave functions defined both inside and outside the muffin-tin spheres. The secular equation is derived directly from the Dirac Hamiltonian, so that the relativistic effects can be fully taken into account. The theory proposed by Takeda (1979) seems to be one of the promising methods for the calculations of electronic structures in the *f*-electron compounds. But his formulation is feasible only for the monoatomic metals, and its efficiency has not been confirmed by any actual applications.

In this thesis, Loucks' RAPW method is converted into a linear form by the relativistic band theory of Takeda (1979) in order to obtain an efficient method for calculating the electronic structures including the *f*

bands in the rare-earth and the actinide materials with complex crystal structures (Higuchi and Hasegawa 1995). This relativistic LAPW (RLAPW) method is quite stable because the matrix elements are independent of the eigenvalues, while the RAPW method is apt to miss the eigenvalues unless zeros of the RAPW determinants are searched very carefully. Especially, though the eigenvalues in the *f* bands generally crowd in a narrow range of energy, the RLAPW method can perform well the calculations of the energy band structure in the *f*-electron compounds. In addition, the eigenvalues can be calculated with much less CPU time of a computer by the RLAPW method than by the RAPW method, because it is not necessary to evaluate the secular determinant for a set of discrete energies. Although the RLAPW method is an approximate method of the RAPW method, it has also been confirmed that the accuracy of the solutions in the RLAPW method can be kept within 1 mRyd. as compared with the solutions in the RAPW method. These properties of the RLAPW method are of great advantage to the determination of the Fermi surface because it requires the calculation of energies at a number of general $\boldsymbol{k}$ points in the Brillouin zone. Throughout this thesis, the RLAPW method will be proved to be one of the promising methods for the calculations of the *f*-electron materials.

It has recently been clarified that the Ce compounds are classified into three groups, i.e. usual metals, the valence fluctuation regime and the Kondo regime.[3] The Ce compounds in the valence fluctuation regime, such as $CeSn_3$, CeNi, etc., have no magnetic order and behave like the Pauli paramagnet with its large susceptibility at low temperatures. The

---

[3] For instance, see, *Proceedings of the Yamada Conference XXV on Magnetic Phase Transitions*, ed. M. Date, K. Nagata, Y. Miyako and K. Komatsubara (Elsevier Science Publishers B. V. and Yamada Science Foundation, 1990) [J. Magn. Magn. Mater. **90&91** (1990)].

theoretical Fermi surface calculated on the basis of the itinerant-electron model for the 4*f* electrons explains well the experimental results for the dHvA effect except for the cyclotron effective mass, and the Fermi surface is apparently different from that of La compounds which are the reference materials having the same crystal structure but no 4*f* electrons. On the other hand, the Ce compounds in the Kondo regime, such as CeB_6, CeSb, etc., have a magnetic order and the 4*f* electrons are localized at each Ce ion. Their Fermi surfaces look similar to those of the La compounds which have the same crystal structure.

$CeSn_3$, CeNi, $CeRu_2Si_2$, $CeCu_6$ and $CeRh_2$ are the typical paramagnetic Ce compounds. Their energy band structure, especially the Fermi surface, has recently been investigated by band theories and the dHvA experiments. As a result of careful investigations both on theoretical and experimental sides, it has been shown that the 4*f* electrons in $CeSn_3$ and CeNi are itinerant and contribute directly to the formation of the Fermi surface (Hasegawa *et al.* 1990, Hasegawa and Yamagami 1991, Hasegawa *et al.* 1993, Yamagami and Hasegawa 1991b, Umehara *et al.* 1990a, Umehara *et al.* 1990b, Onuki *et al.* 1989, Maesawa *et al.* 1989). Especially in $CeSn_3$, both the magnitude and the angle dependence of the major experimental dHvA frequency branches have been explained well with the theoretical Fermi surface calculated by the self-consistent RAPW method in the LDA. As for $CeRu_2Si_2$, recent studies strongly suggested that the 4*f* electrons in $CeRu_2Si_2$ may be itinerant (Zwicknagl 1992, Yamagami and Hasegawa 1992, 1993, Onuki *et al.* 1992). Though $CeCu_6$ has also been investigated extensively by band theory and the dHvA effect experiments (Chapman *et al.* 1990), the agreement between theory and experiment is not so good that the itinerant nature for 4*f* electrons in $CeCu_6$ cannot be concluded. As is described in Chapter 4, it is shown that most of the details of the Fermi surface of $CeRh_2$ surface can also be

explained by the RLAPW calculation which treats the *f* electrons as the Bloch electrons and is based on the LDA (Higuchi *et al.* 1994a, Sugawara *et al.* 1994).

As the typical compounds in the Kondo regime, CeSb (Kitazawa *et al.* 1983, Kasuya *et al.* 1987, Settai *et al.* 1993), $CeAl_2$ (Lonzarich 1988, Guo 1990), $CeGa_2$ (Umehara *et al.* 1991), CeB_6 (Komatsubara *et al.* 1983) etc. are notable. Since the Fermi surface of these compounds has been found to look like those of La compounds, the studies on these Ce compounds have been based on the localized-electron model for the 4*f* electrons.

Like the Ce compounds, some Yb compounds are known to exhibit the heavy-electron states at low temperatures (Maple *et al.* 1982). It is apparent that the 4*f* electrons in the Yb compounds play an essential role on their physical properties like the Ce compounds, so that it seems to be appropriate to start from the two limited cases where the 4*f* electrons are treated as the itinerant electrons or the localized ones. On the basis of the itinerant-electron model for the 4*f* electrons, the 4*f* bands in the Yb compounds may lie just below the Fermi energy. As a result, some amount of holes having the strong *f* character may exist in the 4*f* bands through the hybridization between the *f* bands and the other conduction bands. On the basis of the localized-electron model for the 4*f* electrons, the 4*f* electrons may not contribute directly to the formation of the Fermi surface, but affect it indirectly and weakly. As the first step toward the understanding of the nature of the 4*f* electrons in Yb compounds, we calculate the energy bands and the Fermi surface for $YbGa_2$ on the basis of the itinerant-electron model for the 4*f* electrons. It is expected that the hybridization between the Yb 4*f* states and the other Bloch states may be strong enough for the 4*f* electrons to be itinerant in

$YbGa_2$. In Chapter 5, the results for $YbGa_2$ is explained in detail (Higuchi and Hasegawa 1995a).

La is the first element of the rare-earth series, and a neutral La atom has no 4*f* electrons. However, in the La compounds, the 4*f* bands lie above the Fermi level and may affect the Fermi surface through the hybridization with the other states. Thus a careful investigation of the Fermi surface of the La compounds serves for a deeper understanding of the nature of the 4*f* electrons in the rare-earth materials. Moreover, in order to understand the properties of the Ce compounds, it is important to investigate the properties of the La compounds which are the reference materials having the same crystal structure as the Ce compounds but no 4*f* electrons (Hasegawa 1993). In Chapter 6, the Fermi surface and electronic structures for LaAg which is one of the interesting La compounds are described (Nikch *et al.* 1987, Motoki *et al.* 1995, Higuchi and Hasegawa 1995b).

The actinide compounds have been studied actively, and the most of attention has been directed to the uranium compounds. As for the uranium compounds which have no magnetic order and behave like the Pauli paramagnet, UGe_3 (Hasegawa 1984, Arko and Koelling 1978), UIr_3 (Arko *et al.* 1985), URh_3 (Arko *et al.* 1985), UC (Hasegawa and Yamagami 1990, Onuki *et al.* 1990a) and UB_{12} (Yamagami and Hasegawa 1991, Onuki *et al.* 1990b) are well known. Their energy band structure and the Fermi surface have been investigated by band theory and the dHvA effect experiment, and, as a result, the 5*f* electrons in these paramagnetic uranium compounds are shown to be completely itinerant in the ground state. However, many of the uranium compounds exhibit the local magnetic moment behavior. The nature of the 5*f* electrons in these uranium compounds with the magnetic order has been hardly understood. More recently, new phenomena related to the

superconductivity and magnetism have been observed, especially in the uranium compounds such as UPt_3 (Hayden *et al.* 1992), UPd_2Al_3 etc. (Inada *et al.* 1994). These phenomena are quite different from those in the compounds containing transition elements of the iron group, i.e. iron, nickel, copper etc., and some new concepts of the condensed matter physics sould be established. Since new phenomena found in the actinide compounds seem to be ascribed to the behavior of the 5*f* electrons, it is necessary to study the nature of the 5*f* electrons both experimentally and theoretically. As a first step toward a deep understanding of the nature of the 5*f* electrons in the actinide compounds, we try to investigate the electronic structure and the Fermi surface for Th-metal in detail by using the RLAPW method (Higuchi *et al.* 1994b). A careful investigation of the Fermi surface of Th-metal is instructive because thorium is located at the beginning of the actinide series, and has no 5*f* electrons. Our results of Th-metal are shown in Chapter 7.

The organization of this thesis is as follows. In Chapter 2, the relativistic effects on the *f* electrons in the rare-earth and actinide atoms are studied, and especially it is systematically studied how they change according to the atomic number. In Chapter 3, the self-consistent RLAPW method is described in a self-contained form for the calculation of the electronic structures of the *f*-electron compounds. In the subsequent chapters, we apply the RLAPW method to the *f* electron compounds in order to confirm its efficiency. In Chapter 4, the electronic structure and the Fermi surface for $CeRh_2$ which is one of the heavy-electron compound are explained. The corresponding reference compound $LaRh_2$ is also discussed. In Chapter 5, a band picture for the 4*f* electrons in $YbGa_2$ are explained. In Chapter 6, the electronic structure and the Fermi surface for LaAg are explained and the curvature factors of the Fermi surface are discussed in detail. In Chapter 7, effects of the 5*f* electrons on the Fermi

surface of Th-metal, especially the extremal cross section of the Fermi surface are investigated. Finally a conclusion is given in Chapter 8.

2. Electronic States in the Rare-earth and the Actinide Atoms

2.1. *Introduction*

In order to understand the electronic structure for a crystal, it is generally important to examine the electronic properties of the constituent atoms. Actually, the charge densities determined by the atomic charge densities serve as a good starting point for the self-consistent calculation for a crystal. In this chapter, we explain the properties of the *f* electrons in the neutral rare-earth and actinide atoms, which is obtained by a relativistic atomic theory in LDA. The relativistic effects on the *f* electrons in the rare-earth and actinide atoms are systematically studied with emphasis on their variation with the atomic number.

As is well known, in the hydrogen atom the ratio of the velocity of an electron in the ground state to the velocity of light, v/c, is equal to the fine structure constant α (=1/137). According to a simple Bohr model, in the atom with the atomic number Z the ratio of the velocity of an electron in the most inner orbit (the K-shell) to the velocity of light is equal to $Z\alpha$. Therefore, for example, the velocity of the K-shell electron in the uranium atom (Z=92) reaches 67% of the velocity of light. Since the Coulomb attraction due to the nucleus is proportional to Z, the electrons nearby the heavy nucleus suffer a strong attractive force and must move with a high speed in order to keep their stationary motion. This means that the relativistic ellects on the inner electrons in an atom having the larger Z become the more important. According to the special theory of relativity, it is expected that the energy levels of these inner electrons may decrease and their orbital radii may contract.

At first sight, it may appear that the relativistic corrections are required only for the inner electrons, because they have a mean velocity which is not too small compared to the velocity of light and this is not

obviously the case for the outer electrons. In an atom consisting of many interacting electrons, however, any change in the characteristics of some electrons will induce modifications throughtout the entire system. As a result the relativistic effects can never be neglected in the outer electrons.

Here we consider the uranium atom as an example and explain the relativistic effects on the outer electrons, i.e. 7*s*, 6*d* and 5*f* electrons. Since the *s* electrons in both inner and outer shells have finite probability amplitude at the nucleus, in the vicinity of which the nuclear potential is deep, their velocity approaches the velocity of light. Consequently, the energy levels of the 7*s* electrons decrease and their orbital radius contracts, as well as the other *s* elctrons and the inner electrons. This direct relativistic effect induces an indirect effect on the other outer electrons, i.e. the 7*s* electrons and inner electrons will screen the nuclear charge more effectively, and the energy levels for the 6*d* and 5*f* electrons increase and their orbits spread outward, in contrast to the 7*s* electron. Especially, the indirect relativistic effect on the 5*f* electrons is very important for the electronic structures in a crystal, because the indirect relativistic effect makes the 5*f* orbit spread outward and hybridize with the other orbits more strongly, and consequently tends to promote an itinerant nature of the 5*f* electrons in a crystal.

It is clear from the qualitative considerations in the previous paragraph that the relativistic effects cannot be taken into account by the perturbation theory, because the relativistic effects on electronic states in an atom are different from orbit to orbit. According to the perturbation theory of the first order, the energy levels for orbits all together decrease. In order to take into account the relativistic constract effect and the relativistic screening effect properly, we must determine the wave

functions and their energy levels for all of the orbits by solving the Dirac one-electron equation self-consistently.

It has been already recognized in 1930s that the relativistic effects are very important in the atomic theory. As a practical application, Williams (1940) has first solved the Dirac equation numerically for the copper cation, and confirmed the contraction of the charge density for the inner electrons. However, the relativistic screening effect, i.e. the indirect relativistic effects on the outer electrons, has not been observed because the relativistic effects in the copper atom, the atomic number of which is 29, are not so large. The indirect relativistic effects on the outer electrons have been confirmed by Mayers (1957) for the mercury atom, the atomic number of which is 80. His calculations have been carried out with the EDSAC computer at Cambridge University, which was one of the most superior computer in those days, but it seems that the implementation was a hard work because of many electronic orbitals in the mercury atom. Afterward, Liberman *et al.* (1965) have established the stable method for solving the Dirac equation numerically for heavy atoms, though the potential used in their formalism is assumed to be given in the LDA. Here we will apply their method to the calculation for the rare-earth and the actinide atoms.

2.2. *Self-consistent calculation*

As is already pointed out in the previous section, the direct and indirect relativistic effects are accompanied with the large modification of the wave function. Therefore, any perturbation treatments of the relativistic effects do not lead to correct results even qualitatively. In order to obtain quantitatively reasonable results for the relativistic effects, it is essential to calculate self-consistently the one-electron orbital energies and wave functions by using the Dirac equation. The

method explained in this chapter was first introduced by Liberman *et al.* (1965). The Dirac Hamiltonian under the spherically symmetric field $V(r)$ is given by

$$H = c\alpha \cdot \boldsymbol{p} + \beta m_0 c^2 + V(r), \tag{2.1}$$

where α, β are 4×4 matrices usually used in the Dirac relativistic electron theory (Berestetski *et al.* 1980), and m_0 is a rest mass. Let $\boldsymbol{l}$ and $\boldsymbol{s}$ represent the orbital angular momentum and the spin angular momentum, respectively, then the total angular momentum is defined by $\boldsymbol{j} = \boldsymbol{l} + \boldsymbol{s}$. Using the space inversion operator P, the three commutation relations hold, i.e.

$$[H, j^2] = [H, j_z] = [H, P] = 0. \tag{2.2}$$

Thus, the eigenfunctions can be written as

$$\psi^M_{n\varpi j}(\boldsymbol{r}) = \frac{1}{r}\begin{pmatrix} P_{nlj}(r)\chi^M_{lj}(\hat{r}) \\ iQ_{nlj}(r)\chi^M_{l'j}(\hat{r}) \end{pmatrix}, \tag{2.3}$$

where ϖ is the quantum number for parity of the wave function, n is the principal quantum number, l and j represent the eigenvalues of the orbital angular momentum and the total angular momentum, respectively, and $\hat{r}$ means the spherical coordinate of $\boldsymbol{r}$. The spin angular function $\chi^M_{lj}(\hat{r})$ can be written as a sum of the products of the spherical harmonics $Y_{l,M-m}(\hat{r})$ and the Pauli spinor function $\chi(m)$ by using the Clebsch-Gordan coefficient $C(l\frac{1}{2}j; M-m, m)$:

$$\chi^M_{lj}(\hat{r}) = \sum_{m=\pm 1/2} C(l\tfrac{1}{2}j; M-m, m) Y_{l,M-m}(\hat{r})^* \chi(m), \tag{2.4}$$

where m is the spin component and takes the two values of $\pm 1/2$. Furthermore the relations among these quantum numbers are given by

$$j = l + \frac{1}{2}\varpi = l' - \frac{1}{2}\varpi, \quad \varpi = \pm 1. \tag{2.5}$$

We obtain for the radial wave function a set of coupled differential equations

$$\frac{\mathrm{d}}{\mathrm{d}r}\begin{pmatrix} P_{nlj}(r) \\ Q_{nlj}(r) \end{pmatrix} = \begin{pmatrix} -\kappa/r & \dfrac{\varepsilon_0 + \varepsilon_{nlj} - V(r)}{\hbar c} \\ \dfrac{V(r) - \varepsilon + \varepsilon_0}{\hbar c} & \kappa/r \end{pmatrix} \begin{pmatrix} P_{nlj}(r) \\ Q_{nlj}(r) \end{pmatrix}, \tag{2.6}$$

where

$$\kappa = -\varpi(j + \frac{1}{2}). \tag{2.7}$$

In eq. (2.6) $P_{nlj}(r)$ and $Q_{nlj}(r)$ are the large and small components of the radial wave function, respectively. ε_{nlj} represents the eigenvalue of the state (n, l, j), and is measured relative to the rest energy ε_0.

In order to perform the self-consistent calculation we must obtain the new one-electron potential which is constructed by the new charge density. The charge density is spherically averaged and constructed from the eigenfunctions in eq. (2.6):

$$\rho(r) = \sigma(r) / 4\pi r^2, \tag{2.8}$$

$$\begin{aligned}\sigma(r) &= \sum_{n,\varpi,j,M} \int r^2 \mathrm{d}\omega [\psi^M_{n\varpi j}(\boldsymbol{r})]^* \psi^M_{n\varpi j}(\boldsymbol{r}) \\ &= \sum_{n,l,j} W_{nlj} \{P_{nlj}(r)^2 + Q_{nlj}(r)^2\},\end{aligned} \tag{2.9}$$

where the integration is performed over solid angles, and W_{nlj} represents the number of the electrons in the state (n, l, j).

Once the charge density has been determined, the Coulomb potential (the Hartree potential) and the exchange-correlation potential can be calculated. The Coulomb potential is readily obtained by integrating the Poisson equation. The exchange-correlation potential is treated within the density-functional formalism in the LDA. Using the atomic units in which $\hbar = 1$, the rest mass $m_0 = 1/2$, $e^2 = 2$, $c = 274$, i.e. the energy and the length are measured in units of 1 Ryd. and the Bohr radius, respectively, we can write the one-electron potential as

$$V(r) = -\frac{2Z}{r} + \frac{2}{r}\int_0^r \sigma(t)\mathrm{d}t + 2\int_r^\infty \frac{\sigma(t)}{t}\mathrm{d}t + V_{\mathrm{xc}}[r_{\mathrm{s}}(r)], \tag{2.10}$$

where $V_{\mathrm{xc}}[r_{\mathrm{s}}(r)]$ represents the exchange-correlation potential. The parameter $r_{\mathrm{s}}(r)$ is the radius of the sphere which encloses one unit of the electron charge. It is given by

$$r_{\mathrm{s}}(r) = \left(\frac{3}{4\pi}\right)^{\frac{1}{3}} \rho(r)^{-\frac{1}{3}}. \tag{2.11}$$

The new potential thus determined is substituted into eq.(2.6), and subsequently the next iteration proceeds. The iterations are repeated until the convergence criterion $|rV_{\mathrm{in}}(r) - rV_{\mathrm{out}}(r)| < 0.001$ is satisfied, where $V_{\mathrm{in}}(r)$ and $V_{\mathrm{out}}(r)$ are supposed to be the input and the output

potential, respectively, and thereafter the eigenstates and eigenvalues in the self-consistent field can be obtained.

As already mentioned, it is not sufficient to treat the relativistic effects within the perturbation theory, because the indirect relativistic effects can only be taken into account by the self-consistent calculation. In order to show these insufficiencies in the perturbation theory, we also perform the calculation where the relativistic effects are taken into account as the perturbation of the first order. The perturbation calculation is based on the two-component approximation in which the four-component relativistic wave function is throughout expressed by using the two-component wave function. The two-component equation is expanded up to the first order of the perturbation parameter α^2 (the Pauli approximation). Let us denote the non-relativistic eigenvalue and radial eigenfunction as $E^0(n,l)$ and $R^0_{nl}(r)$, respectively (Herman and Skillman 1963), then the resultant eigenvalue $E_{\mathrm{RCOR}}(n,l,j)$ with the relativistic correction is given by

$$E_{\mathrm{RCOR}}(n,l,j) = E^0(n,l) + E_{\mathrm{VEL}}(n,l) + E_{\mathrm{DAR}}(n,l)$$

$$+ \begin{cases} -(l+1)E_{\mathrm{SO}}(n,l) & \text{for} \quad j = l+1/2 \\ lE_{\mathrm{SO}}(n,l) & \text{for} \quad j = l-1/2 \end{cases} . \tag{2.12}$$

The second term on the right-hand side in eq. (2.12), $E_{\mathrm{VEL}}(n,l)$, represents the mass-velocity correction and necessarily takes the negative value:

$$E_{\mathrm{VEL}}(n,l) = -\frac{\alpha^2}{4}\int_0^{\infty} [R^0_{nl}(r)]^2 [E^0(n,l) - V(r)]^2 r^2 \mathrm{d}r . \tag{2.13}$$

The third term on the right-hand side in eq. (2.12), $E_{\mathrm{DAR}}(n,l)$, represents the Darwin correction. In the case of the hydrogen-like atoms, i.e. under the Coulomb interaction $V(r) = -2Z/r$, the Darwin correction is nonzero only for the s state ($l = 0$). In general cases we can easily speculate that the Darwin correction is very small except the s state on the analogy of the above special case:

$$E_{\mathrm{DAR}}(n,l) = -\frac{\alpha^2}{4}\int_0^{\infty} R_{nl}^0(r)\frac{\mathrm{d}V}{\mathrm{d}r}\frac{\mathrm{d}R_{nl}^0(r)}{\mathrm{d}r}r^2\mathrm{d}r. \tag{2.14}$$

The last term on the right-hand side in eq. (2.12) represents the spin-orbit coupling and causes the energy splitting between two states having the different j:

$$E_{\mathrm{SO}}(n,l) = \frac{\alpha^2}{4}\int_0^{\infty} [R_{nl}^0(r)]^2\frac{1}{r}\frac{\mathrm{d}V}{\mathrm{d}r}r^2\mathrm{d}r. \tag{2.15}$$

2.3. *Results and discussions*

Table 2.I shows the one-electron orbital energies in the uranium atom. It is important to investigate how the energy levels may be influenced by the relativistic corrections. Both in the perturbation calculation and in the self-consistent calculation, the bindings of the core-electrons become stronger. On the other hand, the bindings of the outer electrons, i.e. 5*f* and 6*d* orbitals, become stronger in the perturbation calculation but become weaker in the self-consistent calculation. In order to observe these results clearly, the energy levels of the outer orbits, 5*f*, 6*d* and 7*s* are shown in Fig.2.1. The solid curve, dashed curves and dotted curves represent the non-relativistic, perturbation and self-consistent calculations, respectively. The one-electron energies for the 6*d* and 5*f* orbits split into the two levels owing to

Table 2.I. The energy levels for all orbits in the neutral U atom. ε^0_{nl}, E_{RCOR} and E_{REL} indicate the results of the nonrelativistic, perturbation and self-consistently relativistic calculations, respectively. E_{EXP} represent the experimental results taken from Sandstrom (1957).

state	$-\varepsilon^0_{nl}$ (Ryd.)	$-E_{\mathrm{RCOR}}$ (Ryd.)	$-E_{\mathrm{REL}}$ (Ryd.)	$-E_{\mathrm{EXP}}$ (Ryd.)
1s 1/2	7378.79488	8234.55886	8507.50302	8514.7
2s 1/2	1279.63796	1527.59898	1588.93722	1602.6
2p 1/2	1238.29798	1489.80745	1532.18031	1542.2
3/2		1287.49729	1250.98815	1264.2
3s 1/2	322.31442	389.53806	401.06696	408.5
3p 1/2	302.03634	368.45008	375.29317	381.4
3/2		322.77997	310.51010	316.6
3d 3/2	264.03329	282.75082	269.69859	273.9
5/2		270.02916	256.55343	261.5
4s 1/2	81.13295	100.04910	102.14353	105.5
4p 1/2	71.78340	89.75414	90.54967	92.3
3/2		78.00714	73.64000	76.6
4d 3/2	54.32314	59.45117	55.17513	57.3
5/2		56.47023	52.06772	54.1
4f 5/2	30.13158	31.56928	27.77924	28.4
7/2		30.70792	26.96914	27.9
5s 1/2	17.72197	22.63967	22.74494	23.6
5p 1/2	14.10978	18.46459	18.24046	18.6
3/2		15.66367	14.21700	14.5
5d 3/2	7.80543	8.85614	7.63899	7.2
5/2		8.27138	7.04395	
5f 5/2	0.80353	0.94915	0.33293	
7/2		0.86929	0.27259	
6s 1/2	2.72030	3.66878	3.56819	5.32
6p 1/2	1.71157	2.41653	2.26741	2.2
3/2		1.96506	1.60941	
6d 3/2	0.34459	0.42499	0.26204	0.27
5/2		0.38064	0.22808	
7s 1/2	0.32346	0.41059	0.38494	

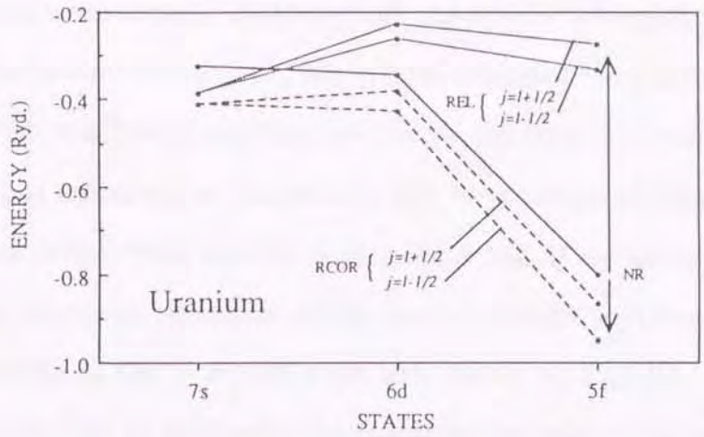

Figure 2.1. The energy levels for the outer orbits, 5*f*, 6*d* and 7*s*. The solid curve, dashed curves and dotted curves represent the results of the nonrelativistic, perturbation and self-consistently relativistic calculations, respectively. The energy levels for the 5*f* orbit splits into two levels such as j=7/2 and 5/2 as well as two levels for the 6*d* orbit such as j=5/2 and 3/2.

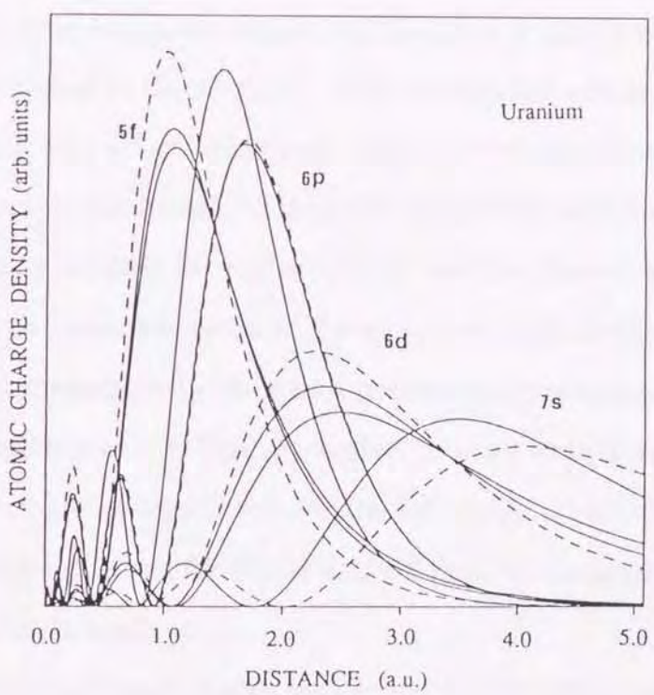

Figure 2.2. The radial charge denities for the outer orbits in the U atom. The solid curves and dashed curve denote the results of the self-consistently relativistic calculation and the nonrelativistic calculation, respectively.

the spin-orbit interaction. Although all the orbital energies shift deeply in the perturbation calculation, the orbital energies for the 6*d* and 5*f* electrons shift shallowly and that for the 7*s* electron shifts deeply in the self-consistent calculation. Especially the magnitude of this energy shift from the non-relativistic results is larger for the 5*f* electron.

The radial charge densities which are calculated self-consistently for the outer orbits in the uranium atom are shown in Fig.2.2. The charge distribution for the 7*s* orbit shrinks towards the origin and its energy becomes deeper. Conversely the charge distributions for the 6*d* and 5*f* orbits expand outward and their energies become shallower. The cause of these behaviors can be explained physically as follows: the 7*s* orbit has finite probability amplitude at the nucleus, in vicinity of which the nuclear potential is very deep, so that its velocity approaches the light velocity, i.e. the relativistic effects become large. As a result, the energy level for the 7*s* orbit becomes deeper and the charge distribution for the 7*s* orbit is contracted to the nucleus. This contraction effect are be called the direct relativistic effect. Similarly, for the core-electrons, the direct relativistic effect is dominant. This direct relativistic effect on the 7*s* and the core-electrons induces an indirect effect on the other outer electrons, i.e. the 7*s* and the core electrons will screen the nuclear charge more effectively, and consequently the mean potential experimenced by the other outer electrons will be less attractive. Owing to this indirect relativistic effect, the energy levels for the 6*d* and 5*f* orbits increase and the radial charge densities for the 5*f* and 6*d* electrons expand outward, in contrast to the 7*s* electron.

The same calculations are also performed for the other actinide atoms. The results are shown in Figs. 2.3, 2.4 and 2.5. The configuration of the valence electrons assumed in this calculation are shown above the figures. The ground state configurations of the valence

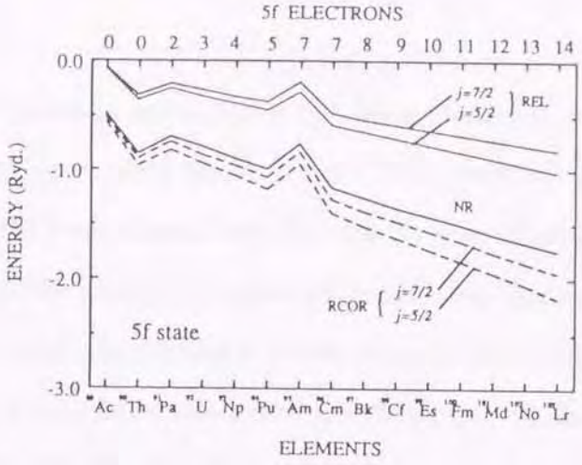

Figure 2.3. The energy level for the 5*f* orbit in the actinide atoms. The solid curve, dashed curves and dotted curves represent the results of the nonrelativistic, perturbation and self-consistently relativistic calculations, respectively. The number of the 5*f* electrons for the configurations assumed in the calculations is shown on the top of the figure. Except the Th and Am atoms, the number of the 6*d* and 7*s* electrons are assumed to be $6d^17s^2$ in the actinide atoms. Configurations for the Th and Am atoms are given by $6d^27s^2$ and $6d^07s^2$, respectively.

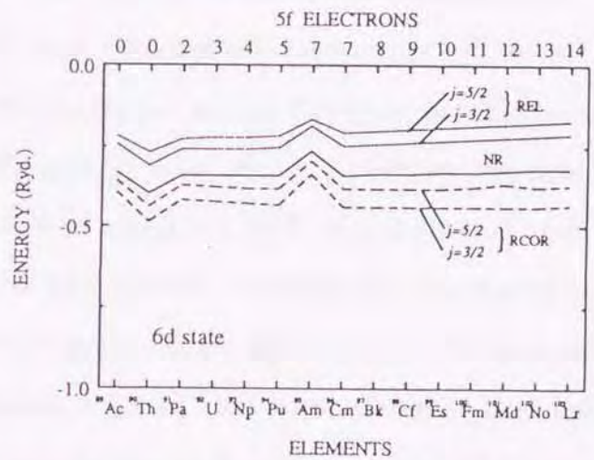

Figure 2.4. The energy level for the 6*d* orbit in the actinide atoms. The other explanations for this figure are the same as the figure caption of Figure.2.3.

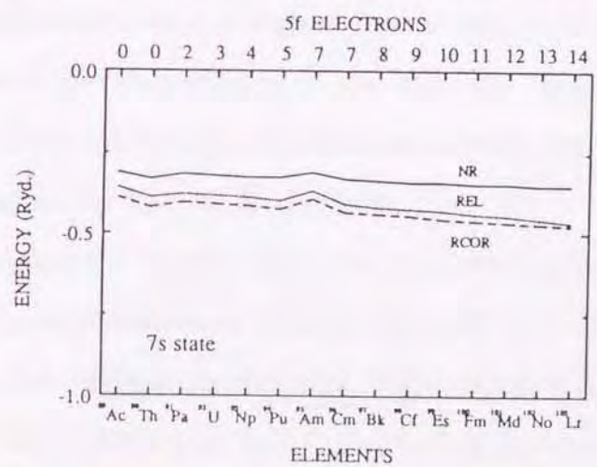

Figure 2.5. The energy level for the 7*s* orbit in the actinide atoms. The other explanations for this figure are the same as the figure caption of Figure.2.3.

electrons in the actinide series have not been clearly determined and there are conflicting reports about them. This problem will be discussed later. Here we will investigate how the relativistic effects in the actinide atoms change as the atomic number increases, on the assumption of the above configurations. In all the actinide atoms, the relativistic effects work in the same way as in the uranium atom, i.e. for the 7*s* orbit the direct relativistic contribution is dominant, while for the 5*f* and 6*d* orbitals the reverse situation is observed. It is the common characteristic to all actinide atoms that the 5*f* electrons suffer the largest relativistic correction. As the atomic number increases, it can be seen that the difference in energy between the non-relativistic and relativistic results becomes large because the relativistic effects are enhanced in the heavier atom. This behavior is also the most notable for the 5*f* orbit.

In Fig. 2.3, the energy level of the 5*f* orbit for the americium atom shows the increase of about 0.2 Ryd. in comparison with the neighboring atoms, plutonium and curium, because the number of the 5*f* electrons increases by two at once. Since this energy difference originates from the different configurations of the outer electrons between $5f^7 6d^0 7s^2$ and $5f^6 6d^1 7s^2$, it almost corresponds to the energy difference of the ground states in the actinide ions between $^8S_{7/2}$ and $^7F_0$ if we consider only 5*f* electrons. Furthermore we can regard it as a reasonable quantitative estimate for the *U*-parameter used in the Hubbard Hamiltonian, since it represents the Coulomb energy increased by adding one 5*f* electron to the state which essentially has six 5*f* electrons.

Next we compare the magnitude of the spin-orbit splitting of the 5*f* orbit with the experimental one, though it is difficult to determine the energy of the outer orbits quantitatively. Figures 2.6, 2.7, 2.8 and 2.9 show the spin-orbit splitting of the 5*f* orbit for the various valences in the actinide ions. The spin-orbit parameter of the 5*f* orbit is defined as

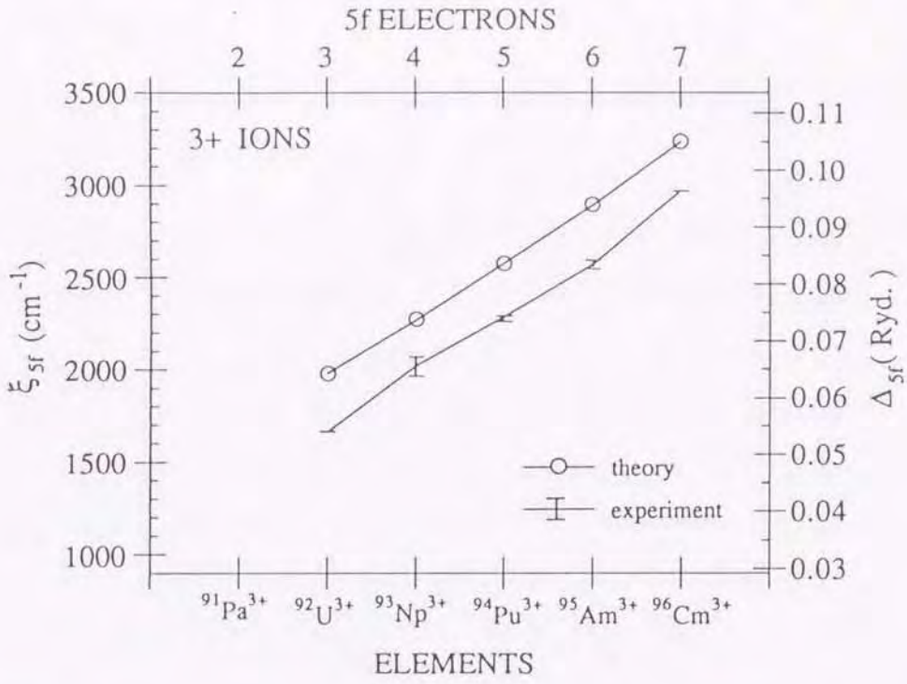

Figure 2.6. The spin-orbit parameter of the 5*f* orbit for the trivalent actinide ions. The corresponding spin-orbit splittings $\Delta_{5f}(\equiv \varepsilon_{f,7/2} - \varepsilon_{f,5/2})$ can be read from the scale on the right ordinate. The number of the 5*f* electrons used in the calculations are shown on the top of the figure. Open circles represent the theoretical results. The experimental results from Desclaux and Freeman (1984) and Freeman and Koelling (1974) are indicated by the error-bars, each of whic ranges from a minimum value to a maximun value.

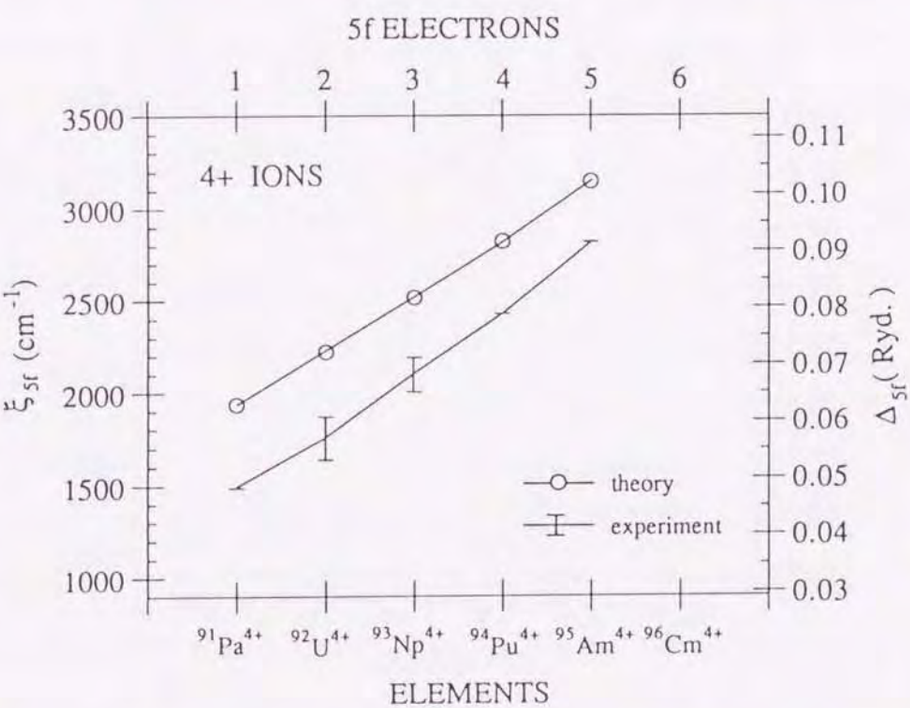

Figure 2.7. The spin-orbit parameter of the 5*f* orbit for the tetravalent actinide ions. The other explanations for this figure are the same as the figure caption of Figure 2.6.

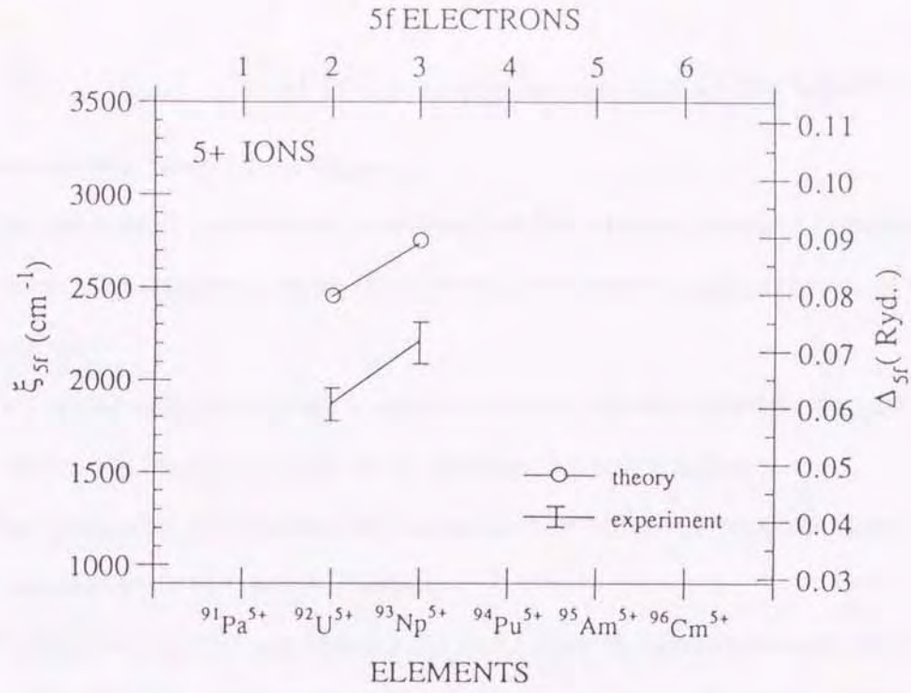

Figure 2.8. The spin-orbit parameter of the 5*f* orbit for the pentavalent actinide ions. The other explanations for this figure are the same as the figure caption of Figure 2.6.

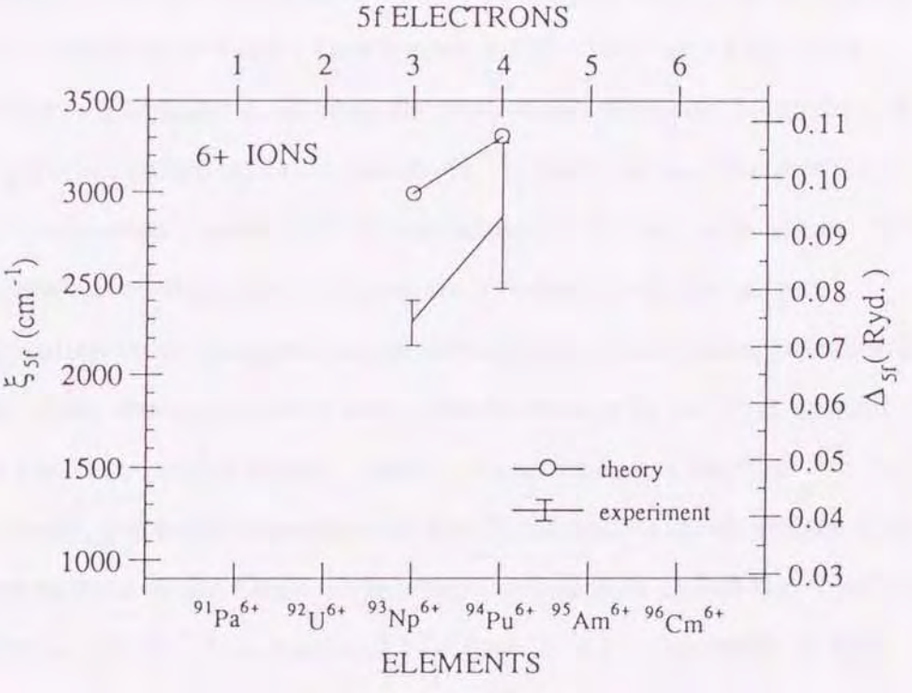

Figure 2.9. The spin-orbit parameter of the 5*f* orbit for the hexavalent actinide ions. The other explanations for this figure are the same as the figure caption of Figure 2.6.

$\xi_{5f} \equiv \frac{2}{7}\left(\varepsilon_{f7/2} - \varepsilon_{f5/2}\right)$. The following tendencies are seen in the behavior of this parameter from these figures:

(1) The spin-orbit parameter increases as the atomic number becomes large when we compare some ions having the same configuration of the $5f$ electrons.

(2) The spin-orbit parameter increases as the atomic number becomes large when we compare some ions having the same valence.

(3) The spin-orbit parameter increases as the valences become large when we compare the same element.

We can interpet the tendencies (1) and (2) as the enhancement of the relativistic effects on account of the increase in the nuclear charge, and the tendency (3) as the result of the substantial increase in the effect of the nuclear charge with the decrease in the number of electrons. The quantitative difference between theory and experiment is about 20 %, though the behavior of the theoretical results can explain qualitatively well the experimental one (Lewis *et al.* 1970 , Chan and Lam 1974).

We have discussed so far one-electron states obtained by assuming a groung state configuration of electrons. Finally let us consider the ground state configuration of the electrons for the actinide atoms. It has been understood that there is some uncertainty as to the correct configuration to be assigned in the description of actinides, because the ground state configuration is very close in energy to the first excited state (Desclaux and Freeman 1984). As an instance for this uncertainty, the relative position of the $5f$, $6d$ and $7s$ levels differs with the treatments of the Coulomb interaction which is called the Coulomb correlation effects (Freeman and Koelling 1974). The origin of this uncertainty may be partially understood by comparing the energies of the outer electrons which are obtained by assuming the different

configurations. In the following discussions, we will observe the thorium, uranium and americium atoms in particular. Figures 2.10, 2.11 and 2.12 compare the orbital energies of the outer electrons of the thorium, uranium and americium atoms for three kinds of configurations, respectively. In each figure, the configuration marked $*$ represents is assumed in the above calculations, i.e. used in Figs. 2.3, 2.4 and 2.5. It is interesting to observe that the relative position of the $5f$, $6d$ and $7s$ levels is quite sensitive to the assumed configurations. The ground state configuration can be speculated from the relative position of the outer electrons to some degree. In the case of the americium, the configurations $5f^5 6d^2 7s^2$ and $5f^6 6d^1 7s^2$ are inconsistent in energy, because the $6d$ and $7s$ levels which are higher than the $5f$ level are occupied nevertheless the $5f$ orbits are partially vacant. On the other hand, the energy levels are occupied with electrons in order of energy for the configuration $5f^7 6d^0 7s^2$. Therefore the configuration $5f^7 6d^0 7s^2$ is appropriate to the ground state configuration for the americium atom. Similar considerations are applied to the thorium and uranium atoms, and consequently the configurations $5f^0 6d^2 7s^2$ and $5f^3 6d^1 7s^2$ are reasonable to the ground state configurations, respectively. Thus, the assumed ground state configuration used here seem to be the most reasonable one at least within LDA.

Relativistic effects in the rare-earth atoms are qualitatively similar to those in the actinide atoms. In order to observe these similarities well, the one-electron orbital energies in the cerium atom are shown in Table 2.2. It is easily understood that the outer electrons $4f$, $5d$ and $6s$ of the cerium atom have the same behavior as the $5f$, $6d$ and $7s$ electrons of the uranium atom, respectively, i.e. for the $4f$ electons the indirect relativistic effect is dominant while the other outer electrons are dominantly subject to the direct relativistic effect. However the

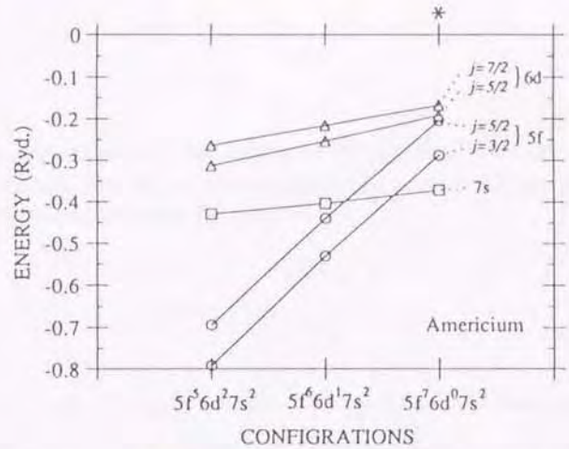

Figure 2.10. The orbital energies of the outer electrons for the Am atom in three cases of configurations. The mark * on the top of the figure indicates the configuration used in the calculation of the neutral atom.

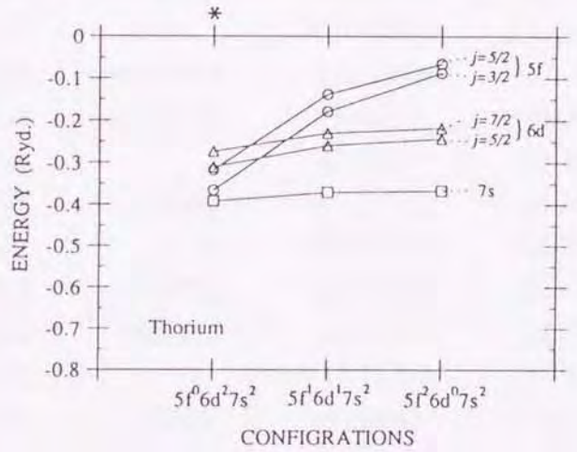

Figure 2.11. The orbital energies of the outer electrons for the Th atom in three cases of configurations. The mark * on the top of the figure indicates the configuration used in the calculation of the neutral atom.

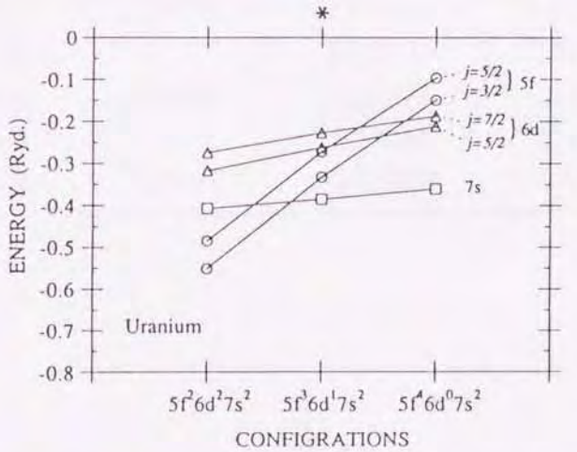

Figure 2.12. The orbital energies of the outer electrons for the U atom in three cases of configurations. The mark * on the top of the figure indicates the configuration used in the calculation of the neutral atom.

Table 2.II. The energy levels for all orbits in the neutral Ce atom. ε^0_{nl}, E_{RCOR} and E_{REL} indicate the results of the nonrelativistic, perturbation and self-consistently relativistic calculations, respectively.

state	$-\varepsilon^0_{nl}$ (Ryd.)	$-E_{\mathrm{RCOR}}$ (Ryd.)	$-E_{\mathrm{REL}}$ (Ryd.)
1s 1/2	2811.87596	2950.36147	2953.90041
2s 1/2	436.89358	473.71286	472.50138
2p 1/2	413.38548	449.67374	446.28550
3/2		420.40362	413.49935
3s 1/2	93.51219	102.18466	101.32147
3p 1/2	83.32163	91.48704	90.19813
3/2		85.78777	83.75668
3d 3/2	64.27967	66.29202	64.24151
5/2		64.90970	62.85627
4s 1/2	18.37491	20.45223	20.13416
4p 1/2	14.58291	16.40065	16.00951
3/2		15.18211	14.62496
4d 3/2	7.92729	8.32480	7.85144
5/2		8.08410	7.61110
4f 5/2	0.32433	0.36372	0.13886
7/2		0.33936	0.11809
5s 1/2	2.58042	2.93435	2.83264
5p 1/2	1.57992	1.83328	1.73436
3/2		1.66511	1.54265
5d 3/2	0.26190	0.28293	0.23393
5/2		0.27048	0.223139
6s 1/2	0.31037	0.33984	0.326841

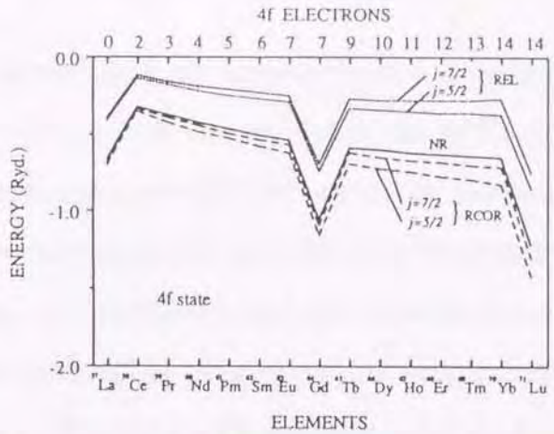

Figure 2.13. The energy level for the 4*f* orbit in the rare-earth atoms. The solid curve, dashed curves and dotted curves represent the results for the nonrelativistic, perturbation and self-consistently relativistic calculations, respectively. The number of the 4*f* electrons for the configurations assumed in the calculations is shown on the top of the figure. Except the La, Gd and Lu atoms, the number of the 5*d* and 6*s* electrons are assumed to be $5d^0 6s^2$ in the actinide atoms. Configurations for the La, Gd and Lu atoms are given by $5d^1 6s^2$.

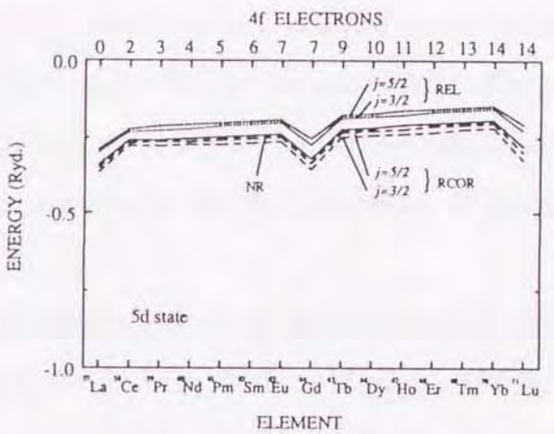

Figure 2.14. The energy level for the 5*d* orbit in the rare-earth atoms. The other explanations for this figure are the same as the figure caption of Figure.2.13.

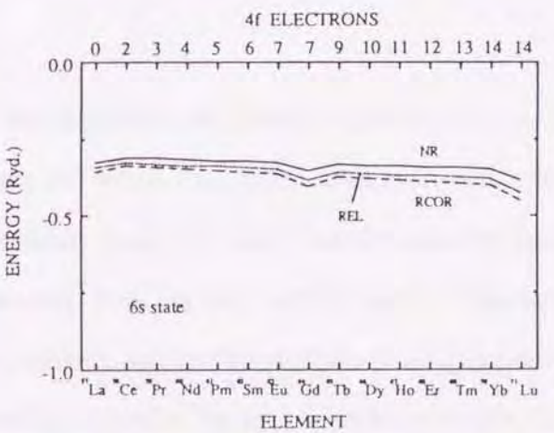

Figure 2.15. The energy level for the 6*s* orbit in the rare-earth atoms. The other explanations for this figure are the same as the figure caption of Figure.2.13.

relativistic energy corrections are smaller in the cerium atom than in the uranium atom. This result suggests that the 5*f* electrons may be more apt to be delocalized than the 4*f* electrons in a crystal. To explain the different behavior between the rare-earth 4*f* electrons and the actinide 5*f* electrons, it was argued that the delocalization of the 5*f* orbitals is a consequence of the requirement of orthogonality between the 5*f* and the 4*f* orbitals. But, this orthogonality constraint was shown to be of rather minor importance in explaining the delocalization of the 5*f* electrons (Desclaux and Freeman 1984). Furthermore since the expectation values of the non-relativistic radial wave functions are already quite different between the rare-earth and the actinide elements (Mann 1968), the differences between the two series cannot be attributed to the relativistic effects only. While the relativistic effects are quite significant, the shell structure effects mentioned above cannot be neglected in the explanation for the delocalization of the actinide 5*f* electrons.

For all rare-earth atoms, the same calculations as the cerium atom are performed and shown in Figs. 2.13, 2.14 and 2.15. A similar explanation can be applied to the 4*f*, 5*d* and 6*s* electrons in the rare-earth atoms.

2.4. *Summary*

In this chapter, we compare the theoretical results for the one-electron orbital energies, wave functions and spin-orbit splittings with the experimental results, and find that the theoretical results can explain the experimental results reasonably well. However, our point is not the quantitative agreement between theory and experiment but the fact that the physical properties for the actinide or rare-earth atoms can

be explained qualitatively well by means of a simplified atomic theory which is based in the LDA.

A starting point of the atomic theory is to solve the Hartree-Fock equation, though the way to solve it becomes more complicated than the method of Liberman *et al.* (1965) because it contains the exchange term in a non-local form. The approach to reinforce the Hartree-Fock equation with the correlation interaction has already been performed for some atoms with small atomic numbers (Yamagami *et al.* 1994). It is our next step in a relativistic atomic theory to take the relativistic effects into account in the correlated Hartree-Fock equation.

3. Relativistic Linear Augmented Plane Wave Method

3.1. *Introduction*

The rare-earth and the actinide compounds have recently attracted particular interest, because strongly-correlated electron systems are realized in many of them.[1] Though it is evident that many-body effects due to the 4*f* and 5*f* electrons are essential in determining physical properties of these systems, one-electron theory can play a crucial role in exploring the nature of the 4*f* and 5*f* electrons (Onuki and Hasegawa 1995, Norman and Koelling 1993). Measurements of the dHvA effect, in parallel with many other experiments, on various rare-earth and actinide compounds are now in progress, and reliable calculations of the electronic structure, in particular the Fermi surface, are desired.

In the RAPW method, inside the APW spheres the exact solution of the Dirac equation which corresponds to the true eigenvalue is used as the basis function. Therefore, matrix elements inevitably become dependent on the eigenvalue, and the eigenvalues should be obtained by finding zeros of the secular determinant. This property of the basis function produces the high accuracy in determining the eigenvalues, but on the other hand it becomes a weakness of this method, because there are many important rare-earth and actinide compounds with a complex crystal structure where many *f* bands exist in a narrow range of energy, and in such a case this calculational scheme is apt to miss the eigenvalues, unless zeros of the secular determinant are searched very carefully. In the improved RAPW method (Yamagami and Hasegawa 1990), this difficulty is got rid of partly by utilizing the symmetrization technique at the $\boldsymbol{k}$ points with high symmetry in the Brilloiun zone. But, construction of the Fermi

---

[1] For recent progress, see, *Proceedings of the International Conference on Strongly Correlated Electron Systems*, ed. T. Kasuya, A. Yanase and K. Okuda (North-Holland, Amsterdam, 1993) [Physica B **186-188** (1993)].

surface requires mostly calculations at general $\boldsymbol{k}$ points where the symmetrization technique cannot exhibit its power.

Here we will derive a linear form suitable for compounds having many kinds of atoms in the primitive cell from Loucks' RAPW method (Loucks 1967) on the basis of relativistic band theory proposed by Takeda (Takeda 1979). In this method, the four-component relativistic plane wave is augmented by a linear combination of the solutions of the Dirac equation for two fixed energies for each value of the angular momentum. The basis function is constructed in a composite form, but its large and small components are made continuous everywhere in a crystal. Therefore, in order to carry out the variational calculation, it is not necessary to introduce surface integrals on the APW spheres, and it can be carried out simply by minimizing the expectation value of energy. In addition, matrix elements of the Dirac Hamiltonian and the overlap integral do not depend on the energy which should be determined. Thus, the main difficulty accompanied with Loucks' RAPW method has been removed out. The energy can be obtained by solving an ordinary eigenvalue problem.

We have already tested the accuracy of this RLAPW method carefully by calculating the energy band structures for the heavy-electron compound $CeRh_2$ (Higuchi *et al.* 1994a) and fcc Th metal (Higuchi *et al.* 1994b), and confirmed that it can reproduce well within 1 mRyd. the energies which are determined at general $\boldsymbol{k}$ points by Loucks' RAPW method. In addition, at each $\boldsymbol{k}$ point, once a secular equation is solved by a standard numerical method, all *f* bands besides other bands are surely determined, and in practice it takes much less computational time than the RAPW method. Then, we have completed a self-consistent band structure calculation scheme on the basis of the RLAPW method within the framework of the exchange-correlation potential (Gunnarsson and Lundrvist 1976) in the LDA. Its accuracy and efficiency ensures that the RLAPW method will be

promising for a study of the electronic structures in the rare-earth and the actinide compounds with a complex crystal structure. In this chapter, we will present a brief but self-contained description of this self-consistent, relativistic linear APW method.

3.2 *Formulation*

We assume that a crystal consists of P kinds of atoms and contains N_p atoms of the pth-type in the primitive cell. The total number of atoms in the primitive cell, N_t, is therefore given by the sum of N_p over p. The radius of the pth type APW sphere is assumed to be S_p. We adopt the MTA to a spatial shape of the one-electron potential, i.e. it is supposed to be spherically symmetric in the APW spheres and equal to a constant value V_0 in the interstitial region. Throughout this chapter, we use the atomic units in which $\hbar = 1$, $m_0 = 1/2$, $e^2 = 2$ and $c = 1/\gamma = 274$, where γ is the fine-structure constant. The units of energy and length are 1 Ryd. and the Bohr radius, respectively.

3.2.1 *Basis functions*

In the RLAPW method, the basis functions are constructed from the solutions of the Dirac one-electron equation in the APW spheres and in the interstitial region. In the interstitial region, the four-component relativistic plane wave for a given wave vector $\boldsymbol{k}_\mu$ and a fixed spin component m (= +1/2 or −1/2) is given by (Rose 1961)[2]

$$\psi_\mu^m(\boldsymbol{s}) = \left(\frac{1+q_\mu}{2q_\mu}\right)^{\frac{1}{2}} \begin{pmatrix} \chi(m) \\ \dfrac{2\gamma\sigma\cdot\boldsymbol{k}_\mu}{1+q_\mu}\chi(m) \end{pmatrix} e^{i\boldsymbol{k}_\mu\cdot\boldsymbol{s}}, \tag{3.1}$$

---

[2] Chapter III, p.68

where σ is the Pauli spin matrix, $\chi(m)$ is the Pauli spinor, and q_μ is defined by

$$q_\mu = (1+4\gamma^2 k_\mu^2)^{\frac{1}{2}}. \tag{3.2}$$

The wave vector $\boldsymbol{k}_\mu$ is given by the sum of the wave vector $\boldsymbol{k}$ in the Brillouin zone and a reciprocal lattice vector $\boldsymbol{K}_\mu$ as

$$\boldsymbol{k}_\mu = \boldsymbol{k} + \boldsymbol{K}_\mu. \tag{3.3}$$

The energy of the relativistic plane wave relative to the rest energy, ε_μ, is given by (Rose 1961)

$$\varepsilon_\mu = \frac{1}{\gamma^2}\left(\frac{q_\mu}{4} - 1\right) + V_0. \tag{3.4}$$

Let us consider the form of the relativistic plane wave in the vicinity of the nth APW sphere whose center is located at $\boldsymbol{r}_n$. As is shown in Fig. 3.1, the radius vector $\boldsymbol{s}$ can be written as $\boldsymbol{s} = \boldsymbol{r}_n + \boldsymbol{r}$.

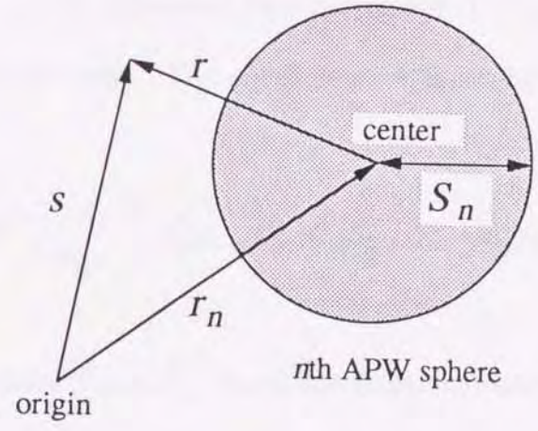

Figure 3.1. In the vicinity of the nth APW sphere whose center is located at $\boldsymbol{r}_n$, the position vector $\boldsymbol{s}$ relative to an arbitrary origin can be expressed as $\boldsymbol{s}=\boldsymbol{r}_n+\boldsymbol{r}$, where $\boldsymbol{r}$ is measured from the center of the nth APW sphere.

The relativistic plane wave can be expanded in the spin-angular function $\chi_\kappa^M(\hat{r})$ as[3]

$$\psi_\mu^m(\boldsymbol{s}) = \mathrm{e}^{\mathrm{i}\boldsymbol{k}_\mu\cdot\boldsymbol{r}_n}\sum_\kappa\sum_{M=-j}^{j} A_{\kappa\mu M}^m \begin{pmatrix} j_l(k_\mu r)\chi_\kappa^M(\hat{r}) \\ \dfrac{2\mathrm{i}\gamma k_\mu S_\kappa}{1+q_\mu} j_{l'}(k_\mu r)\chi_{-\kappa}^M(\hat{r}) \end{pmatrix}, \tag{3.5}$$

where $j_l(x)$ is the spherical Bessel function of order l, and S_κ means the sign of κ. Parameter κ takes any nonzero integer, positive or negative, and is related to the total angular momentum j and the orbital angular momentum l by the relations

$$\begin{aligned} &l=\kappa, \quad j=l-\frac{1}{2}=l'+\frac{1}{2}, && \text{for } \kappa>0, \\ &l=-\kappa-1, \quad j=l+\frac{1}{2}=l'-\frac{1}{2}, && \text{for } \kappa<0. \end{aligned} \tag{3.6}$$

In eq. (3.5) the spin-angular function $\chi_\kappa^M(\hat{r})$ is defined by (Rose 1961)

$$\chi_\kappa^M(\hat{r}) = \sum_{m=\pm\frac{1}{2}} C(l\tfrac{1}{2}j; M-m, m) Y_{l,M-m}^*(\hat{r})\chi(m), \tag{3.7}$$

where $Y_{l,M-m}(\hat{r})$ is the spherical harmonics and $C(l\frac{1}{2}j; M-m, m)$ is the Clebsch-Gordon coefficient. The coefficient $A_{\mu\kappa M}^m$ in eq. (3.5) is defined by

$$A_{\mu\kappa M}^m = 4\pi\mathrm{i}^l\left(\frac{1+q_\mu}{2q_\mu}\right)^{\frac{1}{2}} Y_{l,M-m}^*(\hat{k}_\mu) C(l\tfrac{1}{2}j; M-m, m). \tag{3.8}$$

In eqs. (3.7) and (3.8), $\hat{r}$ and $\hat{k}_\mu$ mean the spherical coordinates of $\boldsymbol{r}$ and $\boldsymbol{k}_\mu$, respectively.

---

[3] Chapter V, p. 157 in Rose (1961)

Inside the nth APW sphere, the one-electron potential is assumed to be the spherically symmetric function $V_n(r)$. By Takeda's theory, the basis function $\tilde{\psi}_{\mu}^{m,n}(\boldsymbol{s})$ is constructed by a linear combination of the solutions of the Dirac equation for the two energy values $\varepsilon_{\kappa 1}^{n}$ and $\varepsilon_{\kappa 2}^{n}$, which are chosen appropriately for each value of κ within a limited range of energy, as (Takeda 1979)

$$\tilde{\psi}_{\mu}^{m,n}(\boldsymbol{s}) = \mathrm{e}^{\mathrm{i}\boldsymbol{k}_{\mu}\cdot\boldsymbol{r}_n} \sum_{\kappa} \sum_{M=-j}^{j} A_{\kappa\mu M}^{m} \sum_{\alpha=1,2} a_{\kappa\mu\alpha}^{n} \begin{pmatrix} g_{\kappa\alpha}^{n}(r)\chi_{\kappa}^{M}(\hat{r}) \\ \mathrm{i}S_{\kappa} f_{\kappa\alpha}^{n}(r)\chi_{-\kappa}^{M}(\hat{r}) \end{pmatrix}, \tag{3.9}$$

where the large component $g_{\kappa\alpha}^{n}(r)$ and the small component $f_{\kappa\alpha}^{n}(r)$ of the radial wave function satisfy a set of coupled differential equations

$$\begin{pmatrix} V_n(r) - \varepsilon_{\kappa\alpha}^{n} & -\frac{1}{\gamma}\left(\frac{\mathrm{d}}{\mathrm{d}r} - \frac{\kappa}{r}\right) \\ \frac{1}{\gamma}\left(\frac{\mathrm{d}}{\mathrm{d}r} + \frac{\kappa}{r}\right) & V_n(r) - \frac{1}{\gamma^2} - \varepsilon_{\kappa\alpha}^{n} \end{pmatrix} \begin{pmatrix} r g_{\kappa\alpha}^{n}(r) \\ S_{\kappa} r f_{\kappa\alpha}^{n}(r) \end{pmatrix} = 0, \qquad \alpha = 1, 2. \tag{3.10}$$

Here, $\varepsilon_{\kappa\alpha}^{n}$ is measured relative to the rest energy, and the radial wave function is normalized by the condition

$$\int_{0}^{s_n} \left\{ g_{\kappa\alpha}^{n}(r)^2 + f_{\kappa\alpha}^{n}(r)^2 \right\} r^2 \mathrm{d}r = 1. \tag{3.11}$$

The expansion coefficients $a_{\kappa\mu\alpha}^{n}$ in eq. (3.9) are chosen so that both large and small components can match those of the relativistic plane wave (3.5) at the boundary of the nth APW sphere. They are given by

$$\begin{pmatrix} a^n_{\kappa\mu 1} \\ a^n_{\kappa\mu 2} \end{pmatrix} = \frac{1}{g^n_{\kappa 1}(S_n) f^n_{\kappa 2}(S_n) - g^n_{\kappa 2}(S_n) f^n_{\kappa 1}(S_n)}$$

$$\times \begin{pmatrix} f^n_{\kappa 2}(S_n) & -g^n_{\kappa 2}(S_n) \\ -f^n_{\kappa 1}(S_n) & g^n_{\kappa 1}(S_n) \end{pmatrix} \begin{pmatrix} j_l(k_\mu S_n) \\ \dfrac{2\gamma k_\mu}{1+q_\mu} j_{l'}(k_\mu S_n) \end{pmatrix}. \tag{3.12}$$

In summary, the four-component basis function in the RLAPW method, $\Xi^m_\mu(\boldsymbol{s})$, is given in a composite form by

$$\Xi^m_\mu(\boldsymbol{s}) = \begin{cases} \psi^m_\mu(\boldsymbol{s}) & \text{in the interstitial region,} \\ \\ \tilde{\psi}^{m,n}_\mu(\boldsymbol{s}) & \text{within the } n\text{th APW sphere.} \end{cases} \tag{3.13}$$

Both large and small components of the basis function are continuous everywhere in a crystal. As is shown in the next section, the RLAPW basis function thus augmented results in the elimination of the difficulties accompanied with the RAPW method, i.e. matrix elements for the Dirac Hamiltonian and the overlap integral are independent of the energy which should be determined.

3.2.2 *Matrix elements*

In order to obtain the eigenvalues $E_{\boldsymbol{k}}$ for a given wave vector $\boldsymbol{k}$, the relativistic Bloch function is expanded into the sum of $2W_{\boldsymbol{k}}$ linearly independent basis functions having different reciprocal lattice vectors:

$$\Phi_{\boldsymbol{k}}(\boldsymbol{s}) = \sum_{\mu=1}^{W_{\boldsymbol{k}}} \sum_{m=\pm\frac{1}{2}} C^m_\mu \Xi^m_\mu(\boldsymbol{s}). \tag{3.14}$$

The number of the basis functions, $2W_{\boldsymbol{k}}$, should be chosen to be large enough for the eigenvalues to converge well. In the expression of eq. (3.14), the expansion coefficient C_{μ}^{m} is determined by the variational principle. The variational expression valid for this trial function under the Dirac Hamiltonian H is given by

$$E_{\boldsymbol{k}} \int_{\mathrm{I+II}} \Phi_{\boldsymbol{k}}(\boldsymbol{s})^{+} \Phi_{\boldsymbol{k}}(\boldsymbol{s}) \mathrm{d}\tau = \int_{\mathrm{I+II}} \Phi_{\boldsymbol{k}}(\boldsymbol{s})^{+} H \Phi_{\boldsymbol{k}}(\boldsymbol{s}) \mathrm{d}\tau, \tag{3.15}$$

where I and II represent the regions inside and outside the APW spheres in the primitive cell, respectively. Note that in eq. (3.15) there is no surface integral because the trial function itself is continuous at the surface of the APW spheres. By substituting (3.14) into (3.15) and minimizing $E_{\boldsymbol{k}}$ with respect to the expansion coefficients, we obtain a set of $2W_{\boldsymbol{k}}$ equations

$$\sum_{\mu=1}^{W_{\boldsymbol{k}}} \sum_{m'=\pm\frac{1}{2}} \left(H_{\nu\mu}^{mm'} - E_{\boldsymbol{k}} O_{\nu\mu}^{mm'} \right) C_{\mu}^{m'} = 0, \quad \nu = 1,\ 2, \cdots, W_{\boldsymbol{k}}, \quad m = \pm\frac{1}{2}, \tag{3.16}$$

where $H_{\nu\mu}^{mm'}$ and $O_{\nu\mu}^{mm'}$ are the matrix elements of H and the overlap matrix, respectively. The values of $E_{\boldsymbol{k}}$ allowed in eq. (3.16) are given by the roots of the secular equation

$$\left| H_{\nu\mu}^{mm'} - E_{\boldsymbol{k}} O_{\nu\mu}^{mm'} \right| = 0. \tag{3.17}$$

For each eigenvalue, the coefficients C_{μ}^{m} are determined from eq. (3.16) together with the normalization condition for the wave function $\Phi_{\boldsymbol{k}}(\boldsymbol{s})$. Note that both $H_{\nu\mu}^{mm'}$ and $O_{\nu\mu}^{mm'}$ are independent of $E_{\boldsymbol{k}}$. In order to solve this generalized eigenvalue problem by a standard matrix diagonalization

technique, eq. (3.16) must be transformed to a simple eigenvalue problem by the Cholesky decomposition. A detailed technique is studied by Dongarra *et al.* (1984).

To evaluate the matrix elements of the Dirac Hamiltonian and the overlap matrices, many spatial integrations must be performed. As for the integration over the region outside the APW spheres, it is convenient to extend the integration throughout the entire primitive cell while continuing to use the form of the RLAPW basis function in the interstitial region. The integration over the region outside the APW spheres is obtained by subtracting from this result the resulting contribution due to the region inside the APW spheres. As the result, the RLAPW matrix elements are given by

$$\begin{aligned} H_{\nu\mu}^{mm'} &= \varepsilon_\mu \Omega \delta_{\nu\mu}\delta_{mm'} - \frac{1}{2}(\varepsilon_\nu + \varepsilon_\mu)\int_{\mathrm{I}} \psi_\nu^m(\boldsymbol{s})^+ \psi_\mu^{m'}(\boldsymbol{s}) d\tau \\ &+ \sum_{n=1}^{N_t} e^{i(\boldsymbol{K}_\mu - \boldsymbol{K}_\nu)\cdot \boldsymbol{r}_n} \sum_\kappa D_{\kappa\nu\mu}^{mm'} \sum_{\alpha,\beta=1,2} \frac{1}{2}(\varepsilon_{\kappa\alpha}^n + \varepsilon_{\kappa\beta}^n) a_{\kappa\nu\alpha}^{n\,*} a_{\kappa\mu\beta}^n \xi_{\kappa\alpha\beta}^n \ , \end{aligned} \tag{3.18}$$

$$\begin{aligned} O_{\nu\mu}^{mm'} &= \Omega \delta_{\nu\mu}\delta_{mm'} - \int_{\mathrm{I}} \psi_\nu^m(\boldsymbol{s})^+ \psi_\mu^{m'}(\boldsymbol{s}) d\tau \\ &+ \sum_{n=1}^{N_t} e^{i(\boldsymbol{K}_\mu - \boldsymbol{K}_\nu)\cdot \boldsymbol{r}_n} \sum_\kappa D_{\kappa\nu\mu}^{mm'} \sum_{\alpha,\beta=1,2} a_{\kappa\nu\alpha}^{n\,*} a_{\kappa\mu\beta}^n \xi_{\kappa\alpha\beta}^n \ , \end{aligned} \tag{3.19}$$

where Ω is the volume of the primitive cell. In eqs.(3.18) and (3.19), we define

$$\begin{aligned} D_{\kappa\nu\mu}^{mm'} &= \sum_{M=-j}^{j} A_{\nu\kappa M}^{m\,*} A_{\mu\kappa M}^{m'} \\ &= 4\pi|\kappa| P_l(\cos\theta_{\nu\mu})\delta_{mm'} \\ &+ 4\pi i S_\kappa (\hat{\boldsymbol{k}}_\nu \times \hat{\boldsymbol{k}}_\mu)\cdot \langle m|\sigma|m'\rangle P_l'(\cos\theta_{\nu\mu}) \ , \end{aligned} \tag{3.20}$$

and

$$\xi^n_{\kappa\alpha\beta} = \int_0^{S_n} r^2 \mathrm{d}r \left\{ g^n_{\kappa\alpha}(r) g^n_{\kappa\beta}(r) + f^n_{\kappa\alpha}(r) f^n_{\kappa\beta}(r) \right\}$$

$$= \begin{cases} 1 & \text{for } \alpha = \beta \\ \dfrac{S_\kappa {S_n}^2 \left\{ f^n_{\kappa\beta}(S_n) g^n_{\kappa\alpha}(S_n) - f^n_{\kappa\alpha}(S_n) g^n_{\kappa\beta}(S_n) \right\}}{\gamma\left(\varepsilon^n_{\kappa\alpha} - \varepsilon^n_{\kappa\beta}\right)} & \text{for } \alpha \neq \beta \end{cases}, \tag{3.21}$$

where $P_l'(x)$ is the derivative of the Legendre polynomial $P_l(x)$, $\theta_{\nu\mu}$ is the angle between $\boldsymbol{k}_\mu$ and $\boldsymbol{k}_\nu$, and $\hat{\boldsymbol{k}}_\nu$, $\hat{\boldsymbol{k}}_\mu$ are the unit vectors in the direction of $\boldsymbol{k}_\nu$, $\boldsymbol{k}_\mu$ respectively. In eq.(3.21), we assume that the radial wave functions are normalized by the condition

$$\xi^n_{\kappa\alpha\alpha} = \int_0^{S_n} r^2 \mathrm{d}r \left\{ g^n_{\kappa\alpha}(r) g^n_{\kappa\alpha}(r) + f^n_{\kappa\alpha}(r) f^n_{\kappa\alpha}(r) \right\} = 1. \tag{3.22}$$

The results of the integrals in eqs.(3.18) and (3.19) are denoted explicitly as

$$\int_{\mathrm{I}} \psi^m_\nu(\boldsymbol{s})^+ \psi^{m'}_\mu(\boldsymbol{s}) d\tau = \left(\frac{1+q_\nu}{2q_\nu} \right)^{\frac{1}{2}} \left(\frac{1+q_\mu}{2q_\mu} \right)^{\frac{1}{2}} \sum_{n=1}^{N_t} e^{i(\boldsymbol{K}_\mu - \boldsymbol{K}_\nu)\cdot \boldsymbol{r}_n}$$
$$\times \frac{4\pi {S_n}^2}{\left|\boldsymbol{K}_\mu - \boldsymbol{K}_\nu\right|} j_1\left(\left|\boldsymbol{K}_\mu - \boldsymbol{K}_\nu\right| S_n\right)$$
$$\times \left\{ \delta_{mm'} + 4\gamma^2 \frac{\boldsymbol{k}_\nu \cdot \boldsymbol{k}_\mu \delta_{mm'} + i\langle m|\sigma|m'\rangle \cdot \left(\boldsymbol{k}_\nu \times \boldsymbol{k}_\mu\right)}{\left(1+q_\nu\right)\left(1+q_\mu\right)} \right\}. \tag{3.23}$$

So far, any approximations have not been introduced in calculating the matrix elements. Hereafter we will use the same approximation as that introduced by Loucks (1967), which is based on the fact that the

contribution of the small components in the plane wave in the interstitial region is negligibly small, i.e. usually the condition $\hbar k_\mu / m_0 << c$ holds. This approximation is accomplished by neglecting the terms, the magnitude of which is of order γ^2, i.e.

$$\left(\frac{1+q_\mu}{2q_\mu}\right)^{\frac{1}{2}} \approx 1 \ ,$$
$$\frac{k_\mu}{1+q_\mu} \approx \frac{k_\mu}{2} \ ,$$
$$\varepsilon_\mu \approx {k_\mu}^2 + V_0 \ .$$

In this approximation, eq.(3.23) becomes

$$\begin{aligned} &\int_{\mathrm{I}} \psi_\nu^m(\boldsymbol{s})^+ \psi_\mu^{m'}(\boldsymbol{s}) d\tau \\ &\approx \sum_{n=1}^{N_t} e^{i(\boldsymbol{K}_\mu - \boldsymbol{K}_\nu)\cdot \boldsymbol{r}_n} \frac{4\pi {S_n}^2}{\left|\boldsymbol{K}_\mu - \boldsymbol{K}_\nu\right|} j_1\left(\left|\boldsymbol{K}_\mu - \boldsymbol{K}_\nu\right| S_n\right) \delta_{mm'} \ , \end{aligned} \tag{3.24}$$

and eq.(3.12) becomes

$$\begin{aligned} \begin{pmatrix} a^n_{\kappa\mu 1} \\ a^n_{\kappa\mu 2} \end{pmatrix} &\approx \frac{1}{g^n_{\kappa 1}(S_n) f^n_{\kappa 2}(S_n) - g^n_{\kappa 2}(S_n) f^n_{\kappa 1}(S_n)} \\ &\times \begin{pmatrix} f^n_{\kappa 2}(S_n) & -g^n_{\kappa 2}(S_n) \\ -f^n_{\kappa 1}(S_n) & g^n_{\kappa 1}(S_n) \end{pmatrix} \begin{pmatrix} j_l(k_\mu S_n) \\ \gamma\, k_\mu j_{l'}(k_\mu S_n) \end{pmatrix} . \end{aligned} \tag{3.25}$$

Consequently the matrix elements of the Hamiltonian and the overlap matrices are expressed as

$$H_{\nu\mu}^{mm'} = \left[\left(k_\mu{}^2 + V_0\right)\Omega\delta_{\nu\mu} - \left\{\frac{1}{2}(k_\nu{}^2 + k_\mu{}^2) + V_0\right\} I_{\nu\mu}\right]\delta_{mm'}$$
$$+ \sum_{p=1}^{P}\left\{\sum_{i=1}^{N_p} e^{i(\boldsymbol{K}_\mu - \boldsymbol{K}_\nu)\cdot\boldsymbol{r}_i}\right\}\sum_{\kappa} D_{\kappa\nu\mu}^{mm'} \sum_{\alpha,\beta=1,2}\frac{1}{2}(\varepsilon_{\kappa\alpha}^{p} + \varepsilon_{\kappa\beta}^{p}) a_{\kappa\nu\alpha}^{p}{}^{*} a_{\kappa\mu\beta}^{p}\xi_{\kappa\alpha\beta}^{p} \ , \tag{3.26}$$

$$O_{\nu\mu}^{mm'} = \left\{\Omega\delta_{\nu\mu} - I_{\nu\mu}\right\}\delta_{mm'}$$
$$+ \sum_{p=1}^{P}\left\{\sum_{i=1}^{N_p} e^{i(\boldsymbol{K}_\mu - \boldsymbol{K}_\nu)\cdot\boldsymbol{r}_i}\right\}\sum_{\kappa} D_{\kappa\nu\mu}^{mm'} \sum_{\alpha,\beta=1,2} a_{\kappa\nu\alpha}^{p}{}^{*} a_{\kappa\mu\beta}^{p}\xi_{\kappa\alpha\beta}^{p} \ , \tag{3.27}$$

where

$$I_{\nu\mu} \equiv \sum_{p=1}^{P}\left\{\sum_{i=1}^{N_p} e^{i(\boldsymbol{K}_\mu - \boldsymbol{K}_\nu)\cdot\boldsymbol{r}_i}\right\}\frac{4\pi S_p{}^2}{\left|\boldsymbol{K}_\mu - \boldsymbol{K}_\nu\right|} j_1\left(\left|\boldsymbol{K}_\mu - \boldsymbol{K}_\nu\right| S_p\right) \ . \tag{3.28}$$

It should be noted in eqs.(3.26), (3.27) and (3.28) that the sum over the individual atoms in the primitive cell are replaced by two sums, one of which is over the kind of atoms and denoted as the sum over p, and another of which is over the individual atoms of the pth type and denoted as the sum over i.

Next, we convert the sum over κ into the sum over l which are related each other by eq.(3.6). We have

$$
\begin{aligned}
H_{\nu\mu}^{mm'} = & \left\{ \left(k_\mu^2 + V_0 \right) \Omega \delta_{\nu\mu} - \left(\frac{k_\nu^2 + k_\mu^2}{2} + V_0 \right) I_{\nu\mu} \right\} \delta_{mm'} \\
& + \sum_{p=1}^{P} \left\{ \sum_{i=1}^{N_p} e^{i(\boldsymbol{K}_\mu - \boldsymbol{K}_\nu)\cdot \boldsymbol{r}_i} \right\} \sum_{l=0}^{l_{\max}} 4\pi P_l(\cos\theta_{\nu\mu}) \\
& \times \sum_{\alpha,\beta=1,2} \left\{ l \left(\frac{\varepsilon_{l\alpha}^p + \varepsilon_{l\beta}^p}{2} \right) a_{l\nu\alpha}^p a_{l\mu\beta}^p \xi_{l\alpha\beta}^p \right. \\
& \qquad \left. + (l+1) \left(\frac{\varepsilon_{-l-1,\alpha}^p + \varepsilon_{-l-1,\beta}^p}{2} \right) a_{-l-1,\nu\alpha}^p a_{-l-1,\mu\beta}^p \xi_{-l-1,\alpha\beta}^p \right\} \delta_{mm'} \\
& + \sum_{p=1}^{P} \left\{ \sum_{i=1}^{N_p} e^{i(\boldsymbol{K}_\mu - \boldsymbol{K}_\nu)\cdot \boldsymbol{r}_i} \right\} \sum_{l=0}^{l_{\max}} 4\pi i (\hat{\boldsymbol{k}}_\nu \times \hat{\boldsymbol{k}}_\nu) \cdot \langle m | \sigma | m' \rangle P_l'(\cos\theta_{\nu\mu}) \\
& \times \sum_{\alpha,\beta=1,2} \left\{ \left(\frac{\varepsilon_{l\alpha}^p + \varepsilon_{l\beta}^p}{2} \right) a_{l\nu\alpha}^p a_{l\mu\beta}^p \xi_{l\alpha\beta}^p \right. \\
& \qquad \left. - \left(\frac{\varepsilon_{-l-1,\alpha}^p + \varepsilon_{-l-1,\beta}^p}{2} \right) a_{-l-1,\nu\alpha}^p a_{-l-1,\mu\beta}^p \xi_{-l-1,\alpha\beta}^p \right\} ,
\end{aligned}
\tag{3.29}
$$

and

$$
\begin{aligned}
O_{\nu\mu}^{mm'} = & \left\{ \Omega \delta_{\nu\mu} - I_{\nu\mu} \right\} \delta_{mm'} \\
& + \sum_{p=1}^{P} \left\{ \sum_{i=1}^{N_p} e^{i(\boldsymbol{K}_\mu - \boldsymbol{K}_\nu)\cdot \boldsymbol{r}_i} \right\} \sum_{l=0}^{l_{\max}} 4\pi P_l(\cos\theta_{\nu\mu}) \\
& \times \sum_{\alpha,\beta=1,2} \left\{ l a_{l\nu\alpha}^p a_{l\mu\beta}^p \xi_{l\alpha\beta}^p + (l+1) a_{-l-1,\nu\alpha}^p a_{-l-1,\mu\beta}^p \xi_{-l-1,\alpha\beta}^p \right\} \delta_{mm'} \\
& + \sum_{p=1}^{P} \left\{ \sum_{i=1}^{N_p} e^{i(\boldsymbol{K}_\mu - \boldsymbol{K}_\nu)\cdot \boldsymbol{r}_i} \right\} \sum_{l=0}^{l_{\max}} 4\pi i (\hat{\boldsymbol{k}}_\nu \times \hat{\boldsymbol{k}}_\nu) \cdot \langle m | \sigma | m' \rangle P_l'(\cos\theta_{\nu\mu}) \\
& \times \sum_{\alpha,\beta=1,2} \left\{ a_{l\nu\alpha}^p a_{l\mu\beta}^p \xi_{l\alpha\beta}^p - a_{-l-1,\nu\alpha}^p a_{-l-1,\mu\beta}^p \xi_{-l-1,\alpha\beta}^p \right\} .
\end{aligned}
\tag{3.30}
$$

These expressions for the matrix elements are useful to understand the relativistic effects, especially the spin-orbit interaction, since the diagonal

and off-diagonal terms with respect to the spin argument are exhibited separately and explicitly. The term which involves the cross product $\left(\hat{\boldsymbol{k}}_\nu \times \hat{\boldsymbol{k}}_\mu\right)$ in eqs.(3.29)and (3.30) originate from the spin-orbit interaction. The expressions in eqs.(3.29) and (3.30) are also convenient to compare with the nonrelativistic expressions which Takeda and Kubler have proposed (Takeda and Kubler 1979). It is easy to prove that the matrix elements in the RLAPW method reduce to those in the LAPW method in the limit $c \to \infty$, and its proof is given in Appendix A.

For the sake of a computational purpose, we define some useful matrix elements such as $A_{\nu\mu}$, $B^{l,p}_{\nu\mu,\alpha\beta}$, $C^{l,p}_{\nu\mu,\alpha\beta}$, $F^{l,p}_{\nu\mu,\alpha\beta}(m,m')$ and $G^{l,p}_{\nu\mu,\alpha\beta}(m,m')$. Using these matrix elements, eqs. (3.29) and (3.30) are written as

$$
\begin{aligned}
H^{mm'}_{\nu\mu} = & \left\{\frac{1}{2}(k_\nu{}^2 + k_\mu{}^2) + V_0\right\}\left(\Omega\delta_{\nu\mu} - A_{\nu\mu}\right)\delta_{mm'} \\
& + \frac{1}{2}\sum_{l=0}^{l_{\max}}\sum_{\alpha,\beta=1,2}\sum_{p=1}^{P}\left\{\left(\varepsilon^p_{l\alpha} + \varepsilon^p_{l\beta}\right)\xi^p_{l\alpha\beta}B^{l,p}_{\nu\mu,\alpha\beta}\right. \\
& \qquad \left. + \left(\varepsilon^p_{-l-1,\alpha} + \varepsilon^p_{-l-1,\beta}\right)\xi^p_{-l-1,\alpha\beta}C^{l,p}_{\nu\mu,\alpha\beta}\right\}\delta_{mm'} \\
& + \frac{1}{2}\sum_{l=1}^{l_{\max}}\sum_{\alpha,\beta=1,2}\sum_{p=1}^{P}\left\{\left(\varepsilon^p_{l\alpha} + \varepsilon^p_{l\beta}\right)\xi^p_{l\alpha\beta}F^{l,p}_{\nu\mu,\alpha\beta}(m,m')\right. \\
& \qquad \left. - \left(\varepsilon^p_{-l-1,\alpha} + \varepsilon^p_{-l-1,\beta}\right)\xi^p_{-l-1,\alpha\beta}G^{l,p}_{\nu\mu,\alpha\beta}(m,m')\right\},
\end{aligned}
\tag{3.31}
$$

and

$$
\begin{aligned}
O^{mm'}_{\nu\mu} = & \left(\Omega\delta_{\nu\mu} - A_{\nu\mu}\right)\delta_{mm'} + \sum_{l=0}^{l_{\max}}\sum_{\alpha,\beta=1,2}\sum_{p=1}^{P}\left(\xi^p_{l\alpha\beta}B^{l,p}_{\nu\mu,\alpha\beta} + \xi^p_{-l-1,\alpha\beta}C^{l,p}_{\nu\mu,\alpha\beta}\right)\delta_{mm'} \\
& + \sum_{l=1}^{l_{\max}}\sum_{\alpha,\beta=1,2}\sum_{p=1}^{P}\left\{\xi^p_{l\alpha\beta}F^{l,p}_{\nu\mu,\alpha\beta}(m,m') - \xi^p_{-l-1,\alpha\beta}G^{l,p}_{\nu\mu,\alpha\beta}(m,m')\right\},
\end{aligned}
\tag{3.32}
$$

where

$$A_{\nu\mu} = 4\pi \sum_{p=1}^{P} \left\{ \left(\sum_{i=1}^{N_p} e^{i(\boldsymbol{K}_\mu - \boldsymbol{K}_\nu)\cdot \boldsymbol{r}_i} \right) S_p^2 \frac{j_1(|\boldsymbol{K}_\mu - \boldsymbol{K}_\nu| S_p)}{|\boldsymbol{K}_\mu - \boldsymbol{K}_\nu|} \right\}, \tag{3.33}$$

$$B^{l,p}_{\nu\mu,\alpha\beta} = 4\pi \left(\sum_{i=1}^{N_p} e^{i(\boldsymbol{K}_\mu - \boldsymbol{K}_\nu)\cdot \boldsymbol{r}_i} \right) P_l(\cos\theta_{\nu\mu}) l a^p_{l\nu\alpha} a^p_{l\mu\beta}, \tag{3.34}$$

$$C^{l,p}_{\nu\mu,\alpha\beta} = 4\pi \left(\sum_{i=1}^{N_p} e^{i(\boldsymbol{K}_\mu - \boldsymbol{K}_\nu)\cdot \boldsymbol{r}_i} \right) P_l(\cos\theta_{\nu\mu}) (l+1) a^p_{-l-1,\nu\alpha} a^p_{-l-1,\mu\beta}, \tag{3.35}$$

$$\begin{aligned} F^{l,p}_{\nu\mu,\alpha\beta}(m,m') = 4\pi i & \left(\sum_{i=1}^{N_p} e^{i(\boldsymbol{K}_\mu - \boldsymbol{K}_\nu)\cdot \boldsymbol{r}_i} \right) \left(\hat{\boldsymbol{k}}_\nu \times \hat{\boldsymbol{k}}_\mu \right) \cdot \langle m|\sigma|m' \rangle \\ & \times P_l'(\cos\theta_{\nu\mu}) a^p_{l\nu\alpha} a^p_{l\mu\beta}, \end{aligned} \tag{3.36}$$

and

$$\begin{aligned} G^{l,p}_{\nu\mu,\alpha\beta}(m,m') = 4\pi i & \left(\sum_{i=1}^{N_p} e^{i(\boldsymbol{K}_\mu - \boldsymbol{K}_\nu)\cdot \boldsymbol{r}_i} \right) \left(\hat{\boldsymbol{k}}_\nu \times \hat{\boldsymbol{k}}_\mu \right) \cdot \langle m|\sigma|m' \rangle \\ & \times P_l'(\cos\theta_{\nu\mu}) a^p_{-l-1,\nu\alpha} a^p_{-l-1,\mu\beta}, \end{aligned} \tag{3.37}$$

Note that in eqs. (3.31) and (3.32) the sum of terms which involves $B^{l,p}_{\nu\mu,\alpha\beta}$ over l may start from l=0, though $B^{l,p}_{\nu\mu,\alpha\beta}$ originally is not defined at l=0, because it is proportional to l as is shown in eq. (3.34).

3.2.3 *The charge density*

In order to perform the energy band calculation self-consistently, it is necessary to calculate the charge density associated with the RLAPW functions. In the MTA, it consists of a spherically averaged radial density $\rho_p(r)$ within the pth-type APW sphere and a constant charge density ρ_0 in the interstitial region. To obtain $\rho_p(r)$, it is necessary to calculate the probability amplitude of the eigenstate at many sampling points of $\boldsymbol{k}$ and

average over the occupied states. The weighting factors $\lambda_{\boldsymbol{k}}$ are determined by taking the order of the group of $\boldsymbol{k}$ into account.

For the wave vector $\boldsymbol{k}$, we define a spherically averaged radial density function $\rho_p^{\boldsymbol{k},n}(r)$ within the pth-type APW sphere which belongs to the nth band by the following integration

$$\begin{aligned}\rho_p^{\boldsymbol{k},n}(r) &= \frac{1}{4\pi N_p}\int_{4\pi}\Phi_{\boldsymbol{k},n}(\boldsymbol{r})^{+}\Phi_{\boldsymbol{k},n}(\boldsymbol{r})\mathrm{d}o \\ &= \frac{1}{4\pi N_p N_{\boldsymbol{k},n}}\sum_{\nu,\mu=1}^{W_{\boldsymbol{k}}}\sum_{m,m'=\pm 1/2} C_\nu^{m\,*} C_\mu^{m'} \sum_{l=0}^{l_{\max}}\sum_{\alpha,\beta=1,2} \\ &\quad \Big[\Big\{B_{\nu\mu,\alpha\beta}^{l,p}\zeta_{\nu\mu,\alpha\beta}^{l,p}(r)+C_{\nu\mu,\alpha\beta}^{l,p}\zeta_{\nu\mu,\alpha\beta}^{-l-1,p}(r)\Big\}\delta_{mm'} \\ &\quad +F_{\nu\mu,\alpha\beta}^{l,p}(m,m')\zeta_{\nu\mu,\alpha\beta}^{l,p}(r)-G_{\nu\mu,\alpha\beta}^{l,p}(m,m')\zeta_{\nu\mu,\alpha\beta}^{-l-1,p}(r)\Big],\end{aligned} \tag{3.38}$$

where the integration is performed over solid angles within each of the N_p APW spheres. In eq. (3.38) we define

$$\zeta_{\nu\mu,\alpha\beta}^{l,p}(r) = r^2\Big\{g_{l\alpha}^{p}(r)g_{l\beta}^{p}(r)+f_{l\alpha}^{p}(r)f_{l\beta}^{p}(r)\Big\}. \tag{3.39}$$

In eq. (3.38) C_ν^m implies the coefficients which are determined for the nth band at $\boldsymbol{k}$. The expression of the norm $N_{\boldsymbol{k},n}$ is given in Appendix B.

By its definition, the Fermi energy E_{F} is determined on the condition that the sum of $\lambda_{\boldsymbol{k}}$ over all states whose eigenvalue is less than E_{F} should be equal to the total number of the valence electrons in the primitive cell, N_{e}, i.e.

$$\sum_{n\ (E_{\boldsymbol{k},n}\le E_{\mathrm{F}})}\ \sum_{\boldsymbol{k}}\lambda_{\boldsymbol{k}} = N_{\mathrm{e}}, \tag{3.40}$$

where $E_{\boldsymbol{k},n}$ is the energy of the nth band at $\boldsymbol{k}$.

The spherically averaged radial density $\rho_p(r)$ is obtained by summing $\rho_p^{\boldsymbol{k},n}(r)$ over all occupied states as

$$\rho_p(r) = \rho_{p,\text{core}}(r) + \sum_{\substack{n \\ (E_{\boldsymbol{k},n} \le E_F)}} \sum_{\boldsymbol{k}} \lambda_{\boldsymbol{k}} \rho_p^{\boldsymbol{k},n}(r). \tag{3.41}$$

The first term on the right-hand side represents the radial charge density of all the core electrons within the pth APW sphere. The second term on the right-hand side represents an average of $\rho_p^{\boldsymbol{k},n}(r)$ with a weighting factor $\lambda_{\boldsymbol{k}}$ over all the occupied states.

In the interstitial region, the constant charge density ρ_0 is determined in order to keep the primitive cell electrically neutral as

$$\rho_0 = \left(N_e - 4\pi \sum_{p=1}^{P} N_p \int_0^{S_p} \rho_p(r) r^2 dr \right) \Bigg/ \left(\Omega - \sum_{p=1}^{P} N_p \frac{4\pi S_p^3}{3} \right). \tag{3.42}$$

3.2.4 *The procedure of a self-consistent calculation*

The procedure of a self-consistent calculation requires an initial charge density. An initial charge density for a crystal is constructed by superposing the self-consistent atomic charge densities, which are calculated for the neutral constituent atoms using the method of Liberman *et al.* (1965). Once the muffin-tin charge density has been determined, the corresponding Hartree potential and the exchange-correlation potential can be calculated in a manner similar to the ordinary non-relativistic band calculations. The details of the method are given in the review by Mattheiss *et al.* (1968). In Appendix C, we rewrite the resultant forms of one-electron potential energy function.

In the RLAPW method, we must choose the sets of the energy values $\left(\varepsilon_{l1}^p,\ \varepsilon_{l2}^p\right)$ and $\left(\varepsilon_{-l-1,1}^p,\ \varepsilon_{-l-1,2}^p\right)$ appropriately for each l and for each kind of

atoms before the calculation of the matrix elements in eqs. (3.31) and (3.32). The matrix elements for each of the sampling mesh points of $\boldsymbol{k}$ in the irreducible Brillouin zone are then constructed, and the secular equation is solved in order to obtain the new eigenvalues and eigenstates. The new charge density is constructed from the RLAPW functions in the way we have explained in the previous section.

The new charge density will usually depart from the one originally used to construct the one-electron potential energy function. Hence the new set of the Hamiltonian and overlap matrices must be constructed by using the new charge density. The eigenstates and the corresponding charge densities for the new Hamiltonian and overlap matrices are obtained, and the process is repeated until the solutions become self-consistent. In order to optimize the convergence of the self-consistent iterations, the new charge density $\rho_p(r)_{\text{new}}$ within the pth type APW sphere is in practice taken to be an appropriate linear combination of the charge densities, $\rho_p(r)_{\text{in}}$ and $\rho_p(r)_{\text{out}}$, where $\rho_p(r)_{\text{in}}$ and $\rho_p(r)_{\text{out}}$ mean the input and output charge densities within the pth type APW sphere, respectively, i.e.

$$\rho_p(r)_{\text{new}} = \omega\rho_p(r)_{\text{in}} + (1-\omega)\rho_p(r)_{\text{out}}, \tag{3.43}$$

where ω is the mixing coefficient. For the f-electron compounds, the coefficient ω generally should take the value close to unity because the f bands are very sensitive to a small change in the one-electron potential.

In this thesis, the parametrization of Gunnarsson and Lundqvist (1976) has been used as the functional form of the exchange-correlation potential.

Fig 3.2 shows the flow chart to calculate the electronic structures and the Fermi surface in the RLAPW method. In order to observe the advantages in the RLAPW method definitely, the flow chart for the self-

consistent calculations in the RAPW method is also shown in Fig. 3.3. It can be seen that much less calculation time is spent by the RLAPW method than by the RAPW method.

To obtain the density of states and the Fermi surface, the eigenvalues thus calculated are converted into energies at finer meshes with an interpolation by the Fourier series expansion. The density of states is calculated by the aid of the tetrahedron method (Jepson and Anderson 1971 ; Rath and Freeman 1975). The Fermi surface is represented in perspective by the aid of the computer program "TPERSP" made by A. Yanase at the Tohoku University Computer Center.

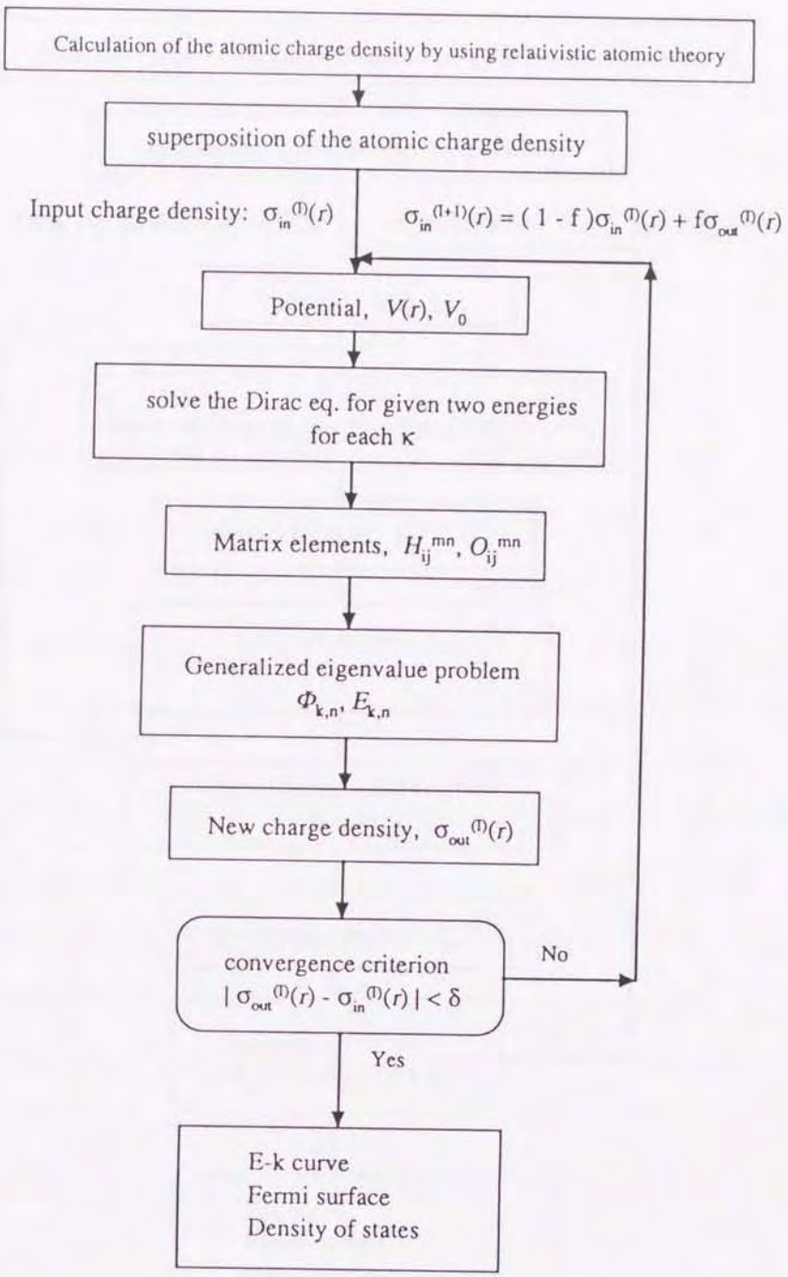

Figure 3.2. The flow chart for the self-consistent calculation in the RLAPW method

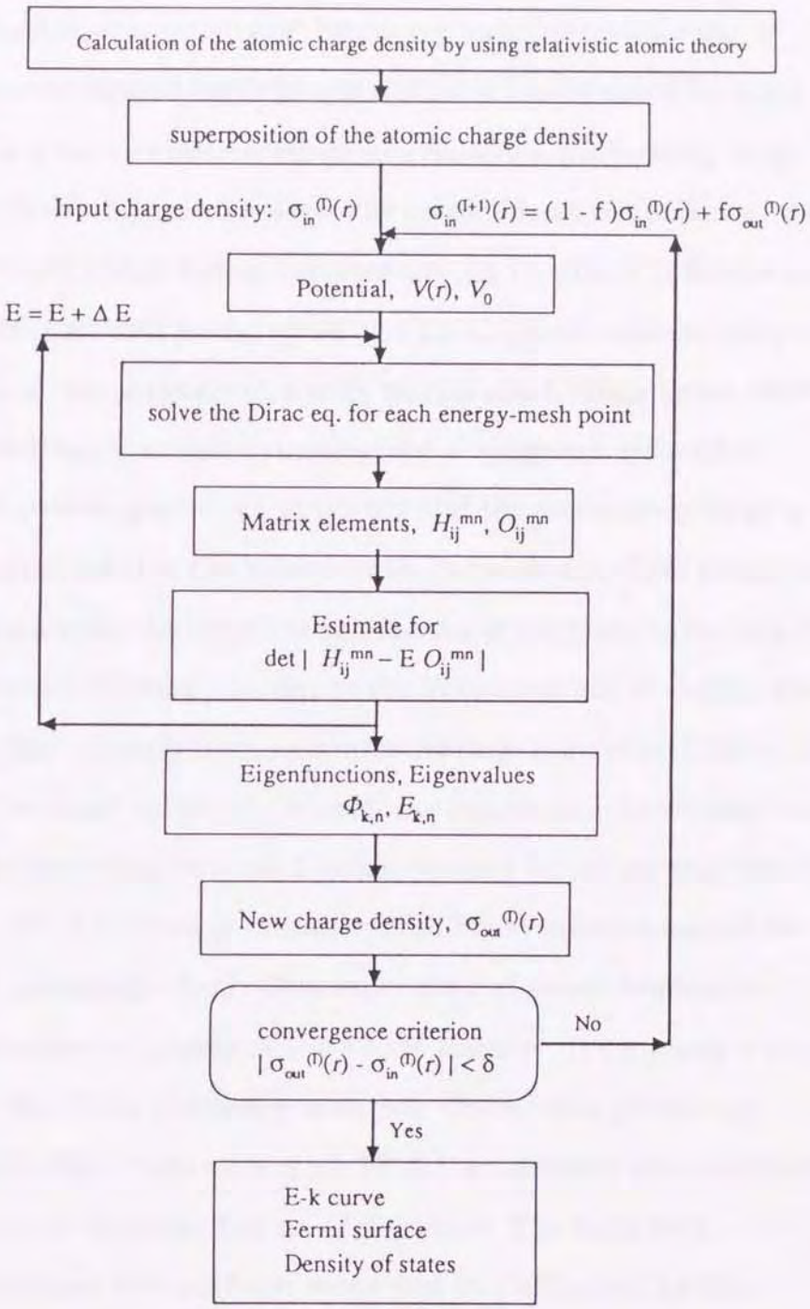

Figure 3.3. The flow chart for the self-consistent calculation in the RAPW method

4. The Fermi Surface of the Itinerant 4*f* Electrons in $CeRh_2$

4.1. *Introduction*

In this chapter, the validity of the energy band picture for the 4*f* electrons is investigated on $CeRh_2$ in the cubic Laves phase by band theory. It is a heavy-electron compound having a moderately large value of the low-temperature electronic specific heat coefficient γ (= 20 mJ/K^2 mol) and a high Kondo temperature T_K (= 400 K) (Sugawara et al. 1994). It is a Pauli paramagnet and its magnetic susceptibility is independent of temperature in a wide temperature range below 400K. It undergoes neither a superconducting nor a magnetic transition.

From the paramagnetic susceptibility and the moderately large γ value, it is expected that the hybridization between the Ce 4*f* states and the Rh 4*d* states may be large enough for the 4*f* electrons to become the Bloch electrons in $CeRh_2$. To clarify the Fermi surface of $CeRh_2$, the dHvA effect has recently been measured by Sugawara *et al.* (1994). Though the residual resistivity ratio of the sample is only 20, they have succeeded in observing several dHvA frequency branches and revealing that all the dHvA frequency branches are almost independent of the direction of a magnetic field. The experimental result implies the existence of spherical sheets of the Fermi surface. It contrasts with the behavior of the dHvA frequency branches which were previously observed in $LaRh_2$ (Sugawara *et al.* 1993), a reference material having the same crystal structure but no 4*f* electrons. The high-field magnetoresistance has not been measured in $CeRh_2$ nor $LaRh_2$.

On the basis of an itinerant 4*f*-electron model, the energy band structure was previously calculated for a series of the Ce compounds in the cubic Laves phase including $CeRh_2$ using an APW method by Yanase (1986). The relativistic energy shifts were taken into account, but the spin-orbit interaction was neglected. The hybridization between

the 4*f* states and the Rh 4*d* states and its effect on the density of states were studied. Though the existence of the spherical sheets of the Fermi surface can be read in the E-$\boldsymbol{k}$ relations around the Γ point in the vicinity of the Fermi level (Fig. 7 of Yanase (1986)), the Fermi surface property was not published for $CeRh_2$. An analysis of the experimental result for the dHvA effect demands a detailed knowledge of the Fermi surface, and it should be derived by a fully relativistic band theory, because the relativistic effects including the spin-orbit interaction are important in such heavy atoms as Ce and Rh.

We apply a relativistic self-consistent APW method to calculate the energy band structure and the Fermi surface for $CeRh_2$ on the assumption that the 4*f* electrons are itinerant, and then try to explain the experimental result for the dHvA effect. As a result of the calculation, we find that the Fermi surface consists of three simple sheets, i.e. two small hole spheres and a hollow electron sphere. The spherical property of these sheets of the Fermi surface explains the behavior of the experimental dHvA frequency branches qualitatively well, though the magnitude of the experimental cyclotron effective masses cannot be explained reasonably well.

Unfortunately, it is evident from an apparent experimental inconsistency between the γ value and the magnitude of the cyclotron effective masses that some of the major dHvA frequency branches may be missed in the measurement by Sugawara *et al.* (1994) because of a limitation of the sample purity. This makes it difficult to confirm the validity of whole the theoretical Fermi surface. Therefore, at the present stage it is not possible to draw such a clear-cut conclusion on the itinerant nature of the 4*f* electrons in $CeRh_2$ as in $CeSn_3$.

4.2 *Method of Calculation*

$CeRh_2$ has the $MgCu_2$ crystal structure which belongs to the cubic Laves-phase (Fig. 4.1). In this crystal structure, the Ce atoms form a diamond sublattice, which consists of two interpenetrating FCC lattices, and the Rh tetrahedra fill up vacant corners in the Ce sublattice. All atoms pack quite closely. It has the non-symmorphic space group Fd3m and contains two molecules per primitive cell. The lattice constant and other crystal constants (Villars and Calvert 1986) are listed in Table 4.I.

The shape of the one-electron potential is determined in the MTA. The radii of the APW spheres are chosen to be as large as possible unless they overlap each other. The Ce APW sphere radius is the half of the nearest-neighbor Ce-Ce distance, $(3/64)^{1/2}a$, and the Rh APW sphere radius is the half of the nearest-neighbor Rh-Rh distance, $(2/64)^{1/2}a$, where a is the lattice constant, i.e. the third-neighbor Ce-Ce distance. The Ce APW spheres, the Rh APW spheres and the interstitial region occupy 34%, 37% and 29% of the whole space in a crystal, respectively.

The starting crystal charge density for the self-consistent iteration process is constructed by a superposition of the relativistic charge densities for the neutral atoms Ce (Xe, $4f^1 5d^1 6s^2$) and Rh (Kr, $4d^8 5s^1$), where Xe and Kr imply the atomic configurations of xenon and krypton, respectively, which are generated by the self-consistent relativistic calculations for atoms (Liberman *et al.* 1965). In the atomic calculations, the same exchange-correlation potential is used as in the crystal. During the iterations, the frozen-core approximation is adopted, i.e. the atomic charge densities of the Xe core except the $5p^6$ states for Ce and the Kr core for Rh are assumed to represent the core electrons in the crystal. In the relativistic atomic calculations, the spin-orbit splitting in the Ce $4f$, Ce $5d$ and Rh $4d$ state is found to be 21 mRyd., 11 mRyd. and 29 mRyd., respectively.

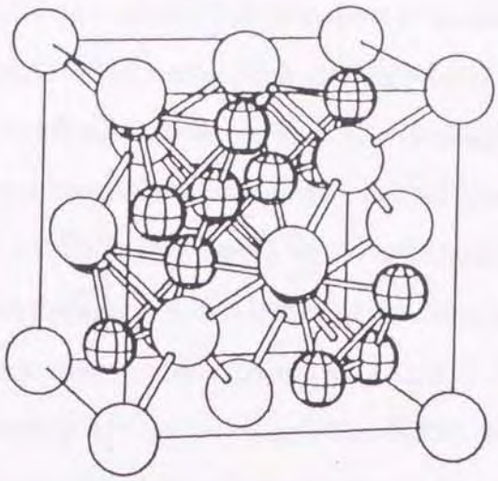

Figure 4.1. Crystal structure of $CeRh_2$ in the cubic Laves-phase. Spheres with and without a pattern show the position of the Rh atoms and the Ce atoms, respectively.

Table 4.I. Crystal constants used in the calculation for $CeRh_2$. The lattice constant and the atomic positions are taken from Villars and Calvert (1986). The origin of coordinates is set at a center of the nearest-neighbour Ce-Ce line.

Crystal structure	$MgCu_2$-type
Space group	Fd3m (No. 227, O_h^7)
Lattice constant, a	7.547 Å (= 14.261762 a.u.)
Atom positions Ce	±1/8, 1/8, 1/8)
Rh	(0, 0, 1/2)
	(1/4, 0, 3/4)
	(0, 1/4, 3/4)
	(1/4, 1/4, 1/2)
Ce APW sphere radius	0.216506 a (= 3.087762 a.u.)
Rh APW sphere radius	0.176777 a (= 2.521147 a.u.)

In each cycle of the self-consistent iteration processes, a new crystal charge density is constructed using 19 $\boldsymbol{k}$ points which are distributed uniformly over the irreducible 1/48 parts of the Brillouin zone. At each $\boldsymbol{k}$ in the Brillouin zone, about 500 plane waves are adopted under the condition $| \boldsymbol{k} + \boldsymbol{G} | < 7.7(2\pi/a)$, where Γ is a reciprocal lattice vector, and angular momenta up to $l_{max} = 8$ are taken into account. They give the eigenvalues which converge well within a few mRyd. The convergence criterion for iterations is $|rV_{in}(r) - rV_{out}(r)| < 0.001$, where $V_{in}(r)$ and $V_{out}(r)$ mean the input potential and the output potential, respectively, and then 77 iterations are demanded.

Using the final self-consistent charge density, eigenvalues are calculated at many symmetry and general points, totally at 263 points in the irreducible 1/48 parts of the Brillouin zone.

4.3 *Results of Calculation*

The energy band structure has been calculated for $CeRh_2$ by the method described in the last section. The Fermi surface is then derived from the energy band structure and its extremal cross-sections are examined carefully. Results of the calculations are explained in the following. In addition, a preliminary calculation has been carried out for $LaRh_2$.[1] Relationship between both compounds is somewhat similar to that which we found previously between $CeSn_3$ and $LaSn_3$ (Hasegawa and Yamagami 1991). Comparison between these compounds will be made briefly in the following. Some results will be compared with results in the previous calculation in which the spin-orbit interaction was neglected (Yanase 1986).

4.3.1 *Fully relativistic energy band structure*

[1] Higuchi and Hasegawa : in preparation.

Figure 4.2 shows the energy band structure of $CeRh_2$ along the principal symmetry axes in the Brillouin zone in the energy range from 0.2 Ryd. to 1.0 Ryd. The six Ce 5*p* bands lie in the energy range between -0.71 Ryd. and -0.45 Ryd. and are omitted from Fig. 4.2. The Fermi energy E_F is located at 0.701451 Ryd. and shown by a dashed line in Fig. 4.2. In order to investigate the character of each band, the charge distributions for many states at the Γ point are partitioned according to the sites and the angular momenta and listed in Table 4.II. The Bloch states which have the Rh *d* components dominantly lie in the wide energy range from 0.2 Ryd. to E_F. In Fig. 4.2, fourteen flat bands lie in the narrow energy range just above E_F. These flat bands consist dominantly of the Ce *f* states and therefore are identified as the *f* bands that the 4*f* states form. The total width of the *f* bands amounts to 0.05 Ryd. and they apparently separate into two subbands which correspond to the total angular momenta j = 5/2 and 7/2. The separation energy is about 0.03 Ryd. which nearly equals to the spin-orbit splitting of the 4*f* state in the Ce atom.

In the previous calculation in which the spin-orbit interaction was neglected (Yanase 1986), the 22nd band and the 23 band are degenerate along the L axis. It is seen in Fig. 4.2 that the doubly degenerate band is split into two bands by the spin-orbit interaction. Many crossings of bands which exist along the Δ and Σ axes in the vicinity of E_F in the previous calculation are also removed out.

The itinerant nature of the 4*f* electrons originates mainly from the hybridization of the Ce 4*f* state and the Rh 4*d* state, which occurs the most appreciably in the vicinity of the Γ point in the Brillouin zone. Due to the 4*f*-4*d* hybridization effect, some amounts of the Ce *f* states are distributed in an upper part of the Rh *d* bands. The Fermi level is

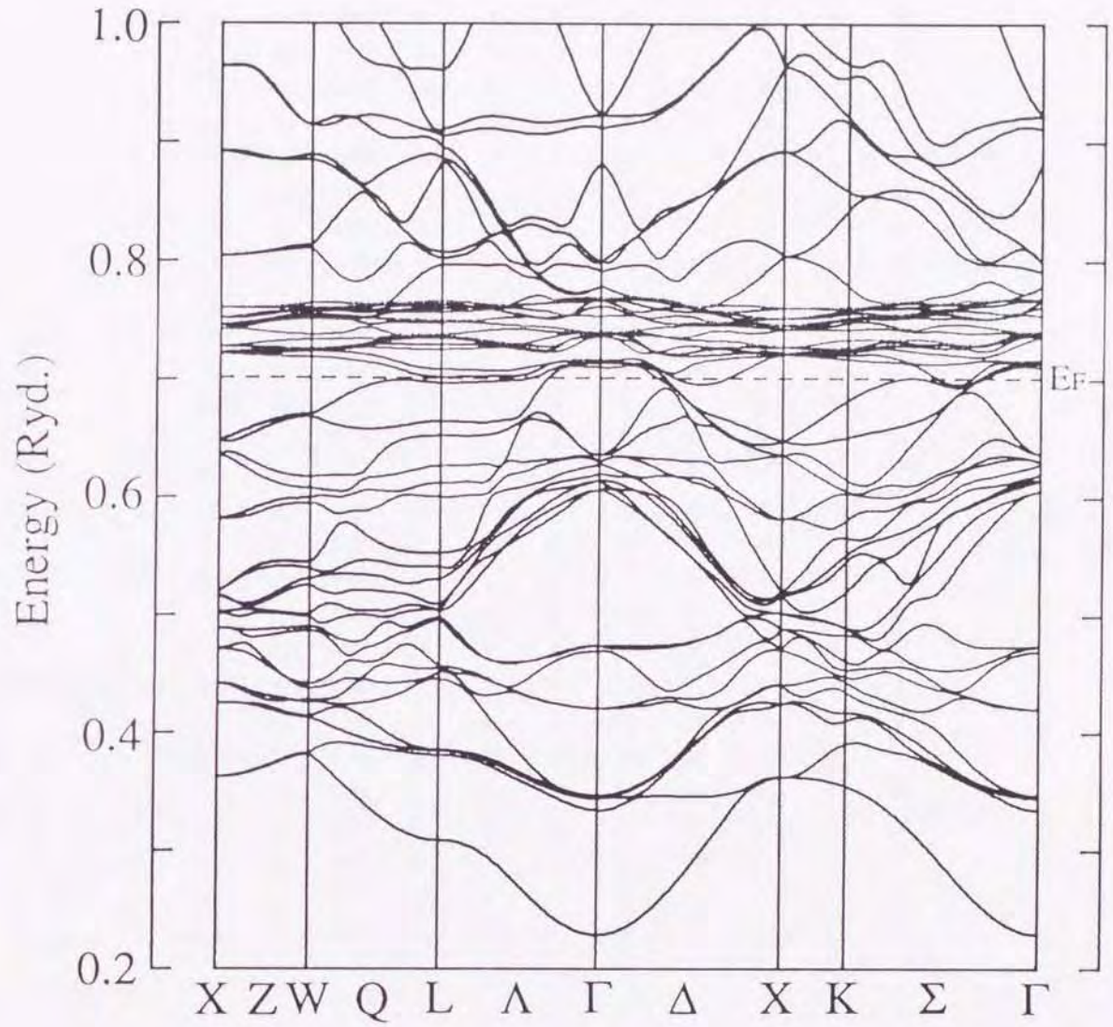

Figure 4.2. Energy band structure calculated for $CeRh_2$ with a self-consistent relativistic APW method. E_F shows the Fermi energy.

Table 4.II. Charge distributions partitioned into the APW spheres and the angular momenta for the Bloch states at the Γ points for $CeRh_2$. Components are given in percent.

Band	Bloch	Energy	outer	Ce sheres				Rh spheres		
index	state	(Ryd.)	region	s	p	d	f	s	p	d
1	Γ_6^+	0.229	27	7	0	0	0	42	0	23
2	Γ_6^+	0.334	23	14	0	0	0	5	0	58
3	Γ_7^+	0.344	16	0	0	5	2	8	0	68
4,5	Γ_8^+	0.347	16	0	0	5	2	8	0	68
6,7	Γ_8^+	0.421	10	0	0	1	0	0	0	88
8	Γ_7^+	0.470	15	0	7	1	0	2	0	75
9,10	Γ_8^+	0.475	13	0	7	1	0	2	0	77
11,12	Γ_8^+	0.606	7	0	0	6	7	2	0	78
13,14	Γ_8^+	0.615	5	0	0	0	5	0	0	89
15	Γ_7^+	0.621	6	0	0	4	7	1	0	81
16	Γ_6^+	0.629	5	0	0	0	7	0	0	87
17,18	Γ_8^-	0.631	31	0	0	53	0	0	15	0
19,20	Γ_8^+	0.637	5	0	0	4	2	0	0	88
21	Γ_7^-	0.710	3	0	0	0	96	0	1	0
22,23	Γ_8^-	0.714	3	0	0	0	97	0	0	0
24	Γ_6^+	0.717	1	1	0	0	97	0	0	1
25,26	Γ_8^+	0.737	1	0	0	4	88	0	0	7
27	Γ_6^-	0.739	20	0	6	14	46	0	13	0
28	Γ_7^-	0.740	6	1	0	0	85	0	7	0
29,30	Γ_8^-	0.741	5	0	1	2	90	0	2	0
31	Γ_7^+	0.754	1	0	0	4	89	0	0	5
32	Γ_6^+	0.762	0	0	0	0	94	0	0	6
33,34	Γ_8^+	0.768	0	0	0	1	94	0	0	5
35	Γ_6^-	0.770	16	0	4	16	53	0	11	0
36,37	Γ_8^-	0.780	29	0	9	30	10	0	21	0
38	Γ_6^+	0.791	1	0	0	0	0	0	0	99
39,40	Γ_8^+	0.799	1	0	0	0	0	0	0	98
41	Γ_7^-	0.883	28	2	0	0	17	0	52	0
42	Γ_7^+	0.912	10	0	3	53	1	1	0	31
43,44	Γ_8^+	0.922	9	0	3	54	1	1	0	32

Table 4.III. The number of the valence electrons in the Ce APW sphere and the Rh APW sphere partitioned into angular momenta.

	s	p	d	f
Ce	0.23	5.98	1.22	1.21
Rh	0.47	0.36	7.14	0.04

located in such a region. Therefore, it is speculated that the Bloch states on the Fermi surface may contain considerable Ce *f* components.

The density of states is evaluated at E_F as $N(E_F)$ = 150.84 states/Ryd.cell. This value is substantially larger than the previous result, i.e. 129.0 states/Ryd.cell which was derived by neglecting the spin-orbit interaction (Yanase 1986). In this relativistic energy band structure, the spin-orbit interaction increases the total width of the *f* bands, and consequently tends to make the dispersion of the conduction bands near E_F rather flat. It also splits some degeneracies of the bands near E_F and weakens their dispersion. As the whole result, the density of states is increased by 17% at E_F.

In Fig. 4.2, the lowest twenty bands are fully occupied. The next three bands are partially occupied and form the Fermi surface. The number of the valence electrons in the APW sphere is partitioned into the angular momenta and listed in Table 4.III. Each Ce APW sphere contains about 1.2 electrons in the *f* state. We have obtained similar results for the number of electrons in the *f* state per Ce APW sphere in $CeSn_3$, CeNi and $CeRu_2Si_2$. We have also found that 0.1 ~ 0.2 electrons are contained in the *f* state within the La APW sphere in the corresponding La compounds, and these electrons do not have an atomic character but a plane-wave character. This means that just one 4*f* electron per Ce atom becomes itinerant in the ground state in $CeRh_2$ and other paramagnetic Ce compounds.

4.3.2 *The Fermi surface*

The three bands from the 21st band to the 23rd band construct the Fermi surface. Each of the lower two bands forms a nearly spherical hole sheet which is centered at the Γ point, as shown in Figs. 4.3 and 4.4. The hole sheet in the 22nd band is a little larger in size than that in the

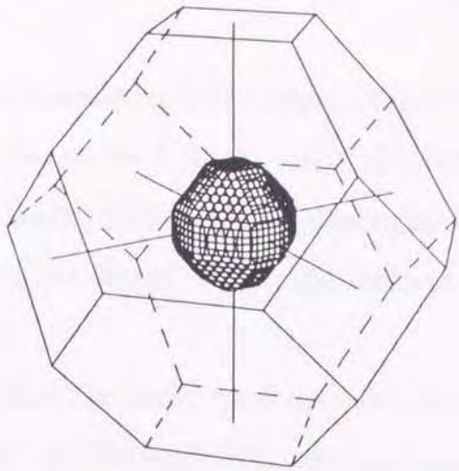

Figure 4.3. The hole sheet of the Fermi surface centered at the Γ point in the 21st band for $CeRh_2$.

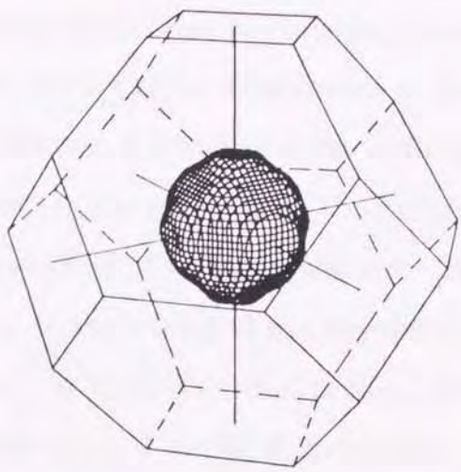

Figure 4.4. The hole sheet of the Fermi surface centered at the Γ point in the 22nd band for $CeRh_2$.

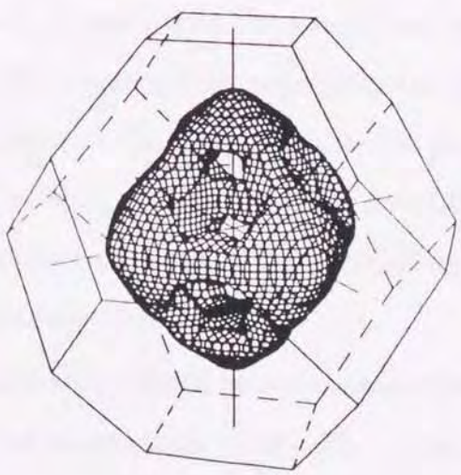

Figure 4.5. The electron sheet of the Fermi surface centered at the Γ point in the 23rd band for $CeRh_2$.

21st band. The 23rd band forms an electron sheet which is essentially a hollow sphere centered at the Γ point with eight windows open in the <111> direction, as shown in Fig. 4.5. It should be noted that all these Fermi surface sheets are closed within the Brillouin zone and no open orbit exists on them.

The hole sheet in the 21st band contains 0.06 holes/cell and that in the 22nd band contains 0.13 holes/cell. The electron sheets in the 23rd band contain the compensating number of electron carriers. $CeRh_2$ is a semimetal, because the number of the valence electrons per primitive cell is even. The parity of this number is even, irrespective of an itinerant or localized nature of the 4*f* electrons in the crystal, because the primitive cell contains two molecules in the Laves-phase structure.

In order to investigate the character of the Fermi surface, the charge distributions for some selected states on the three main sheets are partitioned according to the sites and the angular momenta and listed in Table 4.IV. It is found in Table 4.IV that in these Bloch states the Ce *f* components are dominant and the Rh *d* components are not equally large. This result implies that the hybridization between the Ce 4*f* state and the Rh 4*d* state is rather weak at the Fermi level, in qualitative agreement with the conclusion that Yanase (1986) previously reached. He investigated the electronic states, especially the partial densities of states, in the paramagnetic Ce compounds in the Laves-phase such as $CeRh_2$, $CeRu_2$ and $CeCo_2$, and found that the hybridization between the Ce 4*f* state and the transition metal d state in $CeRh_2$ is not so large as in $CeRu_2$ and $CeCo_2$ (Yanase 1986).

It is remarkable that these Bloch states contain also the Ce *d* components, which are comparable to the Rh *d* components. This result implies that the itinerant nature of the 4*f* electrons may be driven partly by the hybridization with the 5*d* states which belong to the adjacent Ce

Table 4.IV. Charge distributions partitioned into the APW spheres and the angular momenta for the Bloch states lying nearly on the hole sheet in the 21st band, the hole sheet in the 22nd band and the electron sheet in the 23rd band for $CeRh_2$. Components are given in percent. The Bloch state in the <111> direction in the 23rd band is listed for reference, though the electron sheet in the 23rd band has no state along the <111> direction.

<100> direction											
					Ce				Rh		
Band	Bloch state	k (a/2 π)	E_k (Ryd.)	out	s	p	d	f	s	p	d
21	Δ_6	(6,0,0)/20	0.7024	15	1	3	14	38	0	9	17
22	Δ_7	(7,0,0)/20	0.7018	12	0	2	9	37	1	9	27
23	Δ_6	(8,0,0)/20	0.7019	14	3	1	16	38	0	7	17
<110> direction											
					Ce				Rh		
Band	Bloch state	k (a/2 π)	E_k (Ryd.)	out	s	p	d	f	s	p	d
21	Σ_5	(4,4,0)/20	0.7037	13	1	2	14	52	0	8	6
22	Σ_5	(5,5,0)/20	0.6999	12	1	1	6	61	2	10	4
23	Σ_5	(8,8,0)/20	0.7014	7	0	0	4	65	0	3	18
<111> direction											
					Ce				Rh		
Band	Bloch state	k (a/2 π)	E_k (Ryd.)	out	s	p	d	f	s	p	d
21	$\Lambda_{4,5}$	(10,10,10)/60	0.7004	15	2	2	11	49	1	11	5
22	Λ_6	(9,9,9)/40	0.7005	11	0	1	12	63	0	5	4
23	$\Lambda_{4,5}$	(10,10,10)/40	0.7037	10	0	1	12	66	0	5	4

atoms. It is interesting to note that the nearest-neighboring Ce-Ce distance in $CeRh_2$ is smaller by 5% than that in the elemental α-Ce metal in the FCC crystal structure in which the 4*f* electrons are believed also to be itinerant.

It is recognized in Table 4.IV that the amount of the *f* components is the most on the 23rd band electron sheet and the least on the 21st band hole sheet. This tendency is natural, because the 23rd band is the closest to the narrow *f* bands and is influenced the most strongly by them.

For a better understanding of the Fermi surface, we explain the relationship between $CeRh_2$ and $LaRh_2$. In $LaRh_2$, the 20th band forms a small hollow hole sheet centered at the Γ point, the 21st band a small distorted hole sphere centered at the Γ point and the 22nd band a complex electron sheet which is multiply-connected from zone to zone. On the itinerant 4*f* electron model, $CeRh_2$ has two more Bloch electrons per primitive cell. Therefore, in $CeRh_2$ the *f* bands go down and the Fermi level rises up. As a result, we find in $CeRh_2$ that, though the 20th band hole disappears, the 21st band hole sphere survives, but becomes smaller and spherical. The 22nd band electron sheet grows so big that it can be described as a small hole. This is the second hole sheet we find in $CeRh_2$. In $CeRh_2$, a new electron sheet appears in the 23rd band to compensate the two hole sheets.

4.3.3 *Extremal cross-sections of the Fermi surface*

In order to investigate the validity of the Fermi surface, we calculate various extremal cross sections of the Fermi surface and compare them with the experimental results for the dHvA effect. The area of the extremal cross section of the Fermi surface, A, is related to the dHvA frequency, F, by the well-known formula $F = (ch/2\pi e) A$ (Shoenberg 1984

). For $CeRh_2$, it leads to the relation F (Oe) = $7.259 \times 10^7 A$, where A is measured in units of $(2\pi/a)^2$ (= 0.1941 a.u.).

Since they are nearly spherical, the hole sheets in the 21st band and the 22nd band possess the extremal cross section in all directions and their cross-sectional area depends on the direction only weakly. Each hole sheet produces a single dHvA frequency branch. In contrast, the electron sheet in the 23rd band possess several extremal cross sections in the limited range of directions which result in many piecemeal dHvA frequency branches. The existence of the eight small windows of the electron sheet makes the dHvA frequency spectrum rather complicated. The origins of various theoretical frequency branches are explained as follows.

a : an orbit running on the hole sheet centered at the Γ point in the 21st band, existing in the whole range of angles.

b : an orbit running on the hole sheet centered at the Γ point in the 22nd band, existing in the whole range of angles.

The following branches originate from the electron sheet in the 23rd band, and exist only in a limited range of angles because of the existence of the small windows. The electron sheet can be regarded as consisting of six caps which are fixed on the Δ axes and connected with each other by slender arms.

c : an inner orbit which has a center at the Γ point.

d : an outer orbit which has a center at the Γ point.

e : an orbit running outside on a cap around the point $(0.47,0,0)(2\pi/a)$ on the Δ axis.

f : an orbit running inside around the point $(0.18,0.18,0)(2\pi/a)$ on the Σ axis. The orbit looks like a hexagon.

g : an orbit running outside around the point $(0.17,0.17,0)(2\pi/a)$ on the Σ axis. The orbit looks like a hexagon, too.

h : an orbit running inside and outside on two adjacent caps through an arm around the point (0.30,0.30,0)($2\pi/a$) on the Σ axis. The orbit exists between 15° and 35° on the {110} plane.

i : an orbit running inside and outside on two adjacent caps through an arm around the point (0.32,0.32,0.06)($2\pi/a$). The orbit exists between 30° and 40° on the {110} plane.

j : an orbit running on the edge of the window around the point (0.24,0.24,0.24)($2\pi/a$) on the Λ axis. The orbit exists between 30° and 40° on the {110} plane.

k : an orbit running inside and outside on a cap through two windows around the point (0.5,0,0)($2\pi/a$) on the Δ axis. The orbit exists near the <110> direction.

l_1, l_2 : small orbits running inside and outside on a cap through two windows like the orbit ***k***. The center of the orbit is shifted from that of the orbit ***k***. It exist in the limited ranges of angles around the <111> direction.

m : an orbit running inside and outside through three arms around the point (0.36,0.13,0)($2\pi/a$). The orbit exists in the vicinity of 20° on the {100} plane.

In Fig. 4.6, these theoretical branches are drawn by solid curves. Besides these branches, other orbits exist around the slender arms of the electron sheet. The dHvA frequencies which these orbits produce are very small, and not plotted in Fig. 4.6.

4.3.4 *Cyclotron effective masses*

The cyclotron effective mass m_c^* for the extremal electron orbit is given by the derivative of the extremal cross-sectional area with respect to energy. For $CeRh_2$, the ratio of m_c^* to the free-electron mass m_0 is expressed as $m_c^*/m_0 = 0.06178 \times dA/dE$. The m_c^*/m_0 ratio is calculated

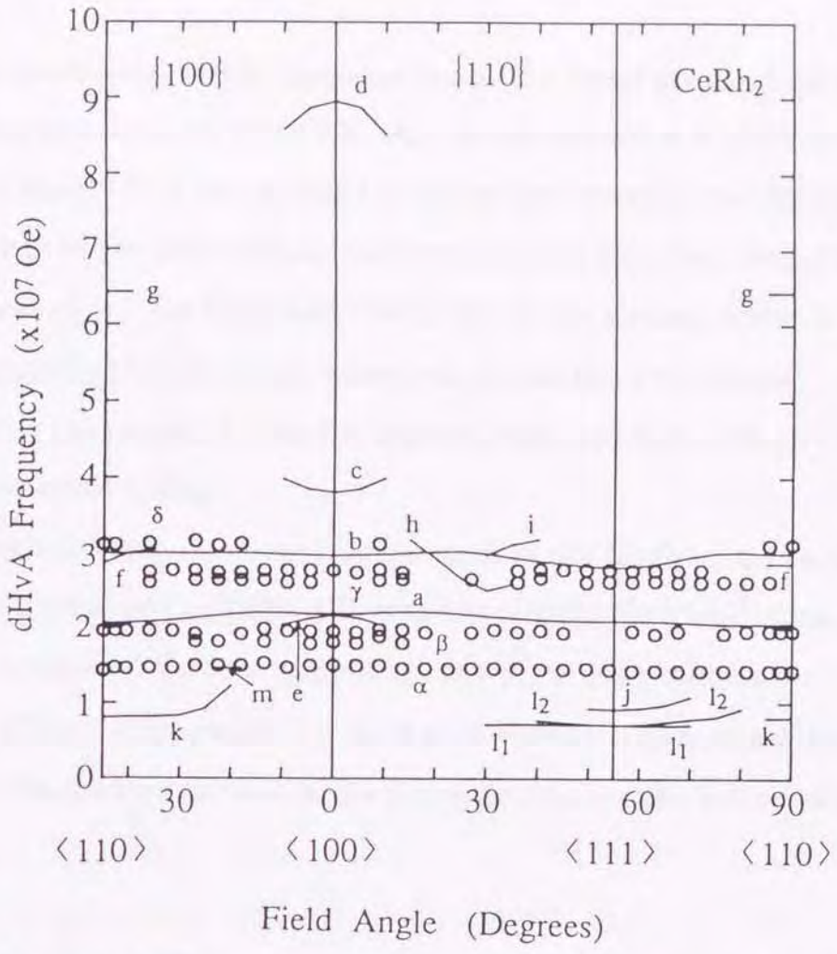

Figure 4.6. Theoretical and experimental frequencies of the de Haas-van Alphen effect for $CeRh_2$ as a function of the direction of magnetic field on the {100} and {110} planes. The solid curves and the alphabets show the theoretical results which are derived using the Fermi surfaces shown in Figs. 4.3, 4.4 and 4.5. Small circles and the Greek letters show the experimental results of Sugawara *et al.* (1994).

Table 4.V. Theoretical cyclotron effective mass ratio m_c^*/m_0, where m_0 is the free-electron mass, for the frequency branches of the de Haas-van Alphen effect in $CeRh_2$. ***B*** shows the direction of magnetic field.

Frequency branch	B	m_c^*/m_0
a	<100>	1.22
a	<110>	1.02
a	<111>	1.09
b	<100>	1.76
b	<110>	2.31
b	<111>	1.95
c	<100>	3.06
d	<100>	4.56
e	<100>	7.41
f	<110>	8.18
g	<110>	7.88
j	<111>	4.15
k	<110>	2.20
l_1,l_2	<111>	2.58

for each theoretical dHvA frequency branch in three principal symmetry directions and listed in Table 4.V. m_c^* for the branch ***a*** is quite isotropic and its magnitude is nearly equal to m_0 on the average. m_c^* for the branch ***b*** is larger than that for the branch a, but less than $3m_0$. The magnitude of m_c^* for the orbits which run on the electron sheet is much larger than that for the orbits which run on the two hole sheets. Especially, the branch ***d*** with the highest frequency has as large values for m_c^* as about $4.6m_0$.

Compare the amount of the *f* components in the Bloch states on the Fermi surface listed in Table 4.II with the magnitude of m_c^*, then it is readily recognized that the magnitude of m_c^* roughly reflects the amount of the *f* components, i.e. such part of the Fermi surface that contains the greater amount of the *f* components has the larger value of m_c^*.

4.4 *Comparison with Experiments*

The theoretical dHvA frequency branches are compared with the recent experimental results of Sugawara *et al.* (1994) in Fig. 4.6 where the experimental frequency branches are indicated by the Greek letters. We first notice that the theoretical branch ***a*** has the angle dependence which is similar to that of the experimental branch α, though the magnitude of ***a*** is slightly larger than that of α. The experimental m_c^*/m_0 ratio for the branch α is 1.80 and 1.70 in the <100> and the <110> direction, respectively (Sugawara *et al.* 1994). Thus, the magnitude of m_c^* for the branch α is greater than that of the branch ***a*** by 50% ~ 70%. Since the cyclotron effective mass is usually enhanced by many-body effects, the assignment (***a***,α) is reasonable.

The theoretical branch ***b*** has the angle dependence which is similar to that of the experimental branch β, though the magnitude of ***b*** is slightly

larger than that of β. The assignment (***b***,β) is not unreasonable. The experimental m_c^*/m_0 ratio for the branch β is 0.78 and 0.70 in the <100> and the <110> direction, respectively (Sugawara *et al.* 1994). Thus, the magnitude of m_c^* for the branch β is less than half of that for the branch ***b*** on the average.

The experimental branch γ is a set of several piecemeal branches which exist in the limited ranges of angles. Probable theoretical candidates for γ may be ***e***, ***f***, ***h*** and ***i*** because of similar magnitude. The magnitude of m_c^* for the branch γ is, however, also small, i.e. $0.84m_0$ in the <100> direction (Sugawara et al. 1994). The extremal cross-section corresponding to the branch δ which is observed in the vicinity of the <110> direction cannot be found on the theoretical Fermi surface. We will discuss an origin of this disagreement and speculate the origin of the branch δ in the next section.

The theoretical branches ***j***, ***k***, $\boldsymbol{l}_1$ and $\boldsymbol{l}_2$ which exist in the low-frequency region are not observed in the experiment. Because of the large cyclotron effective mass, the dHvA amplitude for those branches might be much weakened and they might be missed in the measurement. The theoretical branches ***c***, ***d*** and ***g*** are not observed either. Since they have the large cyclotron effective masses, they might be missed in the measurement, too.

The theoretical density of states at E_F, $N(E_F)$ = 150.84 states/Ryd.cell, corresponds to the electronic specific heat coefficient gband of 13.1 mJ/K^{2}mol. The experimental value is γ_{exp} = 20 mJ/K^{2}mol (Sugawara *et al.* 1994) and 22.5 mJ/K^{2}mol (Harrus *et al.* 1983). γ_{exp} may be enhanced by the many-body effects which cannot be taken into account by the exchange and correlation potential in the local-density approximation. The enhancement factor for γ due to such many-body effects is defined by $\lambda = \gamma_{exp} / \gamma_{band} - 1$ and estimated as λ = 0.53 or 0.72.

In the experiment by Sugawara *et al.* (1993), the γ value is obtained also for $LaRh_2$ as 3.7 mJ/K^2mol. This value is quantitatively well explained by the band structure calculation. It is remarkable that the γ value of $CeRh_2$ is 5 ~ 6 times as large as that of $LaRh_2$.

The enhancement factor λ we find in $CeRh_2$ is much smaller than those we have found in other paramagnetic Ce heavy-electron compounds. The magnitude of l is 2.0, 3.6 ~ 5.0 and 38.0 for $CeSn_3$, CeNi and $CeRu_2Si_2$, respectively.

4.5 *Discussions*

Though the theoretical frequency branches for the dHvA effect agree roughly with the experimental ones as a whole in the frequency region between 1×10^7Oe and 4×10^7Oe, there remain some apparent disagreements. Especially, a candidate frequency branch which corresponds to the highest observed branch ***d*** is not found the the theoretical Fermi surface. Here we discuss an origin of the disagreements.

4.5.1 *Sensitivity of the Fermi surface to a small change of E_F*

As is shown in Fig. 4.2, both the 21st band and the 22nd band have so large dispersion in the vicinity of E_F that the two hole sheets can keep their shape stable to small changes of the location of E_F, while the 23rd band has little dispersion along the Λ axis and it makes a precise determination of E_F rather difficult. In such an energy band structure, the electron sheet may not be so reliable as the two hole sheets and its shape may change sensitively to a small change in E_F, especially to a small raise of E_F.

Here we investigate how sensitively the Fermi surface and the dHvA frequency branches are modified to a small upward shift of the Fermi

level and if a more reasonable explanation of the experimental results can be achieved. We choose tentatively a hypothetical Fermi energy which is slightly higher (by 1.6 mRyd.) than the original Fermi energy. (The compensation of carriers is violated inevitably.) Then, we find that the two hole sheets in the 21st band and the 22nd band actually remain almost unchanged, so that the magnitude and the angular dependence of the branches ***a*** and ***b*** are little affected.

In contrast to the stability of the two hole sheets, the topology of the electron sheet in the 23rd band has changed drastically, and some parts of the dHvA frequency branches originating from this sheet are modified considerably. The eight windows are completely closed. The topology of the new electron sheet is a sphere which has a spherical empty space inside around the Γ point and is connected from zone to zone with slender arms stretching in the <111> direction through the L point.

As a result, all orbits that pass through the windows disappear. An inner orbit is separated and closed inside. Thus, the branch c can now exist in the whole range of angles. It depends weakly on direction, changing from 3.5×10^7 Oe in the <100> direction to 4.0×10^7 Oe in the <110> direction. The branch ***d*** which originates from an outer orbit can exist in a wider range of angles both in the {100} and {110} planes. An outer orbit produces a new branch with about 9×10^7 Oe around the <111> direction, which is designated as ***x***. However, ***d*** and ***x*** cannot be continuous because of the existence of the slender arms.

The experiment by Sugawara *et al.* (1993) suggests the existence of three or more spherical sheets of the Fermi surface, and thus seems to support the validity of the topology of the new electron sheet. It might be possible to assign the experimental branch ***d*** to a part of the theoretical branch c. The large branches ***d*** and ***x*** may not be observed in the measurements of Sugawara *et al.* (1993) because of the limitation of

purity of the sample. To draw a decisive conclusion, however, refined investigations are absolutely necessary.

4.5.2 *Experimental inconsistency of m_c^* with γ*

The γ_{exp} value of $CeRh_2$ is fairly large (Sugawara *et al.* 1993), i.e. about six times that of $LaRh_2$ (Sugawara *et al.* 1994). In contrast, the cyclotron masses that Sugawara *et al.* (1993) measured for a few dHvA frequency branches in $CeRh_2$ are not equivalently large on the average. They note this apparent inconsistency between the experimental results for m_c^* and γ_{exp}, and are afraid to fail to detect the dHvA frequencies having cyclotron effective masses which would be large enough to be consistent with γ_{exp} (Sugawara *et al.* 1994).

We suggest that probable candidates for missing dHvA frequency branches in $CeRh_2$ may be the branche ***d*** which originates from the outer orbits on the electron sheet. It is quite stable to uncertainties of the band structure calculation, but has large values for m_c^* which may diminish the amplitude of the dHvA effect considerably.

4.5.3 *Contrasts between $CeRh_2$ and $LaRh_2$*

There are marked contrasts between $CeRh_2$ and $LaRh_2$. As is explained in 4.3.2, the 21st band forms a distorted hole sphere in $LaRh_2$ and a spherical hole sheet in $CeRh_2$, and the former is larger in size than the latter. The 21st band hole sphere is the most stable to uncertainties of the band calculation. The hole sheet in $LaRh_2$ produces the dHvA frequency branch which depends on the direction of a magnetic field weakly, while the hole sheet in $CeRh_2$ produces the branch ***a*** which is almost independent of it. These theoretical branches explain qualitatively well the behavior of the experimental branches

which are indicated as α in both compounds. The magnitude of the frequencies observed in $LaRh_2$ is actually larger than that in $CeRh_2$.

The experimental cyclotron effective mass ratio for the branch α is 1.70 ~ 1.80 in $CeRh_2$ (Sugawara *et al.* 1994) and 1.03 ~ 1.21 in $LaRh_2$ (Sugawara *et al.* 1993), while the corresponding theoretical value is 1.02 ~ 1.22 and 0.89 ~ 1.06, respectively. Both in theory and experiment, the effective mass is heavier in $CeRh_2$ than in $LaRh_2$, and this tendency is understood as a natural consequence of the effect of the *f* bands. In $CeRh_2$, it may further involve the enhancement factor due to many-body interactions between 4*f* electrons which the local-density approximation fails to take into account.

4.5.4 *Anomalous cyclotron effective masses of the branch β and the branch γ*

In spite of the reasonable explanation for the branch α, mysterious results are found in the experiments for $CeRh_2$ by Sugawara *et al.* (1994). The cyclotron mass ratio m_c^*/m_0 measured for the branch β is 0.78 and 0.70 in the <100> and <110> direction, respectively (Sugawara *et al.* 1994). The angle dependence of this branch suggests that it may be assigned reasonably well to the theoretical branch ***b*** which originates from the 22nd band hole sheet. This hole sheet is stable also like the 21st band hole sheet. The theoretical cyclotron mass ratio is, however, greater than the double of the experimental value. It is not understandable why the experimental m_c^*/m_0 ratio for the branch β is so small. The small m_c^*/m_0 ratio for the branch γ is mysterious also.

It has been found in $CeSn_3$, CeNi and $CeRu_2Si_2$ that the m_c^*/m_0 ratio is greater than that observed in the corresponding La compounds because of the effect of the *f* bands and the many-body enhancement factor. The m_c^*/m_0 ratio for the branch β in $CeRh_2$, however, seems

smaller than that expected for $LaRh_2$, because in the latter compound the 22nd band forms a multiply-connected electron sheet which has the frequency branch with the m_c^*/m_0 ratio of about 1.0 in the <111> direction (Higuchi and hasegawa). Actually, the m_c^*/m_0 ratios found for the branch β and the branch γ in $CeRh_2$ are the smallest m_c^*/m_0 ratio that has been measured for the dHvA frequency branches with magnitude larger than 1×10^7Oe in the paramagnetic heavy-electron Ce compounds.

4.6 *Summary*

On the basis of the itinerant-electron model for the 4*f* electrons, it is predicted that the Fermi surface of $CeRh_2$ consists of two spherical hole sheets and a hollow electron sphere. These spherical sheets of the Fermi surface explain qualitatively well the observed behavior of the dHvA frequency branches, all of which are almost independent of the direction of a magnetic field. The theoretical frequency branch *d* originating from an outer orbit on the electron sheet probably have not been observed in the measurement of Sugawara *et al.* (1994).

The large cyclotron effective masses observed for the branch α are roughly consistent with the enhancement factor which is estimated from the difference between γ_{exp} and γ_{band}. It is not understandable, however, why the cyclotron effective masses observed for the branch β and the branch γ are smaller than those predicted by this band structure calculation.

In order to find a solution to the problem on the cyclotron effective masses, it is necessary to re-examine the dHvA effect in $CeRh_2$ using samples of improved purity. A measurement of the high-field magnetoresistance is desirable to test the validity of the predicted topology of the electron sheet of the Fermi surface. We hope that

theoretical results reported in this paper will be helpful to such a future experimental study. As we have recently studied on $CeSn_3$ (Hasegawa *et al.* 1990), a clear-cut conclusion on the itinerant nature of the 4*f* electrons can be drawn only if all the major dHvA frequency branches are observed and whole the Fermi surface is clarified.

5. A Band Picture for the 4*f* Electrons in $YbGa_2$

5.1 *Introduction*

In this chapter, we will apply the RLAPW method to a self-consistent calculation of the energy band structure, in particular the Fermi surface, for the rare-earth compound $YbGa_2$ by assuming that the 4*f* electrons are itinerant. $YbGa_2$ is one of the reference materials for the ferromagnetic compound $CeGa_2$ where the 4*f* electrons are believed to be localized at the Ce ions (Umehara *et al.* 1991). Another reference material is $LaGa_2$, for which the dHvA effect has been measured (Sakamoto *et al.* 1994), and the Fermi surface has been investigated by band theory (Harima and Yanase 1991). The 4*f* bands are unoccupied in $LaGa_2$, and are expected to be almost fully occupied in $YbGa_2$. In contrast to the simple-hexagonal AlB_2 crystal structure of $CeGa_2$ and $LaGa_2$ with one molecule per primitive cell, $YbGa_2$ has the double-hexagonal $CaIn_2$ crystal structure with two molecules per primitive cell.

The magnetic susceptibility of $YbGa_2$ show almost no temperature dependence below 500K (Klaasse *et al.* 1977). This experimental result implies that $YbGa_2$ may have no magnetic moment, i.e. Yb ions may be divalent. Yamazaki *et al.* (1994) and Sugawara *et al.* (1995) have recently succeeded in growing up the single crystals of this compound, and observing several frequency branches of the dHvA effect which are less than 3×10^7 Oe together with the cyclotron effective mass which varies from $0.20m_0$ to $0.88m_0$, where m_0 is the free-electron mass. These small cyclotron effective masses suggest that in $YbGa_2$ the 4*f* electrons may neither contribute directly to the formation of the Fermi surface nor affect the Bloch states on the Fermi surface strongly.

As a result of a self-consistent calculation by the RLAPW method, it has been found that the 4*f* electrons form very narrow bands just below

the Fermi level, which are split into two subbands by the spin-orbit interaction, and that $YbGa_2$ is a semimetal having small hole and electron sheets of the Fermi surface. These small sheets of the Fermi surface can explain the angle dependence of the experimental dHvA frequencies reasonably well, and the origins of all of the observed frequency branches are identified without ambiguity.

$YbGa_2$ has the double hexagonal $CaIn_2$ crystal structure which is derived from the simple hexagonal AlB_2 crystal structure by displacing the B atoms slightly and alternately in the *c* direction, and shown in Fig. 5.1 together with the primitive vectors ($\boldsymbol{a}_1$, $\boldsymbol{a}_2$, $\boldsymbol{a}_3$). It has the non-symmorphic space group $P6_3/mmc$ and contains two molecules per primitive cell. The lattice constants, the position of atoms in the primitive cell and other constants used in the calculation are listed in Table 5.I. The Brillouin zone of the hexagonal lattice is shown in Fig. 5.2 together with the primitive vectors of the reciprocal lattice, ($\boldsymbol{b}_1$, $\boldsymbol{b}_2$, $\boldsymbol{b}_3$).

5.2 *Method of calculation*

The radii of the APW spheres are chosen to be as large as possible unless they overlap each other. Under this condition, the Ga APW sphere radius is given by the half of the nearest-neighbor Ga–Ga distance, i.e.

$$R(\mathrm{Ga}) = \frac{1}{2}\sqrt{\frac{a^2}{3} + 4z^2c^2},$$

and the Yb APW sphere radius is given by

$$R(\mathrm{Yb}) = \sqrt{\frac{a^2}{3} + \left(\frac{1}{4} - z^2\right)c^2} - R(\mathrm{Ga}),$$

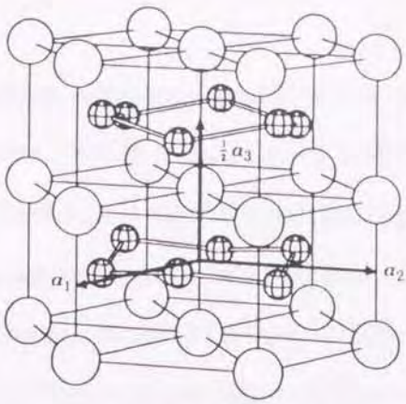

Figure 5.1. Crystal structure of $YbGa_2$ in the double hexagonal lattice. Spheres with and without patterns show the position of the Ga atoms and the Yb atoms, respectively. The origin of coordinates is set at the center of the next nearest-neighbor Yb–Yb line. $\boldsymbol{a}_1$, $\boldsymbol{a}_2$ and $\boldsymbol{a}_3$ are three primitive vectors.

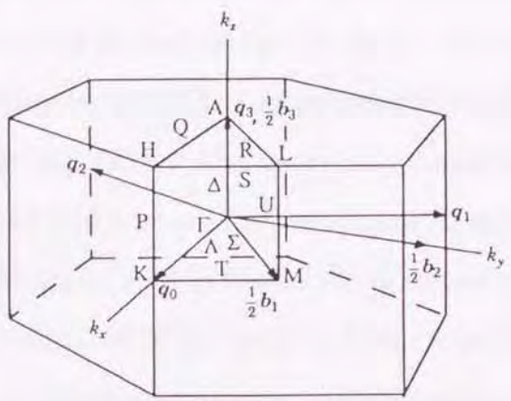

Figure 5.2. The Brillouin zone for the hexagonal lattice together with the primitive vectors of the reciprocal lattice, $\boldsymbol{b}_1$, $\boldsymbol{b}_2$ and $\boldsymbol{b}_3$. The four vectors $\boldsymbol{q}_0$, $\boldsymbol{q}_1$, $\boldsymbol{q}_2$, $\boldsymbol{q}_3$, which are conventionally used in the hexagonal system, are also added to the figure. The symmetry labels are taken from Cracknell *et al.* (1979).

Table 5.I. Crystal constants of $YbGa_2$ used in the calculation. The lattice constants and atomic positions are taken from Villars and Calvert (1986). Atomic positions are measured in units of the primitive vectors ($\boldsymbol{a}_1$, $\boldsymbol{a}_2$, $\boldsymbol{a}_3$), which are shown in Fig. 5.2.

Crystal structure		$CaIn_2$-type
Space group		$P6_3/mmc$
Lattice constant,	a	8.420623 a.u.
	c	13.581467 a.u.
	c/a	1.612882
Atom positions	Yb	(0, 0, ± 1/4)
	Ga	± (1/3, 2/3, z)
		± (2/3, 1/3, 1/2 + z)
		z = 0.044
APW sphere radius	R(Yb)	3.098789 a.u. = 0.368000 a
	R(Ga)	4.033696 a.u. = 0.479026 a

where a and c are the lattice constants and z is the peculiar parameter of the $CaIn_2$ crystal structure, which are listed in Table 5.I. The Yb APW spheres, the Ga APW spheres and the interstitial region occupy 30%, 31% and 39% of the whole space in the crystal, respectively.

The starting crystal charge density for the self-consistent iteration processes is constructed by the superposition of the relativistic charge densities calculated for the neutral atoms Yb (Xe, $4f^{14}6s^2$) and Ga (Ar, $3d^{10}4s^24p^1$) by using the relativistic method of Liberman et al. (1965), where Xe and Ar mean the atomic configuration of xenon and argon, respectively. We take into account the exchange-correlation potential within the density-functional formalism in the LDA. The functional form of the exchange-correlation potential is the parameterization by Gunnarsson and Lundqvist (1976). The same functional form is used in the calculations for atoms and a crystal. The spin-orbit splittings in the $5p$, $5d$, $4f$ states in the Yb atom, and in the $3d$, $4p$ states in the Ga atom are 453mRyd., 9mRyd., 97mRyd., 34mRyd. and 7mRyd., respectively. During the iterations, the frozen-core approximation is adopted, i.e. the atomic charge densities of the Xe core except the $5p^6$ states for Yb and the Ar core for Ga are assumed to be unchanged as the core electrons in the crystal.

During each self-consistent iteration cycle for the crystal, a new charge density is constructed by using fourteen sampling points of $\boldsymbol{k}$ which are distributed uniformly in the irreducible 1/24 parts of the Brillouin zone. At each $\boldsymbol{k}$, about 580 RLAPW basis functions are adopted under the condition $k_\mu \leqq 3.15\ (2\pi/a)$, and the total angular momenta up to 17/2 are taken into account. These conditions correspond to 290 plane waves and the angular momenta up to $l_{max} = 8$, which give the eigenvalues well converged within a few mRyd. The convergence criterion is $4\pi r^2 |\ \rho_p(r)_{in} - \rho_p(r)_{out}\ | < 0.001$ (p = Yb and Ga).

At the starting charge density, the Yb 4*f* state forms very flat bands which are split into two subbands by the spin-orbit interaction. The position of these *f* bands relative to the valence band bottom is so high that the Fermi level lies in the middle of the upper subband, and the number of the valence electrons in the *f* state contained in the Yb APW sphere amounts to 9.1 only. As self-consistent iterations proceed, the *f* bands descend gradually, and the electron number in the *f* state increases. In an early stage of the self-consistent iterations, the values for $\left(\varepsilon_{3,1}^{\mathrm{Yb}},\ \varepsilon_{3,2}^{\mathrm{Yb}}\right)$ and $\left(\varepsilon_{-4,1}^{\mathrm{Yb}},\ \varepsilon_{-4,2}^{\mathrm{Yb}}\right)$ must be lowered in accord with the descent of the *f* bands, and the magnitude of ω in eq. (3.43) must be kept close to 1, i.e. $\omega = 0.97 \sim 0.99$, to prevent divergence. As iterations proceed further, the value of ω can be made smaller to hasten convergence. Finally, the *f* bands settle below the Fermi level, as is shown in Fig. 5.3, and the electron number in the *f* state contained in the Yb APW sphere increases up to 13.4, as is shown in the next section. The sets of the energy values for $\left(\varepsilon_{\kappa,1}^{p},\ \varepsilon_{\kappa,2}^{p}\right)$ used in the final stage are listed in Table 5.II. It should be noted that the convergence of the self-consistent calculation cannot be made faster for $YbGa_2$ than for $CeRh_2$, because in $YbGa_2$ the electron number in the *f* state contained in the rare-earth APW sphere must change largely, i.e. by about 4, while in $CeRh_2$ it must by only about 1 (Higuchi *et al.* 1994a).

For the final self-consistent charge density, the eigenvalues are calculated at 259 points including many general $\boldsymbol{k}$ points in the irreducible 1/24 parts of the Brillouin zone.

5.3 *Results of calculation*

5.3.1 *Fully relativistic energy band structure*

Figure 5.3 shows the fully relativistic energy band structure calculated for $YbGa_2$ along the principal symmetry axes in the Brillouin zone.

Table 5.II. The sets of the energy values $\left(\varepsilon_{l1}^{p},\ \varepsilon_{l2}^{p}\right)$ and $\left(\varepsilon_{-l-1,1}^{p},\ \varepsilon_{-l-1,2}^{p}\right)$ used in the calculation.

Atom	Energy (Ryd.)	l				
		0	1	2	3	4 ~ 8
Yb	ε_{l1}	–	–1.50	–0.10	0.25	0.00
	ε_{l2}	–	–0.50	0.80	0.50	0.80
	$\varepsilon_{-l-1,1}$	0.00	–1.50	–0.10	0.25	0.00
	$\varepsilon_{-l-1,2}$	0.80	–0.50	0.80	0.50	0.80
Ga	ε_{l1}	–	0.00	–1.00	0.00	0.00
	ε_{l2}	–	0.80	–0.20	0.80	0.80
	$\varepsilon_{-l-1,1}$	0.00	0.00	–1.00	0.00	0.00
	$\varepsilon_{-l-1,2}$	0.80	0.80	–0.20	0.80	0.80

Twelve 5*p* bands which lie in the energy range between –1.6 Ryd. and –1.1 Ryd. and forty 3*d* bands which lie in the energy range between –0.6 Ryd. and –0.5 Ryd. are omitted from Fig. 5.3. The Fermi energy E_F is located at 0.412861 Ryd. and indicated by a dashed line. Along the R axis including the A and L points, the energy bands are degenerate fourfold because of the non-symmorphic space group $P6_3/mmc$. Along the Q and S axes, each of the energy bands splits into two doubly-degenerate bands by the spin-orbit interaction, although all the energy bands are degenerate fourfold on the hexagonal symmetry plane including the Q, R and S axes if the spin-orbit interaction is neglected.

In order to investigate the character of each band, the charge distributions are calculated for many states at the Γ point and listed in Table 5.III. The lowest band consists dominantly of the Ga *s* state. The bands which have appreciably the Ga *p* state lie in the wide range from 0 Ryd. to 0.7 Ryd. As is seen from Fig. 5.3, fourteen flat bands lie just below E_F, which consist dominantly of the Yb *f* states and therefore are identified as the *f* bands. The *f* bands splits into two subbands which correspond to the total angular momenta $j = 5/2$ (lower bands) and $j = 7/2$ (upper bands). The magnitude of the splitting is about 0.1 Ryd., which is comparable with the spin-orbit splitting of the 4*f* state in the Yb atom. In the vicinity of their bottom, the *f* bands hybridize with the Ga *p* bands and have small dispersion. Near the Fermi level, the *f* bands hybridize strongly with the Ga *p* and the Yb *d* bands in the vicinity of the Γ point, so that fair amounts of the *f* states are distributed nearby E_F.

The number of the valence electrons contained in the APW spheres is partitioned into the angular momenta and listed in Table 5.IV. Each Yb APW sphere contains about 13.4 electrons in the *f* state. This means that 1.2 holes per primitive cell exist in the 4*f* bands, and that the Bloch states

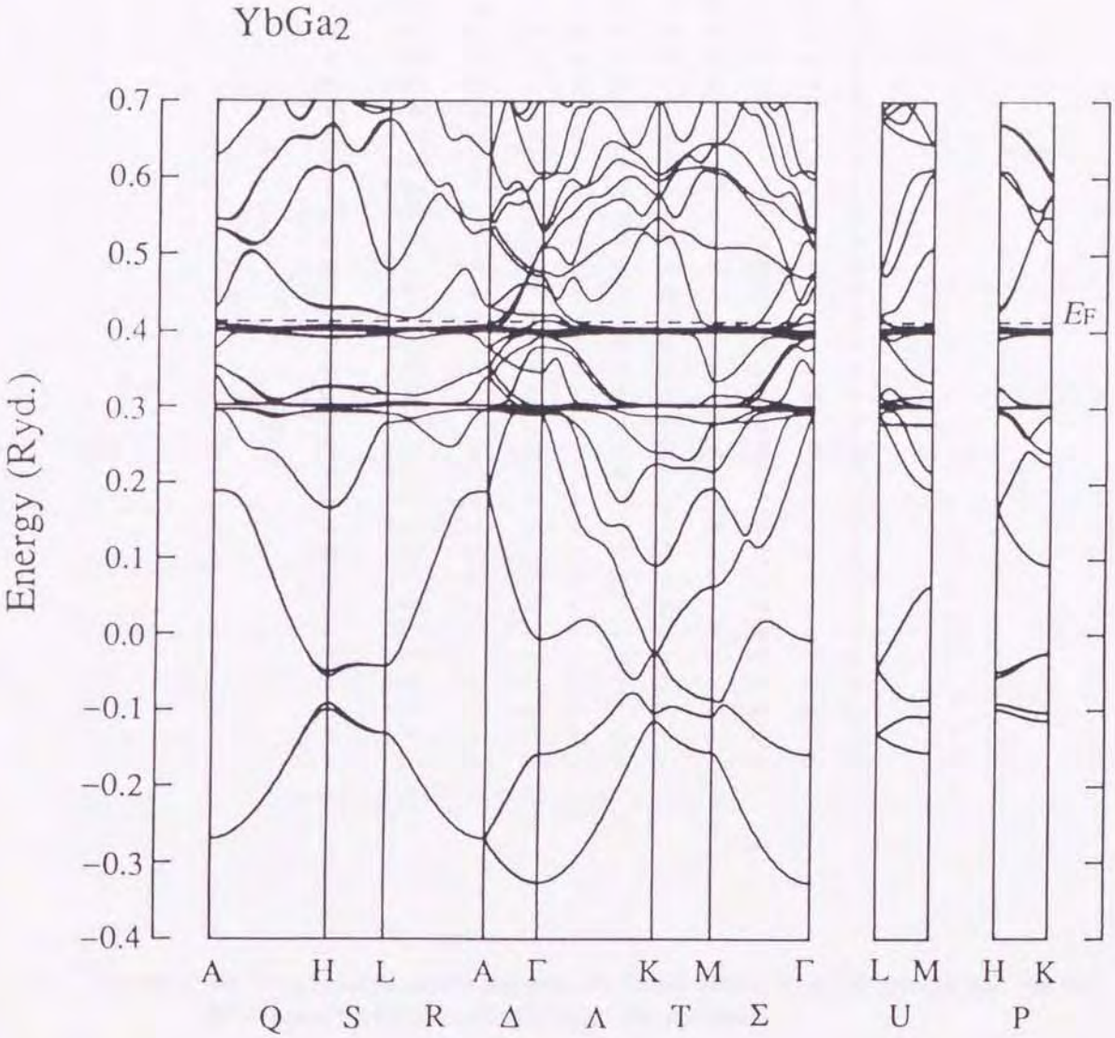

Figure 5.3. Energy band structure calculated for $YbGa_2$ with the self-consistent RLAPW method. E_F shows the Fermi energy.

Table 5.III. Charge distributions partitioned into the angular momenta for the Bloch states at the Γ point. Components are shown in percent. Each band is doubly degenerate.

Band	Energy (Ryd.)	Outer region	Yb spheres				Ga spheres			
			s	*p*	*d*	*f*	*s*	*p*	*d*	*f*
1	−0.327	34	13	0	0	0	53	0	0	0
2	−0.158	26	0	7	0	1	63	1	2	0
3	−0.007	41	17	0	4	0	15	22	0	0
4	0.290	9	0	0	0	78	11	1	1	0
5	0.292	34	0	0	24	0	0	39	1	0
6	0.294	34	0	0	26	0	0	38	1	0
7	0.297	2	0	0	0	96	0	2	0	0
8	0.299	1	0	0	0	97	0	1	0	0
9	0.300	1	0	0	0	98	0	0	0	0
10	0.302	0	0	0	0	99	0	0	0	0
11	0.303	0	0	0	0	99	0	0	0	0
12	0.347	19	1	0	0	44	32	2	2	0
13	0.380	8	0	0	2	77	0	12	0	0
14	0.394	8	0	0	7	78	0	5	1	0
15	0.395	2	0	0	0	92	4	1	0	0
16	0.398	2	0	0	0	95	0	3	0	0
17	0.399	1	0	0	0	98	0	0	0	0
18	0.402	0	0	0	0	99	0	0	0	0
19	0.403	0	0	0	0	99	0	0	0	0
20	0.415	27	1	0	40	25	0	5	2	0
21	0.422	5	0	0	0	80	13	1	0	0
22	0.460	9	0	1	0	6	82	0	0	1
23	0.472	27	0	0	51	0	0	16	5	0
24	0.478	28	0	0	51	0	0	16	5	0
25	0.508	22	0	0	1	23	0	51	2	0
26	0.512	26	0	0	1	14	0	56	2	0
27	0.529	31	0	1	52	0	0	10	5	0
28	0.534	31	0	2	47	1	0	13	5	0
29	0.599	39	3	0	7	9	0	40	0	1
30	0.608	38	0	5	1	6	0	45	2	1
31	0.702	43	0	14	9	3	0	23	7	0

Table 5.IV. The number of the valence electrons in the Yb APW sphere and the Ga APW sphere partitioned into angular momenta.

	s	*p*	*d*	*f*
Yb	0.33	6.24	0.79	13.41
Ga	1.04	0.98	9.94	0.01

on the Fermi surface may have considerable *f* components. The density of states is calculated at E_F as $N(E_F)$ = 39.12 states/Ryd.cell.

5.3.2 *The Fermi surface*

The Fermi surface is constructed by four bands from the 20th band to the 23rd band. The 20th, 21st and 22nd bands form hole sheets which are centered at the Γ point, as is shown in Figs. 5.4, 5.5 and 5.6, respectively. The hole sheet in the 20th band is a very small ellipsoid shrinked in the *c* direction. The hole sheets in the 21st and 22nd bands look like ellipsoids stretched in the *c* direction. The hole sheet in the 21st band is smaller in size than that in the 22nd band. The 23rd band constructs three electron sheets, each of which looks like a distorted square cushion centered at the M point, as is shown in Fig. 5.7. All of the hole sheets and the electron sheets are closed, so that they cannot hold any open orbits.

The hole sheets in the 20th, 21st and 22nd bands contain 0.0015, 0.0457 and 0.1351 holes/cell, respectively. The electron sheets in the 23rd band contain totally the compensating number of electrons. This semimetallic nature is consistent with the fact that $YbGa_2$ is a compensated metal because it has even number of electrons in the primitive cell.

In order to investigate the character of the Fermi surface, the charge distributions for some selected states whose energies are close to E_F are partitioned according to the sites and the angular momenta and listed in Table 5.V. It is found in Table 5.V that the Fermi surface sheets in the 21st, 22nd and 23rd bands consist dominantly of the Yb *f* component, and that the hole sheet in the 20th band consists dominantly of the Yb *d* and Yb *f* components. At the Fermi level, the 21st, 22nd and 23rd bands contain some amounts of the Yb *d* and the Ga *p* components which are not so large as the Yb *f* component, and the 20th band contains the Yb *d* component nearly equal to the Yb *f* component. Thus, all sheets of the Fermi surface

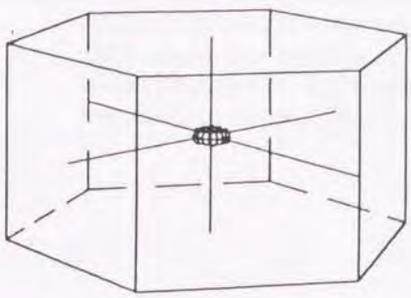

Figure 5.4. The hole sheet of the Fermi surface centered at the Γ point in the 20th band for $YbGa_2$.

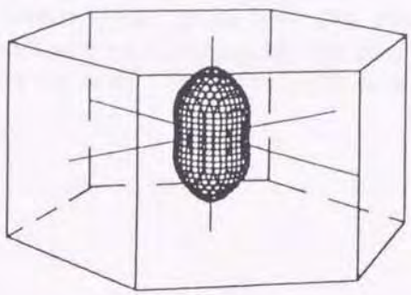

Figure 5.5. The hole sheet of the Fermi surface centered at the Γ point in the 21st band for $YbGa_2$.

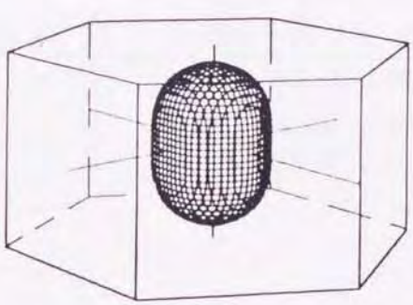

Figure 5.6. The hole sheet of the Fermi surface centered at the Γ point in the 22nd band for $YbGa_2$.

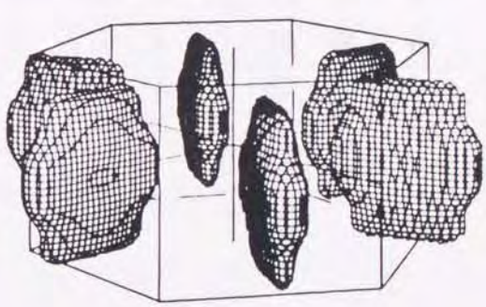

Figure 5.7. The electron sheet of the Fermi surface centered at the M point in the 23rd band for $YbGa_2$.

Table 5.V. Charge distributions partitioned according to the sites and the angular momenta for the selected states whose energy is close to E_F. In the 20th, 21st and 22nd bands, the states on the Δ axis, Λ axis and Σ axis are listed, and in the 23rd band the states on the T axis, Σ axis and U axis are listed. The wave vector $\boldsymbol{k}$ is measured in units of ($\boldsymbol{b}_1$, $\boldsymbol{b}_2$, $\boldsymbol{b}_3$).

Band	Symmetry axis	$\boldsymbol{k}$	$E_{\boldsymbol{k}}$	Out	Yb				Ga		
					s	*p*	*d*	*f*	*s*	*p*	*d*
20	Δ	(0, 0, 4) / 96	0.4135	24	0	0	36	31	1	5	2
	Λ	(6, −3, 0) / 96	0.4131	24	1	0	35	31	0	5	2
	Σ	(6, −6, 0) / 96	0.4125	23	1	0	34	34	0	5	2
21	Δ	(0, 0, 34) / 96	0.4138	12	0	0	11	63	0	12	1
	Λ	(12, −6, 0) / 96	0.4114	5	0	0	5	81	4	3	0
	Σ	(10, −10, 0) / 96	0.4122	5	0	0	6	79	5	4	0
22	Δ	(0, 0, 42) / 96	0.4129	6	0	0	6	79	0	6	1
	Λ	(18, −9, 0) / 96	0.4130	9	0	0	10	71	0	8	1
	Σ	(16, −16 0) / 96	0.4115	7	0	0	9	75	0	6	1
23	T	(51, −45, 0) / 96	0.4122	7	1	1	3	82	0	6	0
	U	(48, −48, 42) / 96	0.4134	18	2	2	9	60	1	6	2
	Σ	(28, −28, 0) / 96	0.4120	13	2	1	10	69	0	3	1

contain considerable amounts of the *f* component through the *p-f* and/or the *d-f* hybridizations, though most of the 4*f* bands lie below E_F.

5.3.3 *Extremal cross-sections of the Fermi surface*

We calculate the extremal cross-sections of the Fermi surface in various directions in order to compare with the experimental results for the dHvA effect. The area of the extremal cross-section of the Fermi surface, A, is related to the dHvA frequency F by the formula $F = c\hbar A/2\pi e$ (Shoenberg 1984). For $YbGa_2$, it gives the relation F [Oe] = $2.0823 \times 10^8 A$, where A is measured in units of $(2\pi/a)^2$.

The hole sheets in the 20th, 21st and 22nd bands are ellipsoids centered at the Γ point, so that in all directions there exist the extremal cross-sections whose center is located at the Γ point. Therefore, each hole sheet produces a single dHvA frequency branch. The three inequivalent electron sheets in the 23rd band produce the three dHvA frequency branches which exist in the whole range of angles and may be degenerate in some directions.

In order to specify the directions of the orbits, we define the four vectors ($\boldsymbol{q}_0$, $\boldsymbol{q}_1$, $\boldsymbol{q}_2$, $\boldsymbol{q}_3$), as is shown in Fig. 5.2. The lattice planes of the reciprocal lattice are denoted with the Miller indices in terms of these vectors. The origins of various theoretical dHvA frequency branches are explained as follows :

b : an orbit running on the hole sheet centered at the Γ point in the 22nd band with the maximum cross-sectional area, existing in the whole range of angles. Its cross-sectional area takes the largest value in the [1010] direction and the smallest value in the [0001] direction.

c : an orbit running on the hole sheet centered at the Γ point in the 21st band with the maximum cross-sectional area, existing in the whole range of angles. The angle dependence of its cross-sectional area shows

the behavior similar to that of the orbit $\boldsymbol{b}$, because the shape of the hole sheet in the 21st band resembles that in the 22nd band.

$\boldsymbol{d}$: an orbit running on the hole sheet centered at the Γ point in the 20th band with the maximum cross-sectional area, existing in the whole range of angles. The angle dependence of its cross-sectional area shows the opposite behavior to that of the orbit $\boldsymbol{c}$.

The following branches originate from the electron sheets in the 23rd band. In order to clarify the origins and degeneracies of the branches, we call three inequivalent electron sheets ' E-1 ', ' E-2 ' and ' E-3 '. The centers of these electron sheets are located at (1/2, −1/2, 0), (1/2, 0, 0) and (0, 1/2, 0), respectively, which are measured in units of the primitive vectors of the reciprocal lattice, ($\boldsymbol{b}_1$, $\boldsymbol{b}_2$, $\boldsymbol{b}_3$), shown in Fig.5.2.

$\boldsymbol{a}_1$: orbits running on the E-1 with the maximum cross-sectional area. The orbit $\boldsymbol{a}_1$ exists in the whole range of angles.

$\boldsymbol{a}_2$: orbits running on the E-2 with the maximum cross-sectional area existing in the whole range of angles. In the [1120] direction, it takes the largest cross-sectional area that the electron sheets have. It is degenerate with the branch $\boldsymbol{a}_1$ in the [0001] direction.

$\boldsymbol{a}_3$: orbits running on the E-3 with the maximum cross-sectional area existing in the whole range of angles. It is degenerate with the branch $\boldsymbol{a}_2$ on the {1210} plane, and with the branch $\boldsymbol{a}_1$ on the {1100} plane.

Thus, the upper branch on the {1210} plane and the lower branch on the {1100} plane have double degeneracy, and three inequivalent branches become degenerate triply in the [0001] direction.

Figure 5.8 show all these theoretical dHvA frequencies as functions of the magnetic-field direction by solid curves.

5.3.4 *Cyclotron effective masses*

The ratio of the cyclotron effective mass m_c^* to m_0 is given by the formula $m_c^*/m_0 = \left(\hbar^2/2\pi m_0\right) dA/dE$. For $YbGa_2$ it is expressed as $m_c^*/m_0 = 0.17722 \times dA/dE$, where A is the cross-sectional area and measured in units of $(2\pi/a)^2$. The ratio is calculated for each theoretical dHvA frequency branch in the three high-symmetry directions such as [0001], [1010] and [1120] directions, and listed in Table 5.VI. It changes with the field direction, and varies from 0.5 to 2.3. This property roughly reflects the shapes of the anisotropic Fermi surface sheets; the branch ***d*** which originates from the ellipsoid shrinked in the *c* direction takes a large value for m_c^*/m_0 in the *c* direction, both of the two branches ***b*** and ***c*** which originate from the ellipsoids stretched in the *c* direction take large values in the direction normal to the *c* direction, and the branches $\boldsymbol{a}_1$, $\boldsymbol{a}_2$, $\boldsymbol{a}_3$ originating from the distorted cushion sheets take the largest value in the [1120] direction.

5.4 *Comparison with experiments*

In this section, we compare the theoretical results for the dHvA frequency branches and the cyclotron effective masses with the experimental ones.

5.4.1 *The dHvA frequency branches*

In Fig. 5.8, we compare the theoretical dHvA frequency branches with the recent experimental results by Yamazaki *et al.* (1994). The experimental frequency branches are denoted by the Greek letters. As is seen in this figure, the theoretical dHvA frequency branches agree well with the experimental ones as a whole, though the theoretical sheets of the Fermi surface in the 21st, 22nd, 23rd bands are a little too large in size, and the hole sheet in the 20th band is far small. In the following, we try to assign each experimental branch to the theoretical branch.

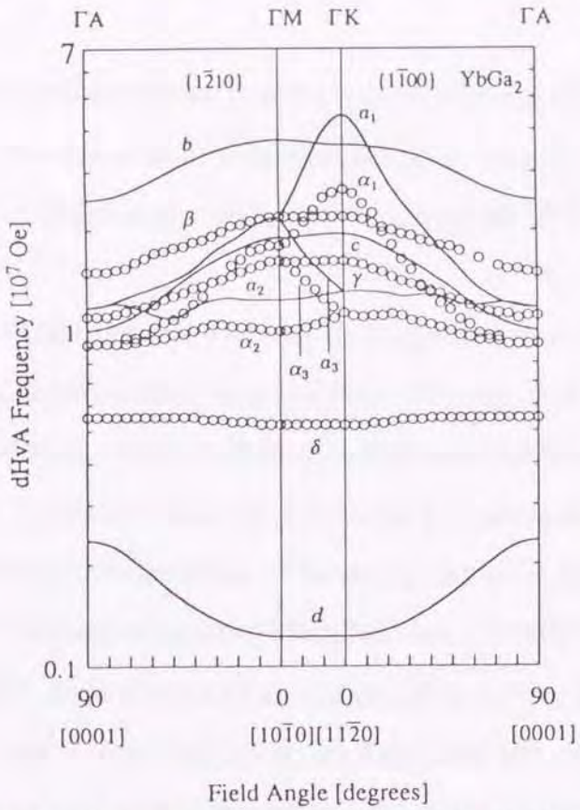

Figure 5.8. Theoretical and experimental frequencies of the de Haas-van Alphen effect for $YbGa_2$ as a function of the direction of the magnetic field on the {1210} and {1100} planes. The solid curves and the alphabets show the theoretical results calculated from the Fermi surface shown in the Figs. 5.4, 5.5, 5.6 and 5.7. Small circles and the Greek letters show the experimental results of Yamazaki *et al.* (1994).

Table 5.VI. Theoretical and experimental cyclotron effective mass ratio, m_c^* / m_0, where m_0 is the free-electron mass, for the dHvA frequency branches which originate from the 20th, 21st and 22nd band hole sheets and 23rd band electron sheets of the Fermi surface in $YbGa_2$. The Greek letters show the experimental branches, and $\hat{B}$ shows the magnetic-field direction. Experimental branches in parentheses show the assignment to theoretical branches. The sign of equality means that the branches coincide in magnitude in the indicated direction of the magnetic field. Experimental results are those of Yamazaki *et al.* (1994).

Branch	Band	$\hat{B}$	m_c^*/m_0 Theor.	Exper.
d (δ)	20	[0001]	1.42	0.20
d (δ)	20	[10$\bar{1}$0]	0.82	0.25
d (δ)	20	[11$\bar{2}$0]	0.81	0.24
c (γ)	21	[0001]	0.50	0.43
c (γ)	21	[10$\bar{1}$0]	0.99	0.47
c (γ)	21	[11$\bar{2}$0]	1.03	0.48
b (β)	22	[0001]	0.82	0.69
b (β)	22	[10$\bar{1}$0]	1.68	0.80
b (β)	22	[11$\bar{2}$0]	1.82	0.77
$\alpha_1=\alpha_2=\alpha_3$ ($\alpha_1=\alpha_2=\alpha_3$)	23	[0001]	1.02	0.32
α_2 (α_2)	23	[10$\bar{1}$0]	0.92	0.34
$\alpha_1=\alpha_3$ ($\alpha_1=\alpha_3$)	23	[10$\bar{1}$0]	1.73	0.58
$\alpha_2=\alpha_3$ ($\alpha_2=\alpha_3$)	23	[11$\bar{2}$0]	1.18	0.35
α_1 (α_1)	23	[11$\bar{2}$0]	2.34	0.88

The experimental branches β and γ have the same behavior in the angle dependence as the theoretical branches $\boldsymbol{b}$ and $\boldsymbol{c}$, respectively. Judging from the order of their magnitude, the assignments ($\boldsymbol{b}$,β) and ($\boldsymbol{c}$,γ) may be reasonable.

The experimental branch δ seems to originate from a spherically small sheet. A probable theoretical candidate for this small sheet may be the hole sheet in the 20th band, so that the experimental branch δ may be assigned to the theoretical branch $\boldsymbol{d}$, though a quantitatively large discrepancy exists between them. The assignment ($\boldsymbol{d}$,δ) is also supported by the fact that the experimental branch δ has a shallow minimum around the [1010] direction and the branch $\boldsymbol{d}$ has a similar tendency.

The experimental branches α_1, α_2 and α_3 have the angle dependence which is similar to that of the theoretical branches $\boldsymbol{a}_1$, $\boldsymbol{a}_2$ and $\boldsymbol{a}_3$, though the magnitude of the theoretical branches is larger than that of the experimental ones. The angle dependence of the theoretical branch $\boldsymbol{a}_2$ is a little different from that of the experimental branch α_2 in the vicinity of 60° both on the {1210} and {1100} planes, because the theoretical electron sheet is deformed from a simple square cushion. The experimental branches suggest that the electron sheet in reality may be like a simple square cushion, and may not be deformed so largely.

5.4.2 *Cyclotron effective masses*

In Table 5.VI, we compare the theoretical values for m_c^*/m_0 with the experimental ones (Yamazaki *et al.* 1994) in the three high-symmetry directions such as [0001], [1010] and [1120] directions.

In the experimental branch δ, the ratio m_c^*/m_0 varies only weakly with the field direction like the dHvA frequency. In the corresponding theoretical branch $\boldsymbol{d}$, however, it is very anisotropic. The theoretical value

is larger than the experimental value by the factor of 3.3 in the [1010] and [1120] directions and 7.1 in the [0001] direction.

In the experimental branches β and γ, m_c^*/m_0 is also isotropic, whereas it is very anisotropic in the corresponding theoretical branches ***b*** and ***c***. In both branches, the theoretical value for m_c^*/m_0 agrees roughly with the experimental one in the [0001] direction, but is greater than twice the experimental one in the [1010] and [1120] directions.

In contrast to the qualitative disagreement of m_c^*/m_0 between the theoretical hole sheets and the experimental ones, the angle dependence of m_c^*/m_0 in the theoretical branches $\boldsymbol{a}_1$, $\boldsymbol{a}_2$, $\boldsymbol{a}_3$ is very similar to that of the experimental branches α_1, α_2, α_3. Quantitatively, the theoretical value is larger by the factor of about 3 than the experimental one in all directions.

Although we can explain the origins of all experimental dHvA frequency branches as is shown in the previous section, the agreement between theory and experiment in the cyclotron effective mass is not so good. All of the experimental cyclotron effective mass are larger than the theoretical ones. We will discuss the cause for this disagreement in the next section.

The theoretical density of states at E_F, $N(E_F)$ = 39.12 states/Ryd.cell, corresponds to the electronic specific heat constant γ_{band} of 3.39 mJ/K^{2}mol. The experimental value γ_{exp} may be enhanced by the many-body effects which cannot be taken into account by the exchange-correlation potential in the local-density approximation, but it is not available now.

5.5 *Discussions*

The RLAPW method has been applied to a self-consistent calculation of the electronic structure for $YbGa_2$ on the basis of an itinerant 4*f* electron model. The calculation has been carried out also within the framework of the MTA and the LDA. Since for a given potential the

RLAPW method has proven to be able to yield very accurate results, the disagreement between theory and experiment will tell us about limitations of other aspects in the calculation.

In the calculated band structure, the *f* bands lie just below the Fermi level, and affect the Bloch states in the vicinity of the Fermi level. The Fermi surface is formed by four bands, and the Bloch states on each sheet of the Fermi surface consist of the *f* states together with the Yb *d* states and the Ga *p* states. Except the hole sheet in the 20th band, the two hole sheets in the 21st and 22nd bands and the electron sheets in the 23rd band can explain the magnitude and the angle dependence of the experimental dHvA frequency branches reasonably well. The origins of all of the observed frequency branches are identified without ambiguity. The quantitative disagreement between theory and experiment is comparable to that found for the low-frequency branches in $LaRu_2Si_2$ (Yamagami and Hasegawa 1992) and $CeRu_2Si_2$ (Yamagami and Hasegawa 1993). We consider it should be ascribed to limitations of the LDA and/or the MTA.

Yamazaki *et al.* (1994) have measured the cyclotron effective mass for $YbGa_2$, and found that for all frequency branches its magnitude is less than the free-electron mass. From the paramagnetic susceptibility and the light cyclotron effective mass, they are led to conclude that in $YbGa_2$ the 4*f* electrons may be localized at the Yb ions and behave like the core electrons. Table 5.VI shows that for each of the frequency branches, magnitude of the theoretical cyclotron effective mass is larger than that of the experimental one. This quantitative disagreement between theory and experiment suggests that in this calculation the effect of the 4*f* bands on the Bloch states in the vicinity of the Fermi level may be too strong. However, this result does not necessarily imply that an energy band picture may not hold for the 4*f* electrons in $YbGa_2$,

because the energy dispersion in the four bands which form the Fermi surface might become large, and the cyclotron effective masses might decrease, if the 4*f* bands were located more deeply, as is easily recognized from Fig.5.3. We consider the error in the position of the 4*f* bands should be ascribed to limitations inherent in the exchange-correlation potential in the LDA. Through previous band structure calculations in the LDA, we have already noticed that in many La compounds the 4*f* bands appear just above the Fermi level and affect the Bloch states on the Fermi surface too strongly (Onuki and Hasegawa 1994). In order to understand more clearly the nature of limitations inherent in the LDA as used in the calculation for the 4*f* bands, the dHvA effect experiments on many other Yb compounds are desirable.

At present the RLAPW method is limited to a calculation for the paramagnetic state. This method is also applicable to the magnetic states. As a next study, we plan to extend the RLAPW method so that the energy band structure of the magnetic *f*-electron compounds can be calculated. The dHvA effect has been already measured in the ferromagnetic compound UGe_2 (Satoh *et al.* 1992) and the antiferromagnetic ternary compound UPd_2Al_2 (Inada et al.), and it is suggested that in these magnetic U compounds the 5*f* electrons may be itinerant and responsible for magnetism. The RLAPW method is expected to verify such interesting nature of the 5*f* electrons, which has not been found for the 4f electrons in any Ce compounds.

6. Curveture factors for the electron and the hole sheets of the Fermi surface of LaAg

6.1. *Introduction*

Since a structural phase transition was discovered in $LaAg_xIn_{1-x}$ for $x < 0.95$ (Ihring *et al.* 1973, Balster *et al.* 1975), the electronic structure of LaAg has been the subject of many theoretical and experimental investigations to clarify the origins of the anomalous elastic behavior and the structural phase transition. In this chapter, we investigate the electronic structure, especially the Fermi surface, for LaAg by band theory.

The structural change was ascribed to a lifting of the twofold degeneracy of the La-d(Γ_{12}) band due to a tetragonal lattice distortion, i.e. the band Jahn-Teller effect (Ihring *et al.* 1973, Balster *et al.* 1975). To confirm the idea of the band Jahn-Teller effect, the energy band structure was calculated for LaAg in a non-self-consistent manner by using a non-relativistic APW and relativistic KKR method (Hasegawa *et al.* 1975), and also self-consistently by using a non-relativistic APW method (Tannous *et al.* 1976). These previous calculations employed the Slater exchange potential, and results for the position of the La d(Γ_{12}) band relative to the Fermi energy E_F were conflicting.

A refined calculation of the energy band structure for LaAg was carried out self-consistently by a non-relativistic ASW method within the framework of the density-functional theory in the local-density approximation (LDA) (Niksch *et al.* 1982). Later on, the band calculation for LaAg was refined further by taking into account relativistic effects (Niksch *et al.* 1987), though the spin-orbit interaction was treated by a perturbation theory. These new calculations concluded that the La d(Γ_{12}) band lies above E_F, and predicted that the Fermi surface consists of large hole and electron sheets as well as small hole

and electron pockets. The magnetoacoustic de Haas-van Alphen (dHvA) effect was measured, and several frequency branches with relatively low frequencies in the range from 5.2×10^6 Oe to 2.1×10^7 Oe were observed (Niksch *et al.* 1987). The experimental results were found to be explained reasonably well by the small hole and electron pockets (Niksch *et al.* 1987). On the basis of the small electron pockets, a mechanism which is different from the band Jahn-Teller effect was proposed for the deformation potential coupling in LaAg (Niksch *et al.* 1987).

The dHvA effect has recently been measured for the magnetic succeptibility in LaAg successfully, and the frequency branches with high frequencies of the order 10^8 Oe which seem to originate from the large hole and electron sheets have been observed (Motoki *et al.* 1995). In this chapter, we carry out a self-consistent calculation for LaAg by using a fully-relativistic APW method, and reconstruct the Fermi surface. Our result confirms well the prediction by Niksch *et al.* (1987), though the smallest electron pocket that they suggested to exist disappears in our result. As a result of careful investigation of the angle dependence of the extremal cross-sectional areas on the large hole and electron sheets, the origins of the experimental dHvA frequency branches in the high-frequency region are identified, and thus the electronic structure, especially the Fermi surface, of LaAg has been revealed much.

6.2. *Method of calculation*

LaAg crystallizes in the CsCl crystal structure. The lattice constants, the position of atoms in the primitive cell and other constants used in the calculation are listed in Table 6.I. A self-consistent calculation is carried out at the experimental lattice constant a (= 3.814 Å) (Villars

and Calvert 1986). The radii of the La and Ag APW spheres are chosen to be equal, i.e. $R(\mathrm{La}) = R(\mathrm{Ag}) = \sqrt{3}\,a\,/\,4$. Thus, the La APW spheres, the Ag APW spheres and the interstitial region occupy 34%, 34% and 32% of the whole space in a crystal, respectively.

The starting crystal charge density for the self-consistent iteration process is constructed by a superposition of the relativistic charge densities for the neutral atoms La (Xe, $4f^0 5d^1 6s^2$) and Ag (Kr, $4d^{10} 5s^1$), where Xe and Kr imply the atomic configurations of xenon and krypton, respectively, which are generated by the self-consistent relativistic calculations for atoms (Liberman *et al.* 1965). In the atomic calculation, the same exchange-correlation potential is used as in the crystal. During the iterations, the frozen-core approximation is adopted, i.e. the atomic charge densities of the Xe core except the $5p^6$ states for La and the Kr core for Ag are assumed to represent the core electrons in the crystal. In the relativistic atomic calculations, the spin-orbit splitting in the La 4f, La 5d and Ag 4d state is found to be 21 mRyd., 14 mRyd. and 41 mRyd., respectively.

In each cycle of the self-consistent iteration processes, a new crystal charge density is constructed using 35 $\boldsymbol{k}$ points which are distributed uniformly over the irreducible 1/48 parts of the simple cubic Brillouin zone. At each k in the Brillouin zone, about 280 plane waves are adopted under the condition $| \boldsymbol{k} + \boldsymbol{G} | < 4.1\ (2\pi/a)$, where $\boldsymbol{G}$ is a reciprocal lattice vector, and angular momenta up to $l_{\max} = 8$ are taken into account. They give the eigenvalues which converge well within a few mRyd. The convergence criterion for iterations is $| rV_{\mathrm{in}}(r) - rV_{\mathrm{out}}(r) | < 0.001$, where $V_{\mathrm{in}}(r)$ and $V_{\mathrm{out}}(r)$ mean the input potential and the output potential, respectively, and about 100 iterations are demanded. The sets of the energy values for $\left(\varepsilon_{\kappa,1}^{\mathrm{La}},\ \varepsilon_{\kappa,2}^{\mathrm{Ag}}\right)$, which are chosen appropriately within a

Table 6.I. Crystal constants of LaAg used in the calculation. The lattice constants and atomic positions are taken from Villars and Calvert (1986).

Crystal structure		CsCl-type
Space group		Pm3m
Lattice constant, a		7.207418 a.u.
Atom positions	La	(0, 0, 0)
	Ag	(1/2, 1/2, 1/2)
APW sphere radius	R(La)	3.120812 a.u. = 0.433000 a
	R(Ag)	3.120812 a.u. = 0.433000 a

Table 6.II. The sets of the energy values $\left(\varepsilon_{l1}^{p},\ \varepsilon_{l2}^{p}\right)$ and $\left(\varepsilon_{-l-1,1}^{p},\ \varepsilon_{-l-1,2}^{p}\right)$ used in the calculation.

Atom	Energy	l				
	(Ryd.)	0	1	2	3	4 ~ 8
La	ε_{l1}	–	–1.20	–0.06	0.31	0.00
	ε_{l2}	–	–0.50	0.80	0.60	0.80
	$\varepsilon_{-l-1,1}$	0.00	–1.20	–0.06	0.31	0.00
	$\varepsilon_{-l-1,2}$	0.80	–0.50	0.80	0.60	0.80
Ag	ε_{l1}	–	0.00	–0.14	0.00	0.00
	ε_{l2}	–	0.80	0.31	0.80	0.80
	$\varepsilon_{-l-1,1}$	0.00	0.00	–0.14	0.00	0.00
	$\varepsilon_{-l-1,2}$	0.80	0.80	0.31	0.80	0.80

limited range of energy in the RLAPW method and used in the final stage, are listed in Table 6.II.

Using the final self-consistent charge density, the eigenvalues are calculated at many symmetry and general points, totally at 286 points in the irreducible 1/48 parts of the Brillouin zone.

6.3. *Results of the band calculation*

6.3.1 *Fully relativistic energy band structure*

Figure 6.1 shows the fully-relativistic energy band structure calculated for LaAg. When the band structure is compared with the result of Niksch *et al.* (1987), it looks very similar to each other, though the two calculations treat relativistic effects in different ways. Niksch *et al.* (1987) included the spin-orbit interaction by a perturbation theory at the end of the self-consistent calculation, while we have taken into account it from the start of the self-consistent calculation. For LaAg, it seems that the fully-relativistic calculation does not give a band structure which is very different from the perturbation theory. There is, however, a small difference between the two calculations, i.e. in our result the whole nineth band is unoccupied, and consequently the extremely small Fermi surface sheet that Niksch *et al.* (1987) predicted to exist at the R point disappears. The total density of states is calculated at the Fermi energy E_F as $N(E_F)$ = 22.3 states /Ryd.cell.

The seventh and the eighth bands are partially occupied, and construct the Fermi surface. The lower band forms a large hole sheet centered at the Γ point and three inequivalent small hole sheets centered at the M points in the simple cubic Brillouin zone. The upper band forms a large electron sheet centered at the R point and three inequivalent small electron sheets centered at the X points.

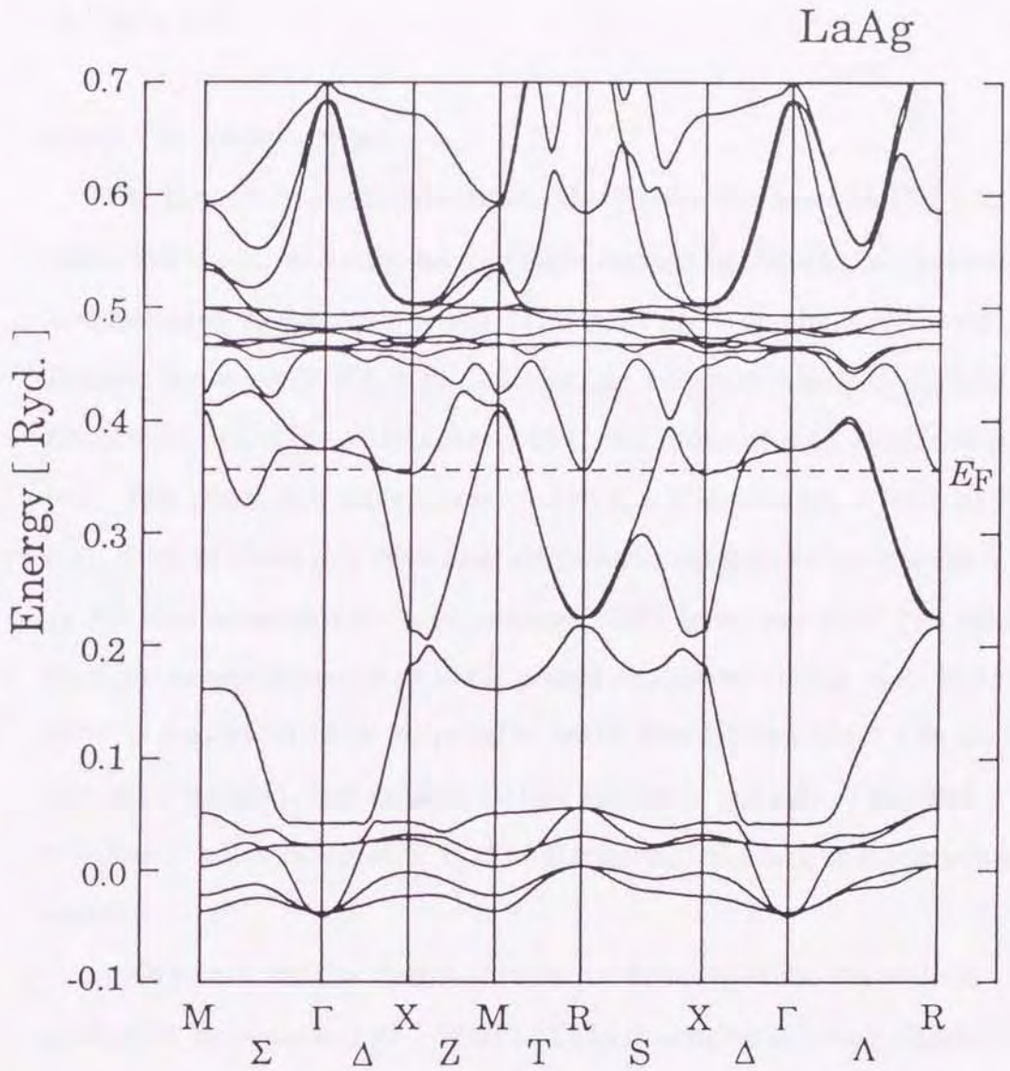

Fig. 6.1. Energy band structure calculated for LaAg with a self-consistent relativistic APW method. E_F shows the Fermi energy.

The charge distributions are calculated for many states at the Γ point and listed in Table 6.III. The number of the valence electrons contained in the APW spheres is partitioned into the angular momenta and listed in Table 6.IV.

6.3.2 *The Fermi surface*

The large hole sheet centered at the Γ point is shown in Fig. 6.2. It looks like a rounded cube having eight bumps in the <111> directions, and contains 0.39 holes per cell. The large electron sheet centered at the R point is shown in Fig. 6.3. It looks like a sphere which is slightly distorted toward the <110> directions, and contains 0.43 electrons per cell. The small hole sheets centered at the M points are shown in Fig. 6.4. Each of them is a deformed ellipsoid of revolution having the T axis as the axis of revolution, and contains 0.021 holes per cell. The small electron sheets centered at the X points are shown in Fig. 6.5. Each of them is an almost ideal ellipsoid of revolution having the Δ axis as the axis of revolution, and contains 0.007 electrons per cell. The total number of holes is equal to that of electrons, i.e. LaAg is a compensated metal.

This result for the Fermi surface confirms well the theoretical prediction by Niksch *et al.* (1987). They concentrated their efforts to the investigation of the properties of the small hole and electron sheets, and only sketched the large hole and electron sheets. The shape of the large hole and electron sheets illustrated in Figs. 3a and 3b in their paper (Niksch *et al.* 1987) looks similar to our result shown in Figs. 6.2 and 6.3 in this chapter. In the following sections, we investigate the extremal cross section, the cyclotron effective mass and the local curvature of the large hole and electron sheets in detail.

Table 6.III. Charge distributions partitioned into the angular momenta for the Bloch states at the Γ point . Components are shown in percent. Each band is doubly degenerate.

Band	Energy (Ryd.)	Outer region	La spheres				Ag spheres			
			s	*p*	*d*	*f*	*s*	*p*	*d*	*f*
1	−0.042	34	17	0	0	0	49	0	0	0
2	−0.038	8	0	0	4	0	0	0	87	0
3	−0.038	8	0	0	4	0	0	0	87	0
4	0.023	2	0	0	2	0	0	0	96	0
5	0.023	2	0	0	2	0	0	0	96	0
6	0.042	1	0	0	2	0	0	0	96	0
7	0.375	26	0	0	57	0	0	0	16	0
8	0.375	26	0	0	57	0	0	0	16	0
9	0.463	3	0	0	0	94	0	2	0	0
10	0.463	3	0	0	0	94	0	2	0	0
11	0.466	3	0	0	0	96	0	0	0	1
12	0.478	4	0	1	0	90	0	5	0	0
13	0.482	3	0	0	0	94	0	1	0	1
14	0.482	3	0	0	0	94	0	1	0	1
15	0.494	1	0	0	0	98	0	0	0	1
16	0.684	8	0	0	85	0	0	0	5	0
17	0.684	8	0	0	85	0	0	0	5	0
18	0.699	8	0	0	85	0	0	0	5	0

Table 6.IV. The number of the valence electrons in the La APW sphere and the Ag APW sphere partitioned into angular momenta.

	s	*p*	*d*	*f*
La	0.21	5.86	0.89	0.14
Ag	0.97	0.63	9.53	0.02

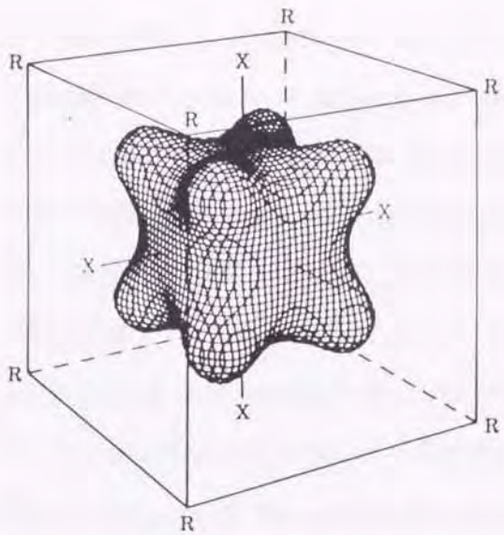

Fig. 6.2. Large hole sheet of the Fermi surface in the seventh band for LaAg. The cubic frame shows the Brillouin zone, the center of which is set at the the Γ point.

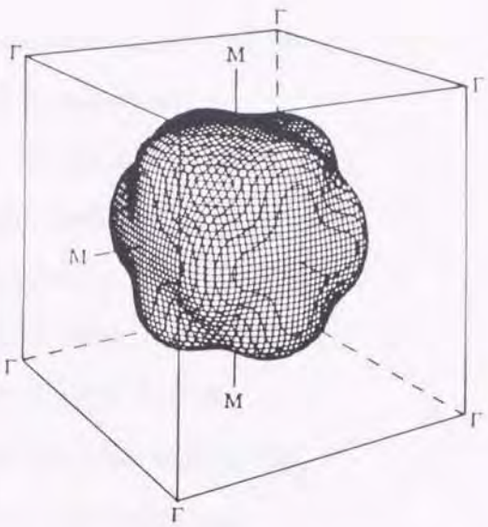

Fig. 6.3. Large electron sheet of the Fermi surface in the eighth band for LaAg. The cubic frame shows the Brillouin zone, the center of which is set at the R point.

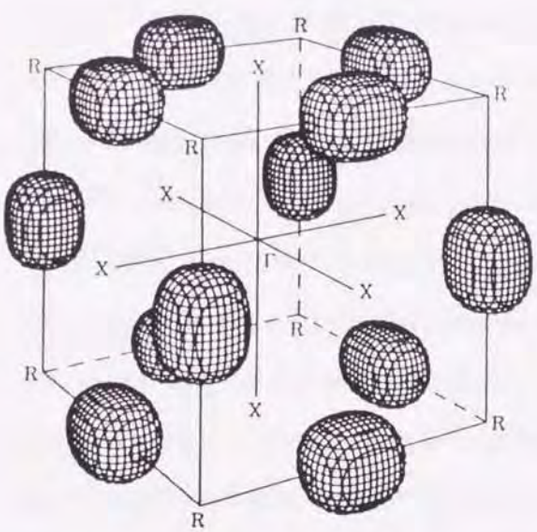

Fig. 6.4. Small hole sheets of the Fermi surface in the seventh band for LaAg centered at the M points. The cubic frame shows the Brillouin zone, the center of which is set at the the Γ point.

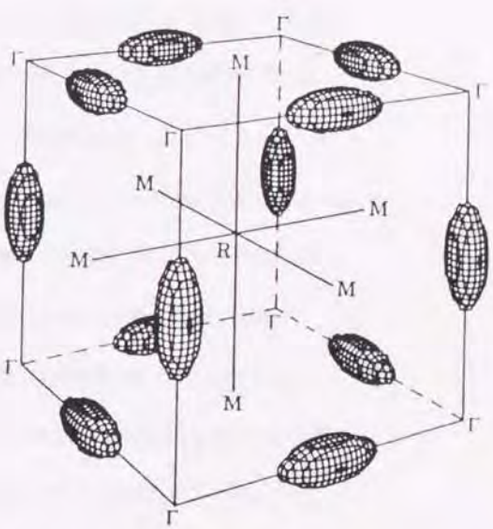

Fig. 6.5. Small electron sheets of the Fermi surface in the eighth band for LaAg centered at the X points. The cubic frame shows the Brillouin zone,the center of which is set at the R point.

6.4. *Comparison with experiments*

In order to investigate the validity of the Fermi surface derived, we calculate its various extremal cross sections and compare our theoretical results with the experimental results for the dHvA effect. The area of the extremal cross section of the Fermi surface, A, is related to the dHvA frequency, F, by the well-known formula $F = (ch/2\pi e)\,A$ (Shoenberg 1984). For LaAg, it leads to the relation F [Oe] = 2.84237×10^8 A, where A is measured in units of $(2\pi/a)^2$ (= 0.75998 a.u.). The cyclotron effective mass m_c^* for the extremal electron orbit is given by the derivative of the extremal cross-sectional area with respect to energy. For LaAg, the ratio of m_c^* to the free-electron mass m_0 is expressed as $m_c^*/m_0 = 0.2419 \times dA/dE$.

Since it is nearly spherical, the large electron sheet possesses the maximum cross section in all directions. The maximum cross section has a center at the R point, and its area depends on the direction only weakly. It produces a single dHvA frequency branch which is denoted as α. The frequency of this branch is very large, and ranges from 1.21×10^8 Oe to 1.35×10^8 Oe. As a function of the magnetic-field direction, it has a broad peak which is centered in the <111> direction

The large hole sheet also possesses the maximum cross section in all directions. Its center is not located always at the Γ point, but moves as the magnetic-field direction changes. The dHvA frequency branch corresponding to the maximum cross section is denoted as β. In the <100> direction, the branch β originates from the orbit which passes on four bulges and has a center at the Δ axis. In the <110> and <111> direction, it originates from the orbit which passes on four bulges and has a center at the Γ point, and from the orbit which passes on three bulges and has a center at the Λ axis, respectively. Owing to its peculiar shape, the minimum cross section exists on the large hole sheet in

limited ranges of angle around the <100> and <111> directions. The dHvA frequency branch corresponding to the minimum cross section is denoted as *c*. At the boundaries of the limited ranges of angle, the branch *c* connects with the branch *b* smoothly. The frequency of these two branches ranges from 8.46×10^7 Oe to 1.28×10^8 Oe.

The three inequivalent small electron sheets produce altogether three different frequencies in each direction of a magnetic field, which may coincide with each other in the high-symmetry directions. The frequency branches which they produce are denoted as d_1, d_2 and d_3. The frequency of these branches ranges from 3.53×10^6 Oe to 9.48×10^6 Oe. The frequency branches which the three inequivalent small hole sheets produce are denoted as g_1, g_2 and g_3. The frequency of these branches ranges from 1.46×10^7 Oe to 1.97×10^7 Oe.

In Fig. 6.6, all these theoretical dHvA frequency branches are shown as a function of the direction of a magnetic field on the {100} and {110} plane, and compared with the experimental dHvA frequencies which have recently been measured by Motoki *et al.* (1995). In Fig. 6.6, the experimental frequency branches are indicated by the Greek letters. The m_c^*/m_0 ratio is calculated for each theoretical dHvA frequency branch in the three high-symmetry directions and listed in Table 6.V.

In Fig. 6.6, we first notice that the theoretical branch *a* has the frequency and the angle dependence which are quite similar to those of the experimental branch α, though the frequency of the branch *a* is slightly larger than that of the branch α in all directions. The theoretical frequencies are larger than the experimental ones by 6 ~ 8%. Table 6.V shows that the ratio m_c^*/m_0 is rather isotropic both in the branches α and *a*, and that the ratio m_c^*/m_0 for the branch α is greater than that of the branch *a* by 42% ~ 68%. Since the cyclotron effective

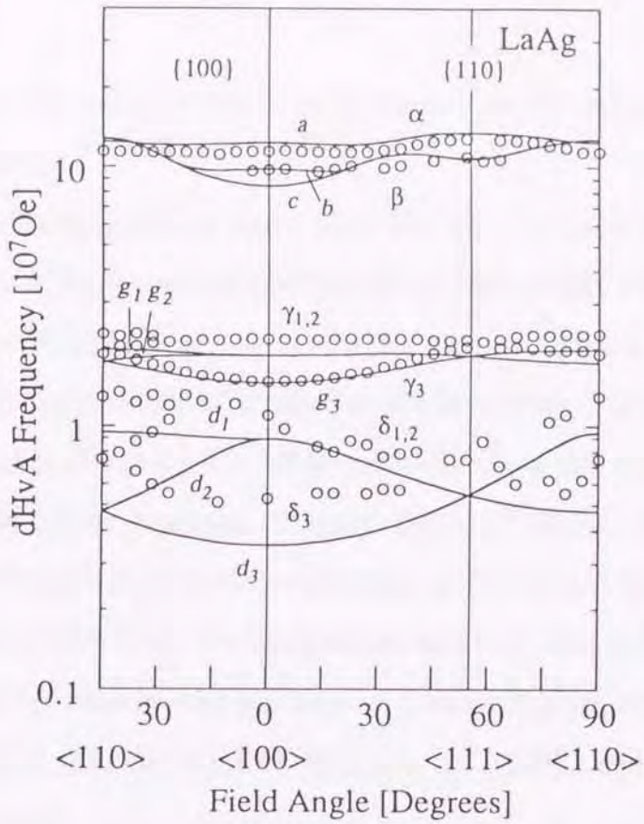

Fig. 6.6. Theoretical and experimental frequencies of the de Haas-van Alphen effect for LaAg as a function of the direction of a magnetic field on the {100} and {110} planes. The solid curves and the alphabets show the theoretical results which are derived using the Fermi surfaces shown in Figs. 6.2 ~ 6.5. Small circles and the Greek letters show the experimental results (Motoki *et al.* 1995).

Table 6.V. Theoretical and experimental results for the extremal cross section and the cyclotron effective mass for the Fermi surface of LaAg. The experimental and theoretical results by Niksch *et al.* are taken from Table 2 and Fig. 6 in their paper (Niksch *et al.* 1987). The other experimental results are the results by Motoki *et al.* (1995).

Branch	Band	Direction	Extremal areas				Effective masses			
			Expt.[a]	Expt.[b]	Calc.[c]	Calc.[b]	Expt.[a]	Expt.[b]	Calc.[c]	Calc.[b]
Large hole sheet at R										
b (β)	7	<100>	9.756		9.799				1.26	
b ≈ c (β)	7	<110>			12.827				1.47	
b (β)	7	<111>	10.600		10.921		3.64		1.43	
c	7	<100>			8.458				1.12	
c	7	<111>			10.732				1.41	
Small hole sheet at M										
$g_1 \approx g_2$ ($\gamma_1 \approx \gamma_2$)	7	<100>	2.1565	2.125	1.868	1.86	0.85	0.67	0.42	0.41
g_3 (γ_3)	7	<100>	1.4790	1.480	1.460	1.41	0.68	0.60	0.40	0.36
$g_1 \approx g_2$ ($\gamma_1 \approx \gamma_2$)	7	<110>	1.8900	1.860	1.763	1.72	0.98	0.92	0.46	0.44
g_3 (γ_3)	7	<110>	2.2600		1.971	1.97	0.96		0.48	
$g_1 \approx g_2 \approx g_3$ ($\gamma_1 \approx \gamma_2 \approx \gamma_3$)	7	<111>	2.1200	2.000	1.865	1.82	1.47	0.96	0.47	0.46
Large electron sheet at Γ										
a (α)	8	<100>	11.485		12.366		1.75		1.08	
a (α)	8	<110>	11.460		12.464		1.86		1.11	
a (α)	8	<111>	12.700		13.536		1.75		1.23	
Small electron sheet at X										
$d_1 \approx d_2$ ($\delta_1 \approx \delta_2$)	8	<100>	1.097		0.892	1.25			1.84	
d_3 (δ_3)	8	<100>	0.529	0.520	0.353	0.57		1.00	0.68	0.63
$d_1 \approx d_2$ ($\delta_1 \approx \delta_2$)	8	<110>	0.7508	0.720	0.474	0.71		1.10	0.88	0.87
d_3 (δ_3)	8	<110>	1.2947		0.948	1.26			1.98	
$d_1 \approx d_2 \approx d_3$ ($\delta_1 \approx \delta_2 \approx \delta_3$)	8	<111>	0.750	0.740	0.546	0.82		1.72	0.99	1.05

a Motoki *et al.*
b Niksch *et al.*
c Present work

mass is usually enhanced by many-body effects, the assignment of α to a may be reasonable.

The theoretical branches b and c have the frequencies which are similar to those of the experimental branch β, though the branch β is observed in a limited range of angles. In the vicinity of the <100> direction, the nearly constant frequencies of the branch β imply that they may be assigned to the branch b. The cyclotron mass has not been measured in the <100> direction. Though Table 6.V shows that the ratio m_c^*/m_0 for the branch β is 2.5 times as large as that of the branches b and c in the <111> direction, the assignment of β to b may not be unreasonable. The reason why the branch β has not been observed in the vicinity of the <110> direction by Motoki *et al.* (1995) will be discussed in the next section.

In a low-frequency region, our assignments are consistent with the previous assignments by Niksch *et al.* (1987). Thus, the branches γ_1, γ_2, γ_3 are assigned to the branches g_1, g_2, g_3, respectively. Table 6.V shows that the ratio m_c^*/m_0 for the branches γ_1, γ_2, γ_3 is 1.7 ~ 3.1 times as large as that of the branches g_1, g_2, g_3. The branches δ_1, δ_2, δ_3 are assigned to the branches d_1, d_2, d_3, respectively, and the ratio m_c^*/m_0 for the branches δ_1, δ_2, δ_3 is larger than that of the branches d_1, d_2, d_3 by 25% ~ 74%.

The theoretical total density of states at E_F, $N(E_F)$ = 22.3 states/Ryd.cell, corresponds to the electronic specific heat coefficient γ_{band} of 3.9 mJ/K^{2}mol. The experimental value is γ_{exp} = 7.7 mJ/K^{2}mol (Seipler *et al.* 1977). The experimental electronic specific heat coefficient may be enhanced by the many-body effects which cannot be taken into account by the exchange-correlation potential in the LDA. The enhancement factor λ for γ_{exp} due to such many-body effects is defined such that $\gamma_{exp} = (1 + \lambda) \gamma_{band}$ and estimated as $\lambda = 0.97$.

It is possible to define the enhancement factor due to similar many-body effects also for m_c^*, λ_c, which may vary from orbit to orbit. From Table 6.V, λ_c is estimated as 0.42 ~ 0.68 for the the large hole sheet and 1.5 for the large electron sheet, as far as four observed cyclotron effective masses are used. These Fermi surface sheets are likely to contribute dominantly to the total density of states at E_F. The estimate for λ_c is roughly consistent with that for γ_{exp} on the average.

6.5. *Local Curvature of the Large Hole and Electron Sheets*

Figure 6.6 shows that the experimental branch β disappears at angles in the vicinity of the <110> direction of a magnetic field, and that only one frequency belonging to the branch β has been observed in the <100> direction. Here we investigate the local curvature of the large hole sheet round the extremal cross sections as a possible origin of these experimental results for the branch β.

The intensity in the oscillation of the dHvA effect is inversely proportinal to the square root of the second derivative, A'', of the extremal area with respect to the wave vector component parallel to a magnetic field (Schoenberg 1984). The result of the calculation for the factor $|A''|^{-1/2}$ on the large hole sheet is shown in Fig. 6.7, where its free-electron value, $(2\pi)^{-1/2}$ (= 0.399), is also plotted. On the large hole sheet, the second derivative A'' both of the branches *b* and *c* can become large in the <110> direction, because in this direction the orbit passes on four bulges. As is shown in Fig. 6.7, the factor $|A''|^{-1/2}$ for these branches decreases to the half of the free-electron value in a limited range of angles around the <110> direction Thus, the disappearance of the branch β in the vicinity of the <110> direction may be ascribed mainly to the damping effect due to the local curvature.

Another possible origin is an increase of m_c^* for the branch β, because m_c^* enters another reduction factor (Schoenberg 1984) and its increase tends to reduce the intensity. In Fig. 6.7, the ratio m_c^*/m_0 calculated for the branches *b* and *c* is also plotted as a function of the direction of a magnetic field. Figure 6.7 shows that m_c^* is larger near the <110> direction than in other directions. Thus, m_c^* may contribute partly to the damping in the branch β near the <110> direction. Concerning a quantitative estimation of the damping effect due to m_c^*, however, we must know more about the direction dependence of the enhancement factor for m_c^*.

In the <100> direction, the second derivative of the branch *b* becomes large, because in this direction the orbit passes on four bulges, while that of the branch *c* is small, because the orbit does not pass on any bulges. Figure 6.7 actually shows that, in the vicinity of this direction, the factor $|A''|^{-1/2}$ in the branch *b* becomes smaller than that in the branch *c*, while the ratio m_c^*/m_0 in the branch *b* is larger than that in the branch *c*. This difference implies that in the vicinity of the <100> direction it may be difficult to detect the dHvA signal arising from the branch *b* as compared to the branch *c*. Thus, the observed branch should be assigned to the branch *c*. As we suggest in the last section, however, the angle dependence of the observed branch is similar to that of the branch *b*. It is not clear at present whether the observed branch should be assigned to the branch *b* or to the branch *c*.

For the sake of comparison, the factor $|A''|^{-1/2}$ and the ratio m_c^*/m_0 are calculated also for the branch *a* and the results are shown in Fig. 6.8. The factor $|A''|^{-1/2}$ makes a sharp peak at about 30° both on the {100} and {110} planes, and becomes small around the <111> direction. The ratio m_c^*/m_0 is quite isotropic, i.e. its angle variation remains within 14%. The experimental value for m_c^*/m_0 is also isotropic. The

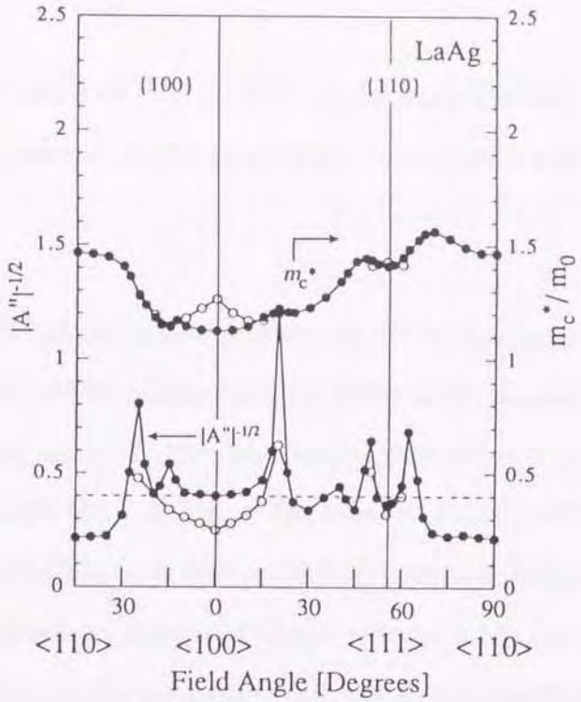

Fig. 6.7. Local curvature factor $|A''|^{-1/2}$ and the ratio of the cyclotron effective mass m_c^* to the free-electron mass m_0 calculated for the theoretical frequency branches *b* (open circles) and *c* (solid circles) as a function of the direction of a magnetic field on the {100} and {110} planes. Solid lines are guides to the eye, and the dashed line show the free-electron value of the curvature factor, i.e. $|A''|^{-1/2} = (2\pi)^{-1/2}$.

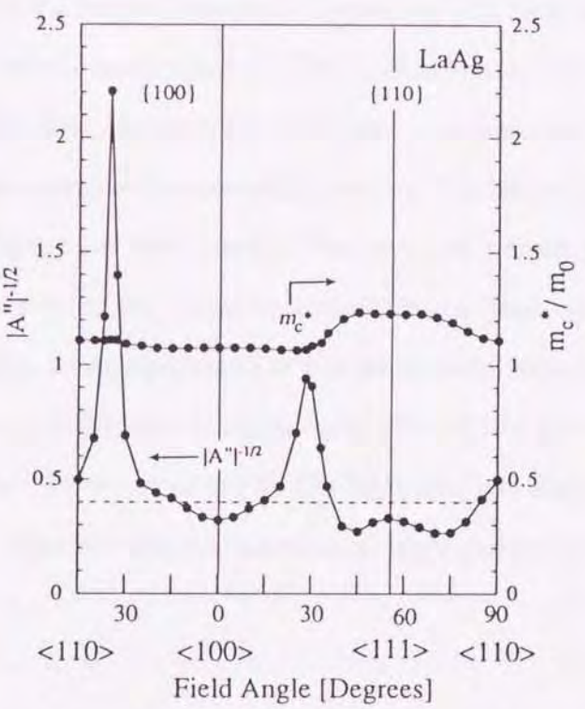

Fig. 6.8. Local curvature factor $|A''|^{-1/2}$ and the ratio of the cyclotron effective mass m_c^* to the free-electron mass m_0 calculated for the theoretical frequency branches *a* (solid circles) as a function of the direction of a magnetic field on the {100} and {110} planes. Solid lines are guides to the eye, and the dashed line show the free-electron value of the curvature factor, i.e. $|A''|^{-1/2} = (2\pi)^{-1/2}$.

minimum in the factor $|A''|^{-1/2}$ is still larger than the half of the free-electron value, in contrast to the case of the branches *b* and *c*.

6.6. *Conclusion*

We have calculated the electronic structure for LaAg self-consistently by a fully-relativistic APW method in the MTA with the exchange-correlation potential in the LDA. The Fermi surface is found to consist of a large hole sheet at the Γ point, a large electron sheet at the R point, three inequvalent small hole sheets at the M points and three inequvalent small electron sheets at the X points in the simple cubic Brillouin zone. This result confirms well the Fermi surface which was previously predicted by the band calculation for LaAg by Niksch *et al.* (1987). The existence of the small hole and electron sheets were previously confirmed experimentally (Niksch *et al.* 1987).

The existence of the large hole and electron sheets has recently been confirmed by the measurement on the dHvA effect by Motoki *et al.* (1995). The observed behavior of the dHvA frequency branches in a high-frequency region is explained reasonably well on the basis of the theoretical large Fermi surface sheets. However, the frequency branches originating from the large hole sheet have been observed only partially, because the local curvature of the large hole sheet tend to weaken the intensity of the dHvA signal near the <110> direction owing to its peculiar shape. In order to verify the shape of the large hole sheet predicted, further experiments on samples of high purity is desirable.

7. Effects of the 5*f* Bands on the Fermi Surface of Th Metal

7.1 *Introduction*

Th metal has attracted much interest and its electronic structure, particularly the Fermi surface, has been investigated both theoretically and experimentally, because it is located at the beginning of the actinide series, and its crystal structure is simple, i.e., it has the face-centered-cubic crystal structure below 1400° C. In Th, the 5*f* bands lie slightly above the Fermi level and affect the electronic structure in the vicinity of the Fermi level appreciably. Thus a careful investigation of the Fermi surface of Th is important as a first step toward a deep understanding of the nature of the 5*f* electrons in the actinides. In this paper, we investigate the electronic structure and the Fermi surface for Th in detail by band theory.

Its magnetic susceptibility increases slightly with temperature, and the room-temperature magnetic susceptibility is 9.7×10^7 emu/mole (Greiner and Smith 1971). The low-temperature specific heat constant γ is reported to be 4.31 and 4.08 mJ/K^{2}mole (Gordon *et al.* 1966). It was the first element in the actinide series for which the dHvA effect was measured, and the topology of the Fermi surface was suggested (Thosen et al. 1967 ; Boyle and Gold 1969). Soon later, the band calculations were performed in various methods to explain the Fermi surface shape and the cyclotron effective mass.

Gupta and Loucks (1969, 1971) have first derived the Fermi surface for Th by a non-self-consistent calculation with a relativistic APW method. In their calculation, the Slater exchange potential was used, and the whole 5*f* bands appeared in the middle of the valence band. This result is unphysical, because the 5*f* bands should be almost unoccupied in Th. Therefore, Gupta and Loucks (1969) removed them out artificially. The Fermi surface that they predicted is simple. It consists

of a hole sheet centered at the Γ point ("rounded cube"), four hole sheets centered at the L points ("dumbbells") and twelve electron sheets which lie across the Σ axes ("lungs"). These three kinds of sheets explained the behavior of the experimental dHvA frequency branches qualitatively well. It was not easy, however, to identify the origin of the experimental dHvA frequency branches clearly, because they did not calculate the dependence of the dHvA frequencies on the direction of a magnetic field, but merely suggested it (Boyle and Gold 1969). Furthermore, the quantitative disagreements between theory and experiment remained about the volume surrounded by hole sheets.

In order to clarify the influence of the 5*f* states on the Fermi surface, Koelling and Freeman (1975) have investigated a change of the band structure by using the local exchange potential with a scale factor which varies from 1 to 2/3. The local exchange potential is derived with a crystal charge density which is generated by overlapping atomic charge densities obtained under an assumed configuration. Koelling and Freeman (1975) suggested that both the decreasing in the exchange scale factor and the inclusion of the 5*f* states in the band structure could be in the correct direction to remove the disagreement between theory and experiment about the volume of hole sheets.

On the basis of an itinerant 5*f* electron model, Skriver and Jan (1980) have performed the first self-consistent calculation for Th with a relativistic linear-muffin-tin-orbital (LMTO) method in the atomic-sphere approximation by using the exchange and correlation potential which is devised in the LDA by von Barth and Hedin (1972). By a self-consistent treatment, they confirmed the importance of the hybridization of the valence band with the 5*f* states stressed by Koelling and Freeman (1975). In order to fit the Fermi surface to the experimental results for the dHvA effect in the high-symmetry directions, they found it necessary

to shift the Fermi level by 2 mRyd. for the cube, -14 mRyd. for the dumbbell, and -6 mRyd. for the lung. In all the previous calculations for Th, the dHvA frequencies have been calculated only in the high-symmetry directions of a magnetic field, and their angular dependence has been calculated neither on the {100} plane nor on the {110} plane.

On the basis of the itinerant 5*f* electron model, we have recently calculated the electronic structure and derived the Fermi surface for two interesting U compounds, UC and UB_{12}, by using a self-consistent, relativistic APW method with the exchange and correlation potential in the LDA (Hasegawa and Yamagami 1990 ; Yamagami and Hasegawa 1991). We could explain reasonably well the magnitude and the angular dependence of the major experimental dHvA frequency branches without introducing any adjustable parameters.

In the light of our experience of these U compounds, the magnitude of the Fermi energy shifts that Skiver and Jan (1980) introduced for Th seems to be somewhat too large. At present, it is not clear whether these errors should be ascribed to the inadequacy of the LDA and/or the shape approximation to the potential. Furthermore, the possibility that they may imply limitations of the relativistic LMTO method when it is applied to the actinides cannot be ruled out.

Judging from these previous studies on Th, it seems necessary to re-examine the Fermi surface for Th as carefully as possible even within the framework of conventional band theory which is based on the LDA. Some errors may be inevitable because of the simplification adopted in the treatment of the exchange and correlation potential and the spatial shape of the crystal potential. We believe it rather important, however, to clarify the property of limitations inherent in such band theory. It is possible to clarify a part of the limitations at least by investigating the Fermi surface carefully.

In this chapter, within the framework of the LDA, we recalculate the energy band structure and derive the Fermi surface for Th by a method different from Skiver and Jan (1980), i.e., by a self-consistent, relativistic APW method, and investigate the angular dependence of the extremal cross-sectional areas of all sheets of the Fermi surface as carefully as possible. As a result, we find that theoretical results can explain the angular dependence of the available experimental dHvA frequency branches reasonably well. In addition, we propose a new assignment of the theoretical and experimental frequency branches which may be more reasonable than the previously suggested one, and also predict the existence of several new dHvA frequency branches, which hopefully may serve as a useful guide for future experimental investigations.

7.2 *Method of Calculation*

To calculate the energy band structure for Th metal, we here apply a self-consistent, relativistic, symmetrized APW method with the exchange and correlation potential in the LDA. The shape of the one-electron potential is determined in the MTA. The radius of the APW sphere is chosen to be the half of the nearest-neighbor Th-Th distance, i.e., $a/2\sqrt{2}$, where a is the lattice constant. The APW spheres occupy 74% of the whole space in a crystal. The lattice constant and other crystal constants used in this calculation are listed in Table 7.I.

Table 7.I Crystal constants of Th used in the calculation. The lattice constant is taken from Vilars and Calvert (1986).

Crystal structure	FCC
Space group	Fm3m
Lattice constant, a	9.608316 a.u.
APW sphere radius	3.397053 a.u.

A starting crystal charge density for the self-consistent iteration procedure is constructed by a superposition of the relativistic charge density for neutral Th atom (Rn, $6d^2 7s^2 5f^0$), which is calculated self-consistently with the relativistic method of Liberman *et al.* (1965), where Rn means the atomic configuration of Rn atom. In the atomic calculation, the same exchange and correlation potential form is used as in the crystal, and the spin-orbit splitting in the $6p$, $6d$ and $5f$ state is found to be 585 mRyd., 37 mRyd. and 48 mRyd., respectively. During the iterations, the Rn core states except the $6p^6$ state are treated in the frozen-core approximation.

Throughout this band structure calculation, about 320 relativistic APW basis functions and the total angular momenta up to 15/2 are used to expand the Bloch function. These numbers of the expansion correspond to 160 plane waves and the angular momenta up to 7, which are determined under the condition that the eigenvalues should converge well within a few mRyd.

In each cycle of the self-consistent iteration processes, the charge density is calculated at nineteen $\boldsymbol{k}$ points, i.e., five symmetry points, seven points on the symmetry axes and seven points on the symmetry planes, which correspond to 256 points distributed uniformly over the full Brillouin zone. Using the final self-consistent charge density, the eigenvalues are calculated at many symmetry and general points, totally 231 points in the irreducible 1/48 parts of the Brillouin zone.

7.3 *Results of calculation*

7.3.1 *Fully relativistic energy band structure*

Figure 7.1 shows the result of this calculation for the energy band structure for Th along the symmetry axes in the Brillouin zone. The Fermi energy E_F is located at 0.6200 Ryd. Three $6p$ bands which lie in

the energy region between -1.2 Ryd. and -0.4 Ryd. are omitted from Fig. 7.1. In the energy range below E_F, this result is similar to that of Gupta and Loucks (1969) who used the Slater exchange and artificially removed the 5*f* bands. In addition, this result looks similar to the result of Koelling and Freeman (1975) with the exchange scale factor of 2/3 and also the result of Skriver and Jan (1980) who used the exchange and correlation potential of von Barth and Hedin (1972).

In order to investigate the character of each band, the charge distributions for many states at the Γ point are partitioned according to the angular momenta, and listed in Table 7.II. As is shown in Table 7.II, at the Γ point, the lowest Γ_6^+ state consists dominantly of the *s* state. The Γ_6^-, two Γ_7^- and two Γ_8^- that lie above it specify the *f* bands, while the Γ_7^+ and two Γ_8^+ states specify the *d* bands. Figure 7.1 shows that these states, especially the *d* states, form wide bands. The *f* bands split into two subbands which correspond to the total angular momenta $j = 5/2$ (lower bands) and 7/2 (upper bands), and the magnitude of the splitting is slightly greater than the spin-orbit splitting in the atomic 5*f* state because of the crystal field effect. As is shown in Fig. 7.1, the main part of the *f* bands exist just above E_F.

Although the *d* bands and the *f* bands do not hybridize at the Γ point, they do at other points with low symmetry. For example, along the Δ axis, the Δ_7 branch starts from the Γ_7^- state (0.663 Ryd.) with large dispersion. In this Δ_7 branch, the *d* states and the *f* states hybridize. At the X point, this branch is compatible with the X_7^+ state, in which the *f* components vanish and the *d* components become dominant. The Fermi surface is constructed by the second and the third bands, both of which contain the *f* components appreciably through the *d*-*f* hybridization. Thus, the 5*f* states may affect the Fermi surface, though the main part

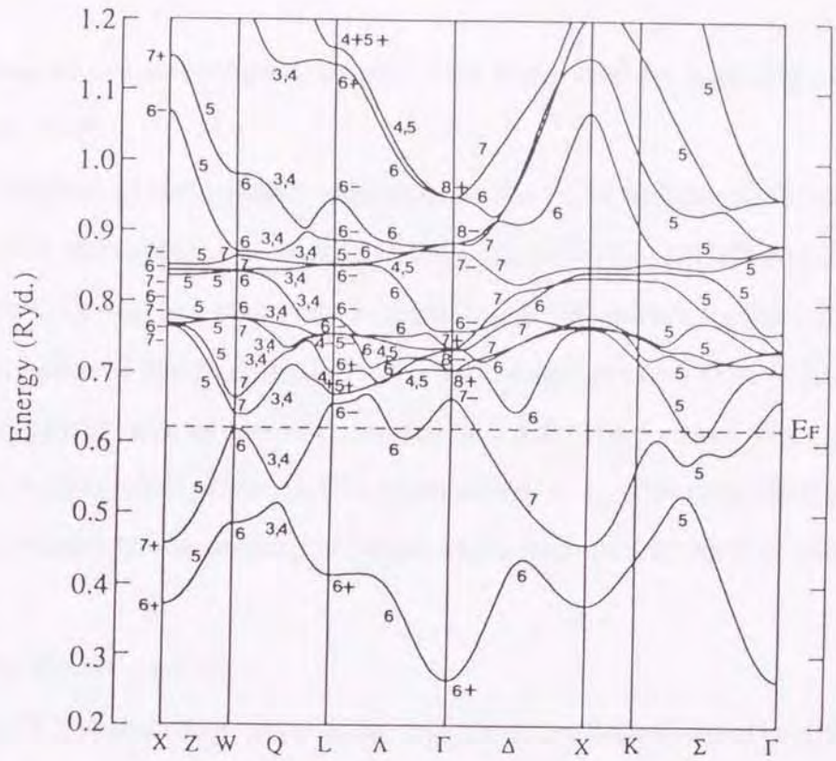

Fig. 7.1. Relativistic energy band structure for Th in the vicinity of the Fermi energy E_F.

Table 7.II Charge distributions partitioned into the angular momenta for the Bloch states at the Γ point. Components are shown in percent.

Band	Bloch state	Energy (Ryd.)	Outer region	Th APW sphere			
				s	*p*	*d*	*f*
1	Γ_6^+	0.264	36	64	0	0	0
2	Γ_7^-	0.663	11	0	0	0	88
3,4	Γ_8^+	0.704	10	0	0	86	0
5	Γ_7^+	0.733	11	0	0	85	0
6,7	Γ_8^-	0.735	6	0	0	0	93
8	Γ_6^-	0.760	7	0	0	0	92
9	Γ_7^-	0.871	0	0	0	0	99
10,11	Γ_8^-	0.884	0	0	0	0	99
12,13	Γ_8^+	0.948	5	0	0	91	0

of the *f* bands are unoccupied, as was first suggested by Koelling and Freeman (1975).

The number of the valence electrons in the APW sphere partitioned according to the angular momenta is 0.47 (*s*), 6.00(*p*), 1.96 (*d*) and 0.41(*f*). There are 1.22 valence electrons outside the APW sphere in the primitive cell. The value of the *f* component is a little smaller than that of Skriver and Jan (1980), who reported the value of 0.5 for the *f* state. The density of states is calculated at E_F as 16.2 states/Ryd. cell. The contribution from the *f* states to the density of states at E_F amounts to 30 % of the total.

7.3.2 *The Fermi surface*

Figure 7.1 shows that the second and the third bands construct the Fermi surface. The second band constructs the hole sheets which consist of a rounded cube centered at the Γ point and four dumbbells centered at the L points, as is shown in Fig. 7.2. The dumbbell is stretched along the <111> direction and has triangular ends which are connected by the hyperbolic neck. The third band constructs the electron sheets which consist of twelve lungs which lie across the Σ axis, as is shown in Fig. 7.3. The lung consists of two lobes and a slender junction.

All these Fermi surface sheets are tiny and closed, so that they cannot hold open orbits. The hole sheets contain totally 0.14 holes/cell, and the electron sheets contain totally the same number of electrons. This result is consistent with the fact that Th metal has even number of electrons per primitive cell, i.e., it is a compensated metal.

7.3.3 *Extremal cross-sections of the Fermi surface*

We calculate the extremal cross-sectional area of the hole sheets and the electron sheets of the Fermi surface in various directions. The extremal cross-sectional area *A* is related to the dHvA frequency *F* by the

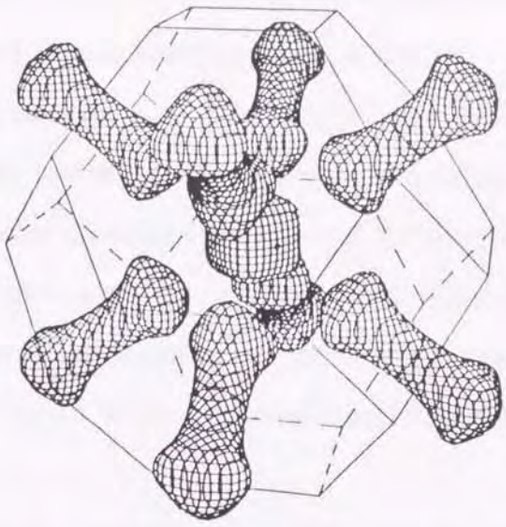

Fig. 7.2. The hole sheet of the Fermi surface in the second band for Th. The hole sheet consists of the rounded cube centered at the Γ point and the dumbbells centered at the L points.

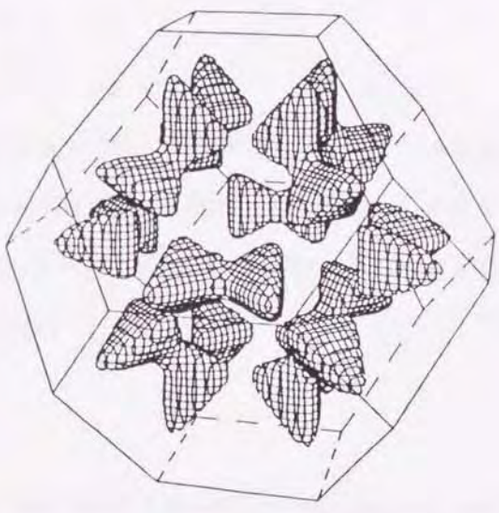

Fig. 7.3. The electron sheet of the Fermi surface in the third band for Th. The electron sheet consists of the lungs which lie across the Σ axes.

well-known formula $F = (ch/2\pi e)A$. It can be written as F[Oe] = 1.59936 × $10^8 A$ for Th, where A is measured in units of $(2\pi/a)^2$.

We use the same notations as those of the Gupta-Loucks model for the orbits except that the orbits c and d are interchanged in order to be consistent with Skriver and Jan (1980), and Koelling and Freeman(1975). In the present work, we have discovered many new orbits on the lung and the dumbbell. New orbits are the orbits r, s and w on the lung and the orbits t, v, x and q on the dumbbell, and added in the following analysis.

Figure 7.4 shows the theoretical dHvA frequencies as functions of the magnetic-field direction on the {100} and {110} planes. In Fig. 7.4, the chain curve, dashed curves and solid curves show the dHvA frequency branches which are calculated from the cube, the dumbbells and the lungs, respectively. In the following, we explain from what orbit these theoretical branches originate on individual sheets of the Fermi surface.

Cube

The cube produces a single dHvA frequency branch which exists in all directions. Figure 7.5 shows three orbits n, f and k which run around it on the plane perpendicular to the <100>, <110> and <111> directions, respectively.

Dumbbell

It is sufficient to deal with the orbits running on the four independent dumbbells, as is shown in the Fig. 7.6. In the <100> direction, there exist two kinds of orbits. One is x which runs around the L point with the minimum area, and another is q which runs around the triangular end with the maximum area. Since the orbits which run around the

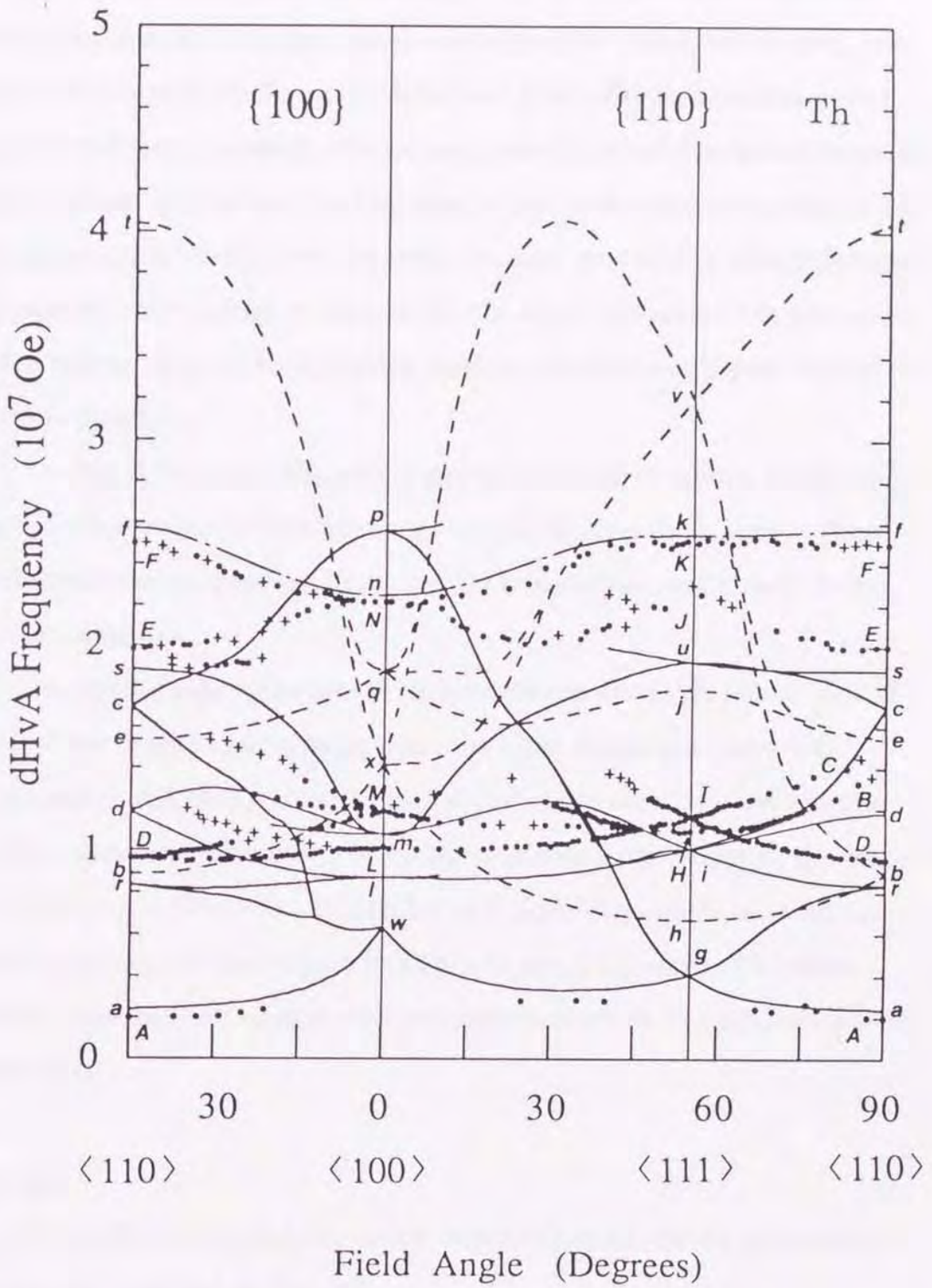

Fig. 7.4. Theoretical and experimental frequencies of the de Haas-van Alphen effect for Th as a function of the direction of a magnetic field on the {100} and {110} planes. The chain curve, the dashed curves and the solid curves show the frequencies calculated from the cube, the dumbbells and the lungs, respectively. Small circles and crosses show the experimental results of Boyle and Gold (1969). The alphabets and the Greek letters show the theoretical and experimental results, respectively.

equivalent points on four independent dumbbells have the same areas in the <100> direction, both x and q are degenerate fourfold.

On the {100} and {110} planes, however, the degeneracy is resolved. The orbit x splits into two branches on the {100} plane, which turn into the orbits b and t in the <110> direction. Both of them have the center near the hyperbolic neck. The orbit q also splits into two branches on the {100} plane. One of the two branches, which is denoted as e in the <110> direction, originates from the orbit running around the triangular end, while the other, which is denoted as t in <110> direction, has the center that moves near to the hyperbolic neck as the field angle goes toward the <110> direction.

On the {110} plane, the orbit x splits into three branches, all of which originate from the orbits running around the hyperbolic neck. These orbits are denoted as h and v in the <111> direction, and b and t in the <110> direction.

The orbit q also splits into three branches on the {110} plane. One of the three branches originates from the orbit running around the triangular end, and is denoted as j in the <111> direction and e in the <110> direction. Other two branches originate from the orbit, the center of which moves from the triangular end to the hyperbolic neck as the field angle varies from <100> to <110> on the {110} plane. Therefore, these branches are united with the branches which are separated from the orbit x.

Lung

It is sufficient to seek the orbits that result from the six independent lungs, as is shown in Fig. 7.7.

In the <100> direction, there exist four kinds of orbits, i.e., w, l, m and p. The orbit w originates from the orbit running around the junction

part with the minimum area. The orbits l and m originate from the orbits running on the lobe with the maximum area. The orbit p originates from the orbit with the largest cross-sectional area of the lung. It is easy to see that the orbit p is degenerate twofold, and the orbits m, l and w are degenerate fourfold in the <100> direction.

On the {100} and {110} planes, these degeneracies are resolved partly. The orbit w splits into three branches on the {100} plane, which are denoted as a, r and c in the <110> direction. The orbits r and c have the minimum and maximum areas, respectively. Their centers are kept apart, until they coincide with each other in the vicinity of 10° on the {100} plane.

The orbit l splits into two branches on the {100} plane, which are denoted as r and d in the <110> direction. Both branches originate from the orbits running around the lobe.

The orbit m also splits into three branches on the {100} plane. One of the three branches has the twofold degeneracy and disappears in the vicinity of 20°. Other two branches are denoted as d and s in the <110> direction.

On the {110} plane, all branches which are separated from the orbits w, l and m are degenerate twofold. There exists only one branch from the orbit w on the {110} plane, which is denoted as g in the <111> direction and r in the <110> direction. As the field angle increases on the {110} plane, its center shifts in the direction from the junction part toward the lobe.

The orbit l splits into two branches on the {110} plane. One of the two branches becomes the orbit i in the <111> direction and the orbit c in the <110> direction. Another branch disappears in the vicinity of 10°.

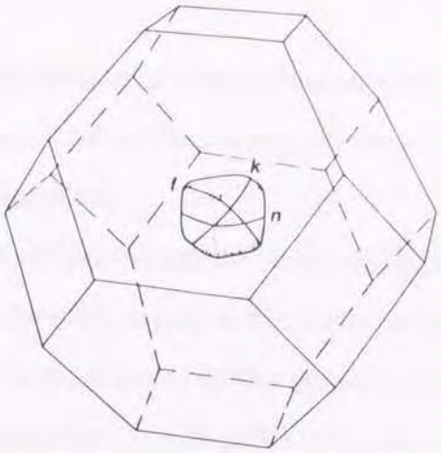

Fig. 7.5. Various extremal orbits on the cube, which are normal to the three high-symmetry directions: the orbits n, f and k are normal to the <100>, <110> and <111> directions, respectively.

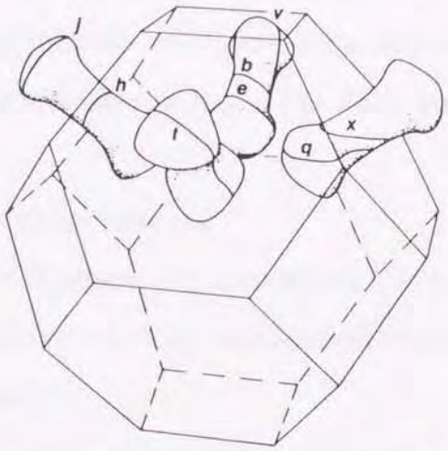

Fig. 7.6. Various extremal orbits on the dumbbells, which are normal to the three high-symmetry directions: the orbits q and x are normal to the <100> direction, the orbits b, e and t to the <110> direction, and the orbits h, j and v to the <111> direction.

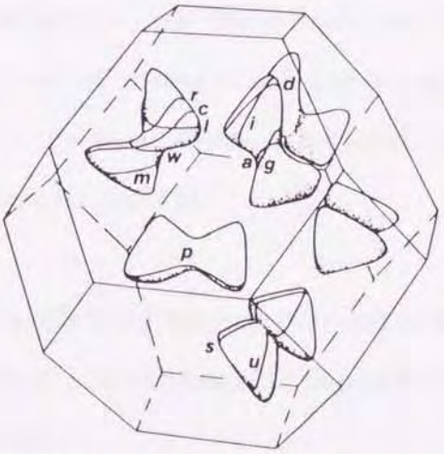

Fig. 7.7. Various extremal orbits on the lungs, which are normal to the three high-symmetry directions: the orbits l, m, p and w are normal to the <100> direction, the orbits a, c, d, r and s to the <110> direction, and the orbits g, i and u to the <111> direction.

The orbit m also splits into two branches on the {110} plane. These two branches have the extremal orbits i and u in the <111> direction, and r and c in the <110> direction.

The orbit p splits into two branches on the {110} plane. One of the two branches turns into the orbit u in the <111> direction and the orbit s in the <110> direction. It disappears in the angle range between 10° and 40° on the {110} plane. Another branch splits into two branches nearby 40°. The branch with a larger frequency originates from the maximum orbit on a lung, and coincides with the orbit i in the <111> direction and the orbit d in the <110> direction. The branch with a smaller frequency originates from the minimum orbit, and coincides with the orbit g in the <111> direction and the orbit a in the <110> direction.

7.4 *Comparison with experiments*

In this section, we compare the theoretical results for the dHvA frequencies, the cyclotron effective masses and the density of states with experimental results.

7.4.1 *dHvA frequency branches*

In Fig. 7.4, we show the theoretical dHvA frequency branches together with the experimental results of Boyle and Gold (1969). The experimental and theoretical orbits which are thought to have the same origin are labeled with the same capital and small letter, respectively, except for the experimental orbit D.

(A) *Cube*

(1) The theoretical branch n-k-f may correspond to the experimental branch N-K-F because of similar angular dependence and magnitude in the whole range of angles.

(B) *Dumbbell*

The frequency branches that are calculated from the dumbbell can explain the behavior of some experimental branches, though the quantitative agreement between theory and experiment is not so good as for the cube. In the <100> direction, the theoretical orbit *q* is not observed in the experiment. Therefore, the corresponding hypothetical orbit in this direction is supposed to be *Q'* for the sake of the following explanations. The magnitude of *Q'* may be slightly larger than that of the orbit *N*.

(2) On the {100} plane, the experimental branch *E-Q'* may be assigned to the theoretical branch *e-q* because of the similar angular dependence.

(3) On the {110} plane, the experimental branch *Q'-J-E* may be assigned to the theoretical branch *q-j-e* because of the similar angle dependence.

(4) On the {110} plane, the experimental branch *H-B* may correspond to a part of the theoretical branch *x-h-b* .

(C) *Lung*

The branches which originate from the lung can explain many experimental branches fairly well.

(5) The previous assignment (*d*, *D*) (Boyle and Gold 1969 ; Gupta and loucks 1969, 1971 ; Koelling and Freeman 1975 ; Skriver and Jan 1980) seems unreasonable to us, because on the {110} plane the angle dependence of the branch *I-D* contradicts that of the branch *i-d*. We suggest that the assignment (*r*, *D*) may be reasonable, because on the {110} plane the angle dependence of the branch *I-D* resembles that of the branch *i-r*.

The theoretical orbit *d* may be missed in the experiment. Therefore, the corresponding hypothetical orbit is supposed to be *D'* for the sake of the following discussions. The orbit *D'* should be observed in the range between *C* and *D* in the <110> direction.

(6) On the {110} plane, the experimental branch *L-I-C* may be assigned to the theoretical branch *l-i-c*.

(7) On the {110} plane, the experimental branch *M-I-D* may be assigned to the theoretical branch *m-i-r*.

(8) On the {100} plane, the experimental branch *L-D* may be assigned to the theoretical branch *l-r*.

(9) A part of the theoretical branch *m-u-c* may be observed in the angle range from 0° to 10° on the {110} plane.

(10) The theoretical branch *p-i-d* seems to be partly observed in the narrow angle range from 40° to 55°. The unobserved branch *I-D'* may follow it.

(11) On the {100} plane, the theoretical branch *l-d* may correspond to the experimental branch *L-D'*, though the latter branch is not observed in the vicinity of the <110> direction.

(12) On the {100} plane, the three experimental branches that are separated from the orbit *M* may be assigned to a part of the theoretical branch *m-s*, a part of the theoretical branch *m-d*, and the theoretical branch that disappears nearby 20°, respectively.

(13) On the {100} plane, the theoretical branch *w-a* is partly observed in the angle range from 20° to 45°. On the {110} plane, the theoretical branch *g-a* is partly observed in the angle range from 65° to 90°, and the branch *w-g* around 30°.

(14) On the {100} plane, the theoretical branch *p-c* seems to be partly observed in the vicinity of 30°.

There are theoretical branches which have not been confirmed in the experiment, as is shown in Fig. 7.4. An origin of the experimental branch which starts from *D* in the <110> direction and slightly increases on the {100} plane is not clear. The disagreements between theory and experiment will be discussed in the next section.

7.4.2 *Cyclotron effective mass*

The ratio of the cyclotron effective mass m_c^* to the free-electron mass m_0 can be expressed as $m_c^*/m_0 = 0.13612 \times dA/dE$ for Th. The ratio is calculated for each theoretical dHvA frequency in the three high-symmetry directions, and listed together with the previous theoretical results and the experimental results in Table 7.III. Compared with the theoretical results by Skriver and Jan (1980), our results for m_c^* are a little larger on the average, and approach closer to the experimental results. However, decisive disagreements between theory and experiment remain, and should be ascribed to many-body effects which band theory fails to take into account. The enhancement factor for m_c^* due to such many-body effects may be defined as $\lambda_c = (m_c^*)_{exp} / (m_c^*)_{band} - 1$, though it may vary from orbit to orbit. From Table 7.III, we obtain $\lambda_c = 0.21 \sim 0.74$ as far as the four experimental values for m_c^* are used.

7.4.3 *Density of states*

The density of states is calculated at E_F as 16.2 states/Ryd. cell, which corresponds to the electronic specific heat constant due to the band structure gband of 2.81 mJ/K^{2}mole. The experimental value for γ is γ_{exp} = 4.08 mJ/K^{2}mole and 4.31 mJ/K^{2}mole (Gordon *et al.* 1966), which may be renormalized similar to m_c^*. Thus, the enhancement factor for γ is defined as $\lambda = \gamma_{exp} / \gamma_{band} - 1$. We obtain $\lambda = 0.45 \sim 0.53$. Quantitatively, this result does not contradict the magnitude of the enhancement factors found for m_c^*.

Figure 7.8 shows the theoretical density of states (DOS) for occupied and unoccupied bands as a function of energy, which is convoluted with the Gaussian with the half width of 20 mRyd., together with the experimental DOS observed by means of the X-ray photoemission

Table 7.III Theoretical and experimental results of the extremal cross-sectional areas and the cyclotron effective masses in the three high-symmetry directions for Th. The cross-sectional area and the cyclotron effective mass are measured in units of $(2\pi/a)^2$ and the free-electron mass, respectively.

			external areas						effective mass			
surface	direction	orbit	expt.[a]	expt.[b]	calc.[c]	calc.[f]	calc.[b]	calc.[d]	expt.[e]	calc.[c]	calc.[f]	calc.[d]
cube	001	*N*	22.1	22.1	22.5	21.6	21.1	22.9	-0.75±0.03	-0.645	-0.55	-0.62
	110	*F*	25.1	24.7	25.7	24.2	23.5	26.6		-0.892	-0.72	-0.88
	111	*K*	25.1	25.2	25.4	24.3	23.7	26.3		-0.835	-0.69	-0.85
dumbbell	110	*B*	13.5	13.5	8.9	12.4	12.0	9.8		-0.315	-0.37	-0.25
	110	*E*	20.0	19.8	15.4	18.7	18.3	15.6		-0.402	-0.41	-0.34
	111	*H*	10.9	10.9	6.7	9.6	9.3	7.9		-0.228	-0.27	-0.19
	111	*J*	22.4	22.4	17.9	21.8	21.4	16.7		-0.506	-0.48	-0.41
	001	*Q*			18.7	21.8		16.0		-0.519	-0.81	-0.52
lung	110	*A*	2.5	2.014	2.4	1.6	1.74	1.7		0.217	0.20	0.15
	110	*C*	15.9	15.9	17.0	13.6	14.3	12.0		0.775	0.67	0.60
	011	*D*	9.6	9.6	8.36 (*r*)	8.3	8.7	8.6	0.58±0.01	0.339 (*r*)	0.44	0.32
	100	*L*	10.0	10.0	8.7	9.9	10.0	8.9	0.66±0.03	0.465	0.55	0.38
	111	*G*			4.1	30.3				0.374	0.43	
	111	*I*	11.7		10.1	10.9				0.384	0.40	
	001	*M*	11.8		10.7	11.2		10.6	0.58±0.03	0.373	0.34	0.35
	001	*P*			25.6	21.8		21.5		0.536	0.71	0.63

a Boyle and Gold (1969) as quoted by Koelling and Freeman (1975)
b Schirber, Schmidt and Koelling (1977)
c present work
d Skriver and Jan (1980)
e Boyle and Gold (1969)
f Koelling and Freeman (1975)

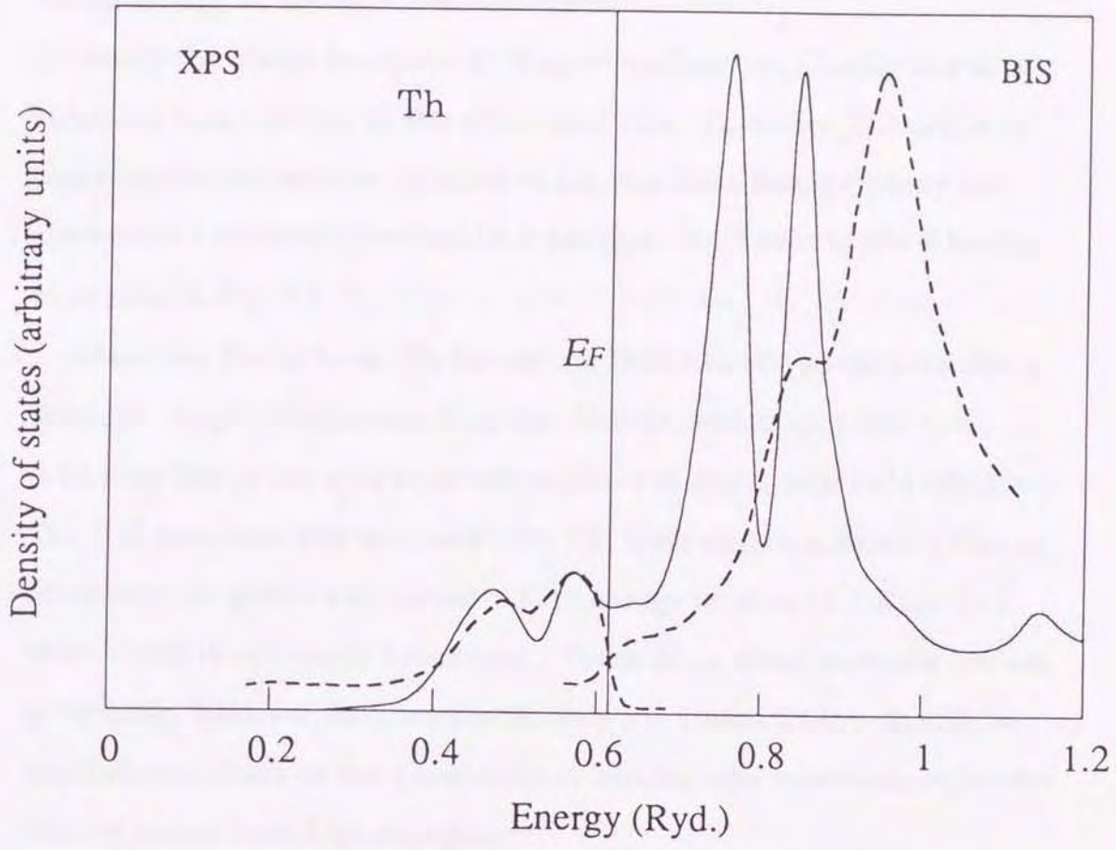

Fig. 7.8. The density of states as a function of energy for Th. The solid curve and the dashed curve show the theoretical density of states and the experimental XPS-BIS spectra of Baer and Lang (1980), respectively. The theoretical density of states is convoluted with the Gaussian with the half width of 20 mRyd. The experimental XPS-BIS spectra are adjusted to the same intensity at the Fermi energy.

spectroscopy (XPS) and the bremsstrahlung isochromat spectroscopy (BIS) by Baer and Lang (1980). The XPS and BIS results are adjusted to the same intensity at the Fermi energy. The theoretical result is normalized arbitrarily so that it has the same peak height above the Fermi energy as the experimental result.

Below the Fermi level, the XPS spectrum has two humps, and this structure looks similar to the theoretical one. Therefore, the origin of these two humps may be ascribed to the van Hove singularities (van Hove 1953) which exist along the Δ axes and the Σ axes in the *d* bands, as is seen in Fig. 7.1.

Above the Fermi level, the theoretical DOS has two peaks with about the same height originating from the *f* bands, which split into two subbands due to the spin-orbit interaction and the crystal field effect. The BIS spectrum has two peaks too, but their height is much different. Moreover, the peaks are shifted to high energy by about 0.1 Ryd., and their width is extremely broadened. These large disagreements are not surprising, however, because the density-functional theory should be applied essentially to the ground state, whereas the experiments involve excited states with high energies.

7.5 *Discussions*

In Table 7.III, the results of the calculation for the dHvA frequencies of all branches in the three high-symmetry directions are listed together with the previous theoretical results and the experimental results. Here we compare our results with the results by Skriver and Jan (1980), because their calculation is the only previous calculation that was carried out self-consistently.

For the cube, their results for the dHvA frequency are larger by 4% ~ 8% in the three high-symmetry directions than the experimental

results, while our results are larger by 1% ~ 4% than the experimental ones. For the dumbbell, their results are smaller by 22% ~ 28% than the experimental ones, while our results are smaller by 20% ~ 34% than the experimental ones. For the lung, their results are smaller by 10% ~ 32% than the experimental ones, while our results are smaller by 4% ~ 14% (and larger by 7% for the orbit C) than the experimental ones. Thus, for the cube and the lung, our results are in better agreement with the experimental results than their results. For the dumbbell, however, band theory has not been improved much.

It is clear that the dumbbell and the lung are a little too small in size, and also the dumbbell is too slender in shape, in agreement with the conclusion of Skriver and Jan (1980). Their calculational method was different from ours, i.e., they used a relativistic LMTO method and the exchange and correlation potential by von Barth and Hedin (1972), while we here use a relativistic APW method and the exchange and correlation potential by Gunnarsson and Lundqvist (1976). We are led to conclude that the dis-agreements between theory and experiment should be ascribed neither to the relativistic LMTO method nor to the relativistic APW method, but rather to limitations of the LDA and/or the muffin-tin approximation to the spatial shape of the potential.

Although band theory still should be improved, in the present work it becomes possible by a careful investigation on the angular dependence of the dHvA frequencies to identify the origin of many experimental branches much more clearly than previously. Furthermore, we can suggest that the new assignment (r, D) may be more reasonable than the assignment (d, D) which was previously proposed (Boyle and Gold 1969 ; Gupta and loucks 1969, 1971 ; Koelling and Freeman 1975 ; Skriver and Jan 1980), and also predict the existence of several new dHvA frequency branches.

Unfortunately, there are some theoretical branches which have not been confirmed, partly or entirely, in the available experiment. The intensity of the dHvA signals for the orbit whose area changes abruptly with the wave vector component parallel to a magnetic field becomes weak. For instance, it may not be easy to observe the branch w-a in the vicinity of the <100> direction, unless a sample of high purity is used in a measurement.

As is seen in Fig. 7.4, on the {100} plane there is an experimental dHvA branch which starts from D in the <110> direction, slightly increases and disappears at about 25°. This experimental branch is expected to originate from the lung, but actually its origin can be found neither on the lung in our calculation nor on any lungs which have been proposed previously (Boyle and Gold 1969 ; Gupta and loucks 1969, 1971 ; Koelling and Freeman 1975 ; Skriver and Jan 1980). The reason for this disagreement between theory and experiment is not clear. In order to solve remaining problems on the Fermi surface of Th, an improvement of the measurement of the dHvA effect in Th is highly desirable. We hope that our theoretical results will serve as a useful guide for future studies.

8. Conclusion

It is one of the most important problems in the modern condensed matter physics to clarify the electronic structures for the heavy-electron materials. As is shown in the previous chapters of this thesis, we have already improved a self-consistent band theory on the basis of the RLAPW method, and applied an improved theory to clarify the electronic structures and the Fermi surfaces for some *f*-electron materials. The electronic structure has been calculated for the rare-earth compounds, such as $CeRh_2$, $LaRh_2$, $YbGa_2$ and LaAg, and one actinide material, i.e. the Th metal, and theoretical results are found to explain experimental results for the dHvA effect reasonably well except for the cyclotron effective mass, so that the efficiency of the RLAPW method has also been established as far as the Fermi surface shape is concerned. The band calculations are based on the itinerant-electron model for the 4*f* electrons in the rare-earth compounds and the 5*f* electrons in the actinide. The results for these materials are summarized as follows.

The Fermi surface for $CeRh_2$ consists of two nearly spherical hole sheets and a hollow electron sheet with eight windows which are open in the <111> direction. All of the sheets are centered at the Γ point. The spherical property of the Fermi surface explains qualitatively well the behavior of the experimental dHvA frequency branches, and candidates for the frequency branches which may be missed in the experiments are suggested. In addition, the properties of the Fermi surface for $LaRh_2$ seem different from those for $CeRh_2$, and both of them can be explained roughly by respective theoretical Fermi surface sheets. These results suggest that the 4*f* electrons in $CeRh_2$ may be itinerant. The itinerant nature of the 4*f* electrons in $CeRh_2$ should be concluded, however, only when all the dHvA frequency branches, especially high-frequency branches, are observed.

The Fermi surface for $YbGa_2$ consists of three hole sheets centered at the Γ point and three electron sheets centered at the M points. All the hole sheets look like deformed ellipsoids of revolution having the axis of revolution in the *c* direction. Each of the electron sheets looks like a distorted square cushion. The origins of all of the observed dHvA frequency branches can be identified clearly by using these theoretical Fermi surface sheets. Theoretical cyclotron effective masses are too large, suggesting that the effect of the 4*f* bands on the Bloch states in the vicinity of the Fermi level may be too strong. This problem seems to be concerned with limitations inherent in the LDA, and therefore is a challenging problem for band theory which should be solved in the near future.

The Fermi surface for LaAg is found to consist of large hole and electron sheets which are centered at the Γ point and the R point, respectively, as well as small hole and electron sheets which are centered at the M points and the X points, respectively. These Fermi surface sheets can explain reasonably well the experimental results for the dHvA effect. Especially, both the magnitude and the angle dependence of the dHvA frequency branch which originates from the large electron sheet are in good agreement with the experimental ones. The reason why the experimental branch β disappears around the <110> direction can be explained from the peculiar shape of the large hole sheet.

In Th metal, the Fermi surface consists of hole sheets, which are shaped like a rounded cube centered at the Γ point and dumbbells centered at the L points, and electron sheets which look like lungs centered at the Σ axis. The extremal cross-sectional area of the Fermi surface is calculated carefully as a function of the direction of the normal on the {100} and {110} planes, and compared with the experimental results for the dHvA effect. As a result, it becomes possible to identify the origin of many dHvA frequency branches more clearly. In addition, a new assignment of the

theoretical and experimental dHvA frequency branches is proposed, and the existence of several new branches is predicted also. The quantitative comparison between theory and experiment suggests that the dumbbell may be too slender in shape, in agreement with the previous work (Skriver and Jan 1980). This disagreement should be ascribed to the limitations of the LDA and/or the MTA.

Since a band picture plays a basic role on the comprehension for the origins of the anomalous physical properties discovered in the heavy-electron system, the studies on the electronic structures and the Fermi surface by means of band theory will become more important in the near future. In order to understand the behavior of the heavy-electron system theoretically, we will have to clarify the electronic structures for more kinds of the *f*-electron materials including the hevey-electron compounds.

As for the Ce compounds, it is necessary to confirm more firmly that the Fermi surface of the paramagnetic Ce compounds both in the valence fluctuation and dense Kondo regimes can be explained reasonably well by band theory on the basis of the itinerant-electron model for the 4*f* electrons. The rare-earth materials except the Ce compounds, such as the Yb compounds, should also be studied extensively both on theoretical and experimental sides in order to understand further the nature of the 4*f* electrons in the rare-earth compounds.

On the other hand, the behavior of the 5*f* electrons in the actinides is extremely various and the understanding for its origin seems to require new physical concepts. Recently the actinide compounds have attracted much interest for many reasons, and in particular, the Fermi surface of the uranium compounds having the magnetic order has been observed directly by the dHvA effect measurements. Therefore, reliable band calculations in which the magnetism is taken into account is desired urgently. The band calculations on the basis of the local-spin-density

approximation (LSDA) (Kohn and Sham 1965, von Barth and Hedin 1972) have already been performed on the 3*d* transition metals and their compounds. The LSDA theory works fairly well for 3*d* transition metals, but it is constructed only for spin-polarized systems. As is already emphasized in this thesis, the relativistic effects are extremely significant in the *f*-electron materials. Therefore, in order to calculate the band structures of *f*-electron materials with magnetic orderings, both the spin polarization and the relativistic effects should be taken into account in a united formalism. The pioneering studies on these problems have been carried out by Eriksson, Johansson, Brooks and their collaborators.[1] At present, the RLAPW method described in this thesis is limited to a calculation for the paramagnetic state. As a next study, we plan to improve the RLAPW method into a useful method suitable for the magnetic actinide materials, in particular the magnetic uranium compounds.

Although the density-functional theory in the LDA has proven to work quite well for many *f*-electron materials, it is an important and fundamental problem in band theory to clarify its limitations and improve it. An approach to this problem is solving the correlated Hartree-Fock equation in which the exchange term is contained in a non-local form and corrected with correlations. As a guide to construct a correction to the LDA, the Hartree-Fock formalism has already been confirmed to be valid for an atomic theory (Desclaux and Freeman 1984). In addition, although Norman and Koelling (1993) have pointed out an improper treatment of Hund's rule effects in the LSDA, it also can be remedied by using the Hartree-Fock formalism. It is a beneficial attempt to apply the correlated Hartree-Fock formalism to the calculations for the solids. A performance of the calculations on the basis of the Dirac-Fock equation,

---

[1] For instance, see, O. Eriksson: Doctor Thesis (Uppsala Univ., 1989).

which includes the relativistic effects, on the *f*-electron materials is also one of our goals.

Acknowledgments

Throughout my study on physics of *f*-electron materials, I have been guided, supported and encouraged by my supervisor Professor Akira Hasegawa. I would like to express my sincerest gratitude to him for his excellent and patient tutorship.

I also wish to thank Professor M. Goda, who has given advice and criticism on the effect of general relativity on the electron motion in atoms shown in Appendix D. I am also grateful to Dr. Y. Tanaka for a number of illuminative discussions and encouragements throughout this course.

I am indebted to Professor Y. Onuki, Osaka University, for a permission of use of the experimental data for the de Haas-van Alphen effect prior to publication. I also would like to acknowledge Dr. H. Yamagami, Tohoku University, for valuable discussions of band theory and strong encouragements.

Lastly I want to thank all members of the condensed matter theory group of Niigata University for helping to create a nice academic atmosphere.

Numerical calculations were performed at Niigata University Information Processing Center and Tohoku University Computer Center.

References

Andersen O K: Phys. Rev. B **12** (1975) 3060.

Arko A J and Koelling D D: Phys. Rev. B **17** (1978) 3104.

Arko A J, Koelling D D and Schirber J E: *Handbook on the Physics and Chemistry of the Actinides*, eds. A. J. Freeman and G. H. Lander (North-Holland, Amsterdam, 1985) Vol. 2, Chap. 3, p. 175.

Baer Y and Lang J K: Phys. Rev. B **21** (1980) 2060.

Balster A, Ihrig H, Kockel A and Methfessel S: Z. Phys. B - Condensed Matter and Quanta **21** (1975) 241.

Berestetski V B, Lifshitz E M and Pitaevski L P: *Quantum Electrodynamics* (Pergamon Press, Oxford, 1980).

Boyle D J and Gold A V: Phys. Rev. Lett. **22** (1969) 461.

Chan S K and Lam D J: *The Actinides: Electronic Structure and Related Properties*, eds. A. J. Freeman and J. B. Darby (Academic Press, New York, 1974) Vol. 1, p. 1.

Chapman S, Hunt M, Meeson P, Reinders P H P, Springford M and Norman M R: J. Phys.: Condens. Matter **2** (1990) 8123.

Cracknell A P, Davies B L, Miller S C and Love W F: *Kronecker Product Table* (IFI/Plenum, New York, 1979) Vol. 1, p. 30.

Desclaux J P and Freeman A J: *Handbook on the Physics and Chemistry of Actinides,* eds. A. J. Freeman and G. H. Lander (North-Holland, Amsterdam, 1984) Vol. 1, Chap. 1.

Dimmock J O: *Solid State Physics*, ed. Ehrenreich H, Seitz F and Turnbull D (Academic Press, New York, 1971) Vol. 26, p. 103.

Dongarra J J, Gabriel J R, Koelling D D and Wilkinson J H: J. Comput. Phys. **54** (1984) 278.

Eriksson O: Doctor Thesis (Uppsala Univ., 1989).

Ewald P P: Ann. Physik **64** (1921) 253.

Freeman A J and Koelling D D: *The Actinides: Electronic Structure and Related Properties*, eds. A. J. Freeman and J. B. Darby (Academic Press, New York, 1974) Vol. 1, p. 54.

Gordon J E, Montgomery H, Noer R J, Pichett G R and Torbon R: Phys. Rev. **152** (1966) 432.

Greiner J D and Smith J F: Phys. Rev. B **4** (1971) 3275.

Gunnarsson O and Lundqvist B I: Phys. Rev. B **13** (1976) 4274.

Guo G Y: Physica B **165&166** (1990) 335.

Gupta R P and Loucks T L: Phys. Rev. Lett. **22** (1969) 458, Phys. Rev. B **3** (1971) 1834.

Harrus A, Mihalisin T and Kemly E: J. Mag. & Magn. Mater. **47&48** (1983) 5347.

Hasegawa A: J. Phys. Soc. Jpn. **53** (1984) 3929.

Hasegawa A: J. Phys. Soc. Jpn. **54** (1985) 677.

Hasegawa A: Jpn. J. Appl. Phys. Series 8 (1993) 162.

Hasegawa A, Bremicker B and Kubler J: Z. Phys. B - Condensed Matter and Quanta **22** (1975) 231.

Hasegawa A, Yamagami H and Johbettoh H: J. Phys. Soc. Jpn. **59** (1990) 2457.

Hasegawa A and Yamagami H: J. Phys. Soc. Jpn. **59** (1990) 218.

Hasegawa A and Yamagami H: J. Phys. Soc. Jpn. **60** (1991) 1654.

Hasegawa A and Yamagami H: Prog. Theor. Phys. Suppl. **27** (1992) 108.

Hasegawa A, Yamagami H and Asano S: Physica B **186-188** (1993) 159.

Hayden S M, Taillefer L, Vettier C and Flouquet J: Phys. Rev. B **46** (1992) 8675.

Herman F and Skillman S: *Atomic Structure Calculations* (Prentice-Hall, Englewood Cliff, New Jersey, 1963).

Higuchi M and Hasegawa A: to appear in J. Phys. Soc. Jpn. **64** No.3 (1995a).

Higuchi M and Hasegawa A: submitted to Z. Phys. B - Condensed Matter (1995b).

Higuchi M, Yamagami H and Hasegawa A: J. Phys. Soc. Jpn. **63** (1994a) 3014.

Higuchi M, Yamagami H and Hasegawa A: J. Phys. Soc. Jpn. **63** (1994b) 4463.

Ihrig H, Vigren D T, Kubler J and Methfessel S: Phys. Rev. B **8** (1973) 4525.

Inada Y, Aono H, Ishiguro A, Kimura J, Sato N, Sawada A and Komatsubara T: Physica B **119&200** (1994) 119.

Jepson O and Anderson O K: Solid State Commun. **9** (1971) 1763.

Kasuya T, Sakai O, Tanaka J, Kitazawa H and Suzuki T: J. Magn. Magn. Mater. **65&66** (1987) 6.

Kitazawa H, Suzuki T, Sera M, Oguro I, Yanase A, Hasegawa A and Kasuya T: J. Magn. Magn. Mater. **31-34** (1983) 421.

Klaasse J C P, Mattens W C M, de Boer F R and de Chatel P F: Physica B **86-88** (1977) 234.

Koelling D D and Arbman G O: J. Phys. F **5** (1975) 2041.

Koelling D D and Freeman A J: Phys. Rev. B **12** (1975) 5622.

Koelling D D and Harmon B H: J. Phys. C **10** (1977) 3107.

Kohn W and Sham L J: Phys. Rev. **94** (1965) 1111.

Komatsubara T, Sato N, Kunii S, Oguro I, Furukawa Y, Onuki Y and Kasuya T: J. Magn. Magn. Mater. **31-34** (1983) 368.

Lee P A, Rice T M, Serene J W, Sham L J and Wilkins J W: Comments on Cond. Matter Phys. **12** (1986) 99.

Lewis W B, Mann J B, Liberman D A and Cromer D T: J. Chem. Phys. **53** (1970) 89.

Liberman D, Waber J T and Cromer D T: Phys. Rev. **137** (1965) A27.

Lonzarich G G: J. Magn. Magn. Mater. **76&77** (1988) 1.

Loucks T L: *Augmented Plane Wave Method* (Benjamin, New York, 1967).

MacDonald A H, Pickett W E and Koelling D D: J. Phys. C **13** (1980) 2675.

Maesawa M, Kato T, Ishikawa Y, Sato K, Umehara I, Kurosawa Y and Onuki Y: J. Phys. Soc. Jpn. **58** (1989) 4098.

Mann J B: Los Alamos Report LA (1968) 3690.

Maple M B, DeLong L E and Sales B C: *Handbook on the Physics and Chemistry of Rare Earths*, ed. K. A. Gschneidner Jr., L. Eyring, G. (North-Holland, Amsterdam, 1978) Vol. 1, Chap. 11, p. 797.

Marcus P M: Int. J. Quant. Chem. **1S** (1967) 567.

Mattheiss L F, Wood J H and Switendick A C: *Methods in Computational Physics*, ed. B. Alder, S. Fernbach and M. Rotenberg (Academic Press, New York, 1968) Vol. 8, p. 63.

Mayers D F: Proc. Roy. Soc. (London) A **241** (1957) 93.

Motoki K, Settai R, Ebihara T, Kimura N, Ikezawa H, Toshima H, Sugawara H and Onuki Y: to be published in J. Phys. Soc. Jpn.

Niksch M, Luthi B, Assmus W and Kubler J: J. Magn. Magn. Mater. **28** (1982) 243.

Niksch M, Luthi B and Kubler J: Z. Phys. B - Condensed Matter **68** (1987) 291.

Norman M R and Koelling D D: *Handbook on the Physics and Chemistry of Rare Earths*, ed. K. A. Gschneidner Jr., L. Eyring, G. H. Lander and G. R. Choppin (North-Holland, Amsterdam, 1993) Vol. 17, Chap. 110, p. 1.

Onuki Y and Hasegawa A: to appear in *Handbook on the Physics and Chemistry of Rare Earths*, ed. K. A. Gschneidner Jr. and L. Eyring (North-Holland, Amsterdam, 1995) Vol. 20, Chap. 135.

Onuki Y, Kurosawa M, Maezawa M, Umehara I, Ishikawa Y and Sato K: J. Phys. Soc. Jpn. **58** (1989) 3705.

Onuki Y, Umehara I, Albessard A K, Ebihara T and Satoh K: J. Phys. Soc. Jpn. **61** (1992) 960.

Onuki Y, Umehara I, Kurosawa Y, Satoh K and Matsui H: J. Phys. Soc. Jpn. **59** (1990a) 229.

Onuki Y, Umehara I, Kurosawa Y, Nagai N, Satoh K, Kasaya M and Iga F: J. Phys. Soc. Jpn. **59** (1990b) 2320.

Rath J and Freeman A J: Phys. Rev. B **11** (1975) 2109.

Rose M E: *Relativistic Electron Theory* (John Wiley, New York, 1961).

Sandstrom A E: *Encyclopedia of Physics,* ed. S. Flugge (Springer-Verlag, Berlin, 1957) Vol.30.

Satoh K, Yun S W, Umehara I, Onuki Y, Uji S, Shimizu T and Aoki H: J. Phys. Soc. Jpn. **61** (1992) 1829.

Schirber J E, Schmidt F A and Koelling D D: Phys. Rev. B **16** (1977) 4235.

Seipler D, Bremicker B, Goebel U, Happel H, Hoenig H E and Perrin B: J. Phys. F: Metal Phys. **7** (1977) 599.

Settai R, Goto T, Sakatsume S, Kwon Y S, Suzuki T and Kasuya T: Physca B **186-188** (1993) 176.

Shoenberg D: *Magnetic Oscillations in Metals* (Cambridge University Press, Cambridge, 1984) Chap. 2.

Skriver H L and Jan J P: Phys. Rev. B **21** (1980) 1489.

Slater J C: Phys. Rev. **51** (1937) 846.

Sugawara H, Nagai N, Albessard K A, Yamazaki T, Itoh J, Satoh K and Onuki Y: Physica B **186-188** (1993) 162.

Sugawara H, Yamazaki T, Itoh J, Takashita M, Ebihara T, Kimura N, Svoboda P, Settai R, Onuki Y,Sata H, Uji S and Aoki H: J. Phys. Soc. Jpn. **63** (1994) 1502.

Sugawara H, Motoki K, Yamazaki T, Ebihara T, Kimura N, Takashita M, Itoh J, Toshima H, Settai R and Onuki Y: to be published in J. Phys. Soc. Jpn. (1995).

Takeda T: Z. Phys. B - Condensed Matter **32** (1978) 43.

Takeda T: J. Phys. F: Metal Phys. **9** (1979) 815.

Takeda T and Kubler J: J. Phys. F: Metal Phys. **9** (1979) 661.

Tannous C, Ray D K and Belakhovsky M: J. Phys. F: Metal Phys. **6** (1976) 2091.

Thorsen A C, Joseph A S andValby L E: Phys. Rev. **162** (1967) 574.

Umehara I, Kurosawa Y, Nagai N, Kikuchi M, Satoh K and Onuki Y: J. Phys. Soc. Jpn. **59** (1990a) 2848.

Umehara I, Nagai N and Onuki Y: J. Phys. Soc. Jpn. **60** (1991) 1464.

Umehara I, Nagai N and Onuki Y: J. Phys. Soc. Jpn. **60** (1990b) 1294.

van Hove L: Phys. Rev. **89** (1953) 1189.

Villars P and Calvert L T: *Pearson's Handbook of Crystallographic Data for Intermetallic Phases* (American Society for Metal, 1986) Vols. 1, 2 and 3.

von Barth U and Hedin L: J. Phys. C **5** (1972) 1629.

Williams Jr. A O: Phys. Rev. **58** (1940) 723.

Yamagami H: Doctor Thesis (Niigata Univ., 1991).

Yamagami H and Hasegawa A: J. Phys. Soc. Jpn. **59** (1990) 2426.

Yamagami H and Hasegawa A: J. Phys. Soc. Jpn. **60** (1991a) 987.

Yamagami H and Hasegawa A: J. Phys. Soc. Jpn. **60** (1991b) 1011.

Yamagami H and Hasegawa A: J. Phys. Soc. Jpn. **61** (1992) 2388.

Yamagami H and Hasegawa A: J. Phys. Soc. Jpn. **62** (1993a) 592.

Yamagami H and Hasegawa A: Physica B **186-188** (1993b) 136.

Yamagami H, Yasutami Takada, Yasuhara H and Hasegawa A: Phys. Rev. A **49** (1994) 2354.

Yamazaki T, Motoki K, Sugawara H, Ebihara T, Kimura N, Takashita M, Itoh J, Toshima H, Ikezawa H, Settai R and Onuki Y: to appear in J. Magn. Magn. Mater. **140-144** (1995).

Yanase A: J. Phys. F: Metal Phys. **16** (1986) 1501.

Yanase A and Harima H: Prog. Theor. Phys. Suppl. No. 108 (1992) 19.

Zwicknagl G: Adv. Phys. **41** (1992) 203.

Proceedings and Reviews

Proceedings of the Yamada Conference XXV on Magnetic Phase Transitions, ed. M. Date, K. Nagata, Y. Miyako and K. Komatsubara (Elsevier Science Publishers B. V. and Yamada Science Foundation, 1990) [J. Magn. Magn. Mater. **90&91** (1990)].

Proceedings of the International Conference on Strongly Correlated Electron Systems, ed. T. Kasuya, A. Yanase and K. Okuda (North-Holland, Amsterdam, 1993) [Physica B **186-188** (1993)].

Onuki Y and Hasegawa A: *The Fermi Surface of Heavy-Electron Systems* in: *Nihon Butsuri Gakkaisi* **46** (1991) 571 [in Japanese].

Onuki Y, Ueda K and Komatubara T: *on Heavy-Electron System*: *Buturigaku Ronbunsensyu IV* (Nihon Butsuri Gakkai, 1994) [in Japanese].

Appendix A : A Proof of the Correspondance between the Matrix Elements in RLAPW and those in LAPW in the Nonrelativistic Limit

Here is the proof that the matix elements in the RLAPW method are reduced to those in the LAPW method in the nonrelativistic limit $c \to \infty$, where c is the velocity of light. For simplicity we assume the average potential V_0 to be zero and consider a monoatomic metal. The matrix elements in the LAPW method are given by Takeda and Kubler (1979) :

$$\begin{aligned}
&\left\{H_{\nu\mu} - EO_{\nu\mu}\right\}_{\mathrm{LAPW}} \\
&= \left(k_\nu^2 - E\right)\Omega\delta_{\nu\mu} - \left(\frac{k_\nu^2 + k_\mu^2}{2} - E\right) I_{\nu\mu} \\
&+ \sum_l 4\pi(2l+1) P_l(\cos\theta_{\nu\mu}) \Bigg\{ \sum_{\alpha=1,2} \varepsilon_{l\alpha} a_{l\nu\alpha} a_{l\mu\alpha} \Phi_{l\alpha\alpha} \\
&+ \frac{1}{2} \sum_{<\alpha,\beta>} \left(\varepsilon_{l\alpha} + \varepsilon_{l\beta}\right)\left(a_{l\nu\alpha} a_{l\mu\beta} + a_{l\nu\beta} a_{l\mu\alpha}\right) \Phi_{l\alpha\beta} \\
&- E \sum_{\alpha,\beta=1,2} a_{l\nu\alpha} a_{l\mu\beta} \Phi_{l\alpha\beta} \Bigg\},
\end{aligned} \tag{A.1}$$

where $\varepsilon_{l\alpha}(\alpha = 1,2)$ are chosen appropriately for each value of l and the summing of the term which involves $\left(\varepsilon_{l\alpha} + \varepsilon_{l\beta}\right)$ in eq. (A.1) is taken over all possible pairs $< \alpha\beta >$ except for $< \alpha\alpha >$. In eq. (A.1), $a_{l\mu\alpha}$ and $\Phi_{l\alpha\beta}$ are defined as

$$\begin{pmatrix} a_{l\mu 1} \\ a_{l\mu 2} \end{pmatrix} = \frac{1}{\phi_{l1}(s)\phi'_{l2}(s) - \phi_{l2}(s)\phi'_{l1}(s)} \begin{pmatrix} \phi'_{l2}(s) & -\phi_{l2}(s) \\ -\phi'_{l1}(s) & \phi_{l1}(s) \end{pmatrix} \begin{pmatrix} j_l(k_\mu s) \\ k_\mu j'_l(k_\mu s) \end{pmatrix}, \tag{A.2}$$

and

$$\Phi_{l\alpha\beta} = \begin{cases} 1 & \text{for } \alpha = \beta \\ s^2 \dfrac{\phi_{l\alpha}(s)\phi'_{l\beta}(s) - \phi'_{l\alpha}(s)\phi_{l\beta}(s)}{\varepsilon_{l\alpha} - \varepsilon_{l\beta}} & \text{for } \alpha \neq \beta, \end{cases} \tag{A.3}$$

where $\phi_{l\alpha}(r)$ is a solution of the radial Schrodinger equation with its eigenvalue of $\varepsilon_{l\alpha}$, and s means the radius of the Muffin-tin sphere. The other notations used in eqs. (A.1), (A.2) and (A.3) are the same as Takeda and Kubler (1979) and the reader is referred to that.

First we will verify that $\xi_{\kappa\alpha\beta}$ coincides with $\Phi_{l\alpha\beta}$ in the limit $c \to \infty$. Let $c \to \infty$, then the term $c f_{\kappa\alpha}/g_{\kappa\alpha}$ contained in $\xi_{\kappa\alpha\beta}$ becomes

$$c\frac{f_{\kappa\alpha}}{g_{\kappa\alpha}} \xrightarrow{c\to\infty} \begin{cases} \dfrac{\phi'_{l\alpha}}{\phi_{l\alpha}} + \dfrac{\kappa+1}{s} & \text{for } \kappa > 0 \\ -\left(\dfrac{\phi'_{l\alpha}}{\phi_{l\alpha}} + \dfrac{\kappa+1}{s}\right) & \text{for } \kappa > 0. \end{cases} \tag{A.4}$$

Hence the term $\xi_{\kappa\alpha\beta}$ is simplified and can be written as

(i) $\kappa > 0$

$$\xi_{l\alpha\beta} = g_{l\alpha} g_{l\beta} s^2 \frac{c\dfrac{f_{l\beta}}{g_{l\beta}} - c\dfrac{f_{l\alpha}}{g_{l\alpha}}}{\varepsilon_{l\alpha} - \varepsilon_{l\beta}}$$

$$\xrightarrow{c\to\infty} \phi_{l\alpha}\phi_{l\beta} s^2 \frac{\dfrac{\phi'_{l\beta}}{\phi_{l\beta}} + \dfrac{\kappa+1}{s} - \dfrac{\phi'_{l\alpha}}{\phi_{l\alpha}} - \dfrac{\kappa+1}{s}}{\varepsilon_{l\alpha} - \varepsilon_{l\beta}}$$

$$= s^2 \frac{\phi_{l\alpha}\phi'_{l\beta} - \phi'_{l\alpha}\phi_{l\beta}}{\varepsilon_{l\alpha} - \varepsilon_{l\beta}}$$

$$= \Phi_{l\alpha\beta},$$

(ii) $\kappa < 0$

$$\xi_{-l-1,\alpha\beta} = -g_{-l-1,\alpha} g_{-l-1,\beta} S^2 \frac{c\dfrac{f_{-l-1,\beta}}{g_{-l-1,\beta}} - c\dfrac{f_{-l-1,\alpha}}{g_{-l-1,\alpha}}}{\varepsilon_{-l-1,\alpha} - \varepsilon_{-l-1,\beta}}$$

$$\xrightarrow{c\to\infty} -\phi_{l\alpha}\phi_{l\beta} S^2 \frac{-\dfrac{\phi'_{l\beta}}{\phi_{l\beta}} - \dfrac{\kappa+1}{s} + \dfrac{\phi'_{l\alpha}}{\phi_{l\alpha}} + \dfrac{\kappa+1}{s}}{\varepsilon_{l\alpha} - \varepsilon_{l\beta}}$$

$$= s^2 \frac{\phi_{l\alpha}\phi'_{l\beta} - \phi'_{l\alpha}\phi_{l\beta}}{\varepsilon_{l\alpha} - \varepsilon_{l\beta}}$$

$$= \Phi_{l\alpha\beta}.$$

Irrespective of the sign of κ, we have

$$\xi_{\kappa\alpha\alpha} = 1 = \Phi_{l\alpha\alpha}.$$

Accordingly it can be shown that

$$\xi_{\kappa\alpha\beta} \xrightarrow{c\to\infty} \Phi_{l\alpha\beta}. \tag{A.5}$$

Similarily the expansion coefficients $a_{\kappa\alpha\beta}$ in the RLAPW method can be simplified to those in the LAPW method in the nonrelativistic limit. Using the eq.(A.4), we see that

(i) $\kappa > 0$

$$\begin{pmatrix} a_{l\mu 1} \\ a_{l\mu 2} \end{pmatrix} = \frac{1}{g_{l1}g_{l2}} \frac{c}{\left(\dfrac{cf_{l2}}{g_{l2}}\right) - \left(\dfrac{cf_{l1}}{g_{l1}}\right)} \begin{pmatrix} f_{l2}j_l - \gamma g_{l2} k_\mu j_{l-1} \\ -f_{l1}j_l + \gamma g_{l1} k_\mu j_{l-1} \end{pmatrix}$$

$$\xrightarrow{c\to\infty} \frac{1}{\phi_{l1}\phi_{l2}} \frac{1/\gamma}{\dfrac{\phi'_{l2}}{\phi_{l2}} + \dfrac{l+1}{s} - \dfrac{\phi'_{l1}}{\phi_{l1}} - \dfrac{l+1}{s}} \begin{pmatrix} \gamma\phi'_{l2} j_l - \gamma\phi_{l2} k_\mu j'_l \\ -\gamma\phi'_{l1} j_l - \gamma\phi_{l1} k_\mu j'_l \end{pmatrix}$$

$$= \frac{1}{\phi_{l1}\phi'_{l2} - \phi'_{l1}\phi_{l2}} \begin{pmatrix} \phi'_{l2} & -\phi_{l2} \\ -\phi'_{l1} & \phi_{l1} \end{pmatrix} \begin{pmatrix} j_l \\ k_\mu j'_l \end{pmatrix},$$

(A.6)

(ii) $\kappa < 0$

$$\begin{pmatrix} a_{-l-1,\mu 1} \\ a_{-l-1,\mu 2} \end{pmatrix} = \frac{1}{g_{-l-1,1} g_{-l-1,2}} \frac{c}{\left(\frac{cf_{-l-1,2}}{g_{-l-1,2}}\right) - \left(\frac{cf_{-l-1,1}}{g_{-l-1,1}}\right)} \times \begin{pmatrix} f_{-l-1,2} j_l - \gamma g_{-l-1,2} k_\mu j_{l+1} \\ -f_{-l-1,1} j_l + \gamma g_{-l-1,1} k_\mu j_{l+1} \end{pmatrix}$$

$$\xrightarrow{c\to\infty} \frac{1}{\phi_{l1}\phi_{l2}} \frac{-1/\gamma}{\frac{\phi'_{l2}}{\phi_{l2}} - \frac{l}{s} - \frac{\phi'_{l1}}{\phi_{l1}} + \frac{l}{s}} \begin{pmatrix} -\gamma\phi'_{l2} j_l + \gamma\phi_{l2} k_\mu j'_l \\ \gamma\phi'_{l1} j_l - \gamma\phi_{l1} k_\mu j'_l \end{pmatrix}$$

$$= \frac{1}{\phi_{l1}\phi'_{l2} - \phi'_{l1}\phi_{l2}} \begin{pmatrix} \phi'_{l2} & -\phi_{l2} \\ -\phi'_{l1} & \phi_{l1} \end{pmatrix} \begin{pmatrix} j_l \\ k_\mu j'_l \end{pmatrix}. \tag{A.7}$$

Substituting (A.2) into (A.6) and (A.7), we find that the expansion coefficients $a_{\kappa\alpha\beta}$ in the RLAPW method correspond to those in the LAPW method in the limit $c \to \infty$.

The matrix elements in the RLAPW are repeated here :

$$\begin{aligned}
&\left\{H_{\nu\mu}^{mm'} - EO_{\nu\mu}^{mm'}\right\}_{\text{RLAPW}} \\
&= \left\{\left(\varepsilon_\mu - E\right)\Omega\delta_{\nu\mu} - \left(\frac{\varepsilon_\nu + \varepsilon_\mu}{2} - E\right) I_{\nu\mu}\right\}\delta_{mm'} \\
&+ \sum_l \Big[4\pi \left\{ l P_l(\cos\theta_{\nu\mu})\delta_{mm'} + i(\hat{k}_\nu \times \hat{k}_\nu)\cdot\langle m|\sigma|m'\rangle P'_l(\cos\theta_{\nu\mu})\right\} \\
&\quad \times \sum_{\alpha,\beta=1,2} \left(\frac{\varepsilon_{l\alpha} + \varepsilon_{l\beta}}{2} - E\right) a_{l\nu\alpha} a_{l\mu\beta} \xi_{l\alpha\beta} \\
&\quad + 4\pi \left\{ (l+1) P_l(\cos\theta_{\nu\mu})\delta_{mm'} - i(\hat{k}_\nu \times \hat{k}_\nu)\cdot\langle m|\sigma|m'\rangle P'_l(\cos\theta_{\nu\mu})\right\} \\
&\quad \times \sum_{\alpha,\beta=1,2} \left(\frac{\varepsilon_{-l-1,\alpha} + \varepsilon_{-l-1,\beta}}{2} - E\right) a_{-l-1,\nu\alpha} a_{-l-1,\mu\beta} \xi_{-l-1,\alpha\beta} \Big].
\end{aligned} \tag{A.8}$$

Substituting (A.5), (A.6) and (A.7) into (A.8) yields the expression in the nonrelativistic limit as follows :

$$
\begin{aligned}
&\left\{H_{\nu\mu}^{mm'} - EO_{\nu\mu}^{mm'}\right\}_{\mathrm{RLAPW}} \\
&\xrightarrow{c\to\infty} = \left\{\left(k_\mu^2 - E\right)\Omega\delta_{\nu\mu} - \left(\frac{k_\nu^2 + k_\mu^2}{2} - E\right)I_{\nu\mu}\right\}\delta_{mm'} \\
&\quad + \sum_l 4\pi(2l+1)P_l(\cos\theta_{\nu\mu}) \\
&\quad \times \sum_{\alpha,\beta=1,2}\left(\frac{\varepsilon_{l\alpha} + \varepsilon_{l\beta}}{2} - E\right)a_{l\nu\alpha}a_{l\mu\beta}\Phi_{l\alpha\beta}\delta_{mm'} \\
&\quad = \left\{\left(k_\mu^2 - E\right)\Omega\delta_{\nu\mu} - \left(\frac{k_\nu^2 + k_\mu^2}{2} - E\right)I_{\nu\mu}\right\}\delta_{mm'} \\
&\quad + \sum_l 4\pi(2l+1)P_l(\cos\theta_{\nu\mu})\left\{\sum_{\alpha,\beta=1,2}\varepsilon_{l\alpha}a_{l\nu\alpha}a_{l\mu\alpha}\Phi_{l\alpha\alpha}\right. \\
&\qquad\qquad + \frac{1}{2}\sum_{<\alpha,\beta>}\left(\varepsilon_{l\alpha} + \varepsilon_{l\beta}\right)\left(a_{l\nu\alpha}a_{l\mu\beta} + a_{l\nu\beta}a_{l\mu\alpha}\right)\Phi_{l\alpha\beta} \\
&\qquad\qquad \left. - E\sum_{\alpha,\beta=1,2}a_{l\nu\alpha}a_{l\mu\beta}\Phi_{l\alpha\beta}\right\}\delta_{mm'} \\
&\quad = \left\{H_{\nu\mu} - EO_{\nu\mu}\right\}_{\mathrm{LAPW}}\delta_{mm'}.
\end{aligned}
\tag{A.9}
$$

Here we assume that the energies $\varepsilon_{l\alpha}$ and $\varepsilon_{-l-1,\alpha}$ in the RLAPW method coincide with those in the LAPW method, i.e. both of the energies $\varepsilon_{l\alpha}$ and $\varepsilon_{-l-1,\alpha}$ given beforehand in the RLAPW method accord with the energy $\varepsilon_{l\alpha}$ in the LAPW method in the nonrelativistic limit.

Therefore it has been proven that the matrix elements in the RLAPW method are reduced to those in the LAPW method in the nonrelativistic limit $c \to \infty$.

Appendix B : Expressions for the Norm and the Charge Distributions

In order to evaluate the norm of the variation function $\Phi_{\boldsymbol{k},n}(\boldsymbol{s})$ in eq.(3.13), we integrate $\Phi_{\boldsymbol{k},n}(\boldsymbol{s})^{+}\Phi_{\boldsymbol{k},n}(\boldsymbol{s})\mathrm{d}\tau$ over a primitive cell of the crystal and require that this integral equal unity :

$$\int_{\text{cell}} \Phi_{\boldsymbol{k},n}(\boldsymbol{s})^{+}\Phi_{\boldsymbol{k},n}(\boldsymbol{s})\mathrm{d}\tau = 1, \tag{B.1}$$

where the suffix n represents the band index. As the result, the norm $N_{\boldsymbol{k},n}$ of the wave function $\Phi_{\boldsymbol{k},n}(\boldsymbol{s})$ of the state in the nth band at $\boldsymbol{k}$ is calculated as

$$\begin{aligned}
N_{\boldsymbol{k},n} &= \sum_{\nu,\mu=1}^{W_{\boldsymbol{k}}} \sum_{m,m'=\pm\frac{1}{2}} C_{\nu}^{m^{*}} C_{\mu}^{m'} \left\{ \int_{\text{outside}} \psi_{\nu}^{m}(\boldsymbol{s})^{+}\psi_{\mu}^{m'}(\boldsymbol{s})\mathrm{d}\tau \right. \\
&\quad \left. + \sum_{i=1}^{N_t} \int_{i\text{th sphere}} \tilde{\psi}_{\nu}^{m,i}(\boldsymbol{s})^{+}\tilde{\psi}_{\mu}^{m',i}(\boldsymbol{s})\mathrm{d}\tau \right\} \\
&= \Omega \sum_{\nu,\mu=1}^{W_{\boldsymbol{k}}} \sum_{m,m'=\pm\frac{1}{2}} C_{\nu}^{m^{*}} C_{\mu}^{m'} O_{\nu\mu}^{mm'} \\
&= \sum_{\nu,\mu=1}^{W_{\boldsymbol{k}}} \sum_{m,m'=\pm\frac{1}{2}} C_{\nu}^{m^{*}} C_{\mu}^{m'} \left[\left(\Omega\delta_{\nu\mu} - A_{\nu\mu} \right)\delta_{mm'} \right. \\
&\quad + \sum_{l=0}^{l_{\max}} \sum_{\alpha,\beta=1,2} \sum_{p=1}^{P} \left\{ \xi_{l\alpha\beta}^{p} B_{\nu\mu,\alpha\beta}^{l,p} + \xi_{-l-1,\alpha\beta}^{p} C_{\nu\mu,\alpha\beta}^{l,p} \right\}\delta_{mm'} \\
&\quad \left. + \sum_{l=0}^{l_{\max}} \sum_{\alpha,\beta=1,2} \sum_{p=1}^{P} \left\{ \xi_{l\alpha\beta}^{p} F_{\nu\mu,\alpha\beta}^{l,p}(m,m') - \xi_{-l-1,\alpha\beta}^{p} G_{\nu\mu,\alpha\beta}^{l,p}(m,m') \right\} \right] ,
\end{aligned} \tag{B.2}$$

From this norm we derive separately the probabilities of finding an electron with $\boldsymbol{k}$ in the nth band inside and outside the APW spheres. If we rewrite eq. (B.2) in the following form :

$$Q_{\text{out}}^{\boldsymbol{k},n} + \sum_{l=0}^{l_{\max}} \sum_{p=1}^{P} N_p Q_{pl}^{\boldsymbol{k},n} = 1, \tag{B.3}$$

then $Q_{\text{out}}^{\boldsymbol{k},n}$ means the fraction of electronic charge outside the APW spheres and $Q_{pl}^{\boldsymbol{k},n}$ means the fractional charge partitioned according to the angular momentum l in one of the pth-type APW spheres. They are given by

$$Q_{\text{out}}^{\boldsymbol{k},n} = \frac{1}{N_{\boldsymbol{k},n}} \sum_{\nu,\mu=1}^{W_{\boldsymbol{k}}} \sum_{m=\pm\frac{1}{2}} C_\nu^{m\,*} C_\mu^m \left(\Omega\delta_{\nu\mu} - A_{\nu\mu}\right), \tag{B.4}$$

and

$$Q_{pl}^{\boldsymbol{k},n} = \frac{1}{N_p N_{\boldsymbol{k},n}} \sum_{\nu,\mu=1}^{W_{\boldsymbol{k}}} \sum_{\alpha,\beta=1,2} \sum_{m,m'=\pm\frac{1}{2}} C_\nu^{m\,*} C_\mu^{m'} \left\{ \left(\xi_{l\alpha\beta}^{p} B_{\nu\mu,\alpha\beta}^{l,p} + \xi_{-l-1,\alpha\beta}^{p} C_{\nu\mu,\alpha\beta}^{l,p} \right) \delta_{mm'} \right.$$
$$\left. + \xi_{l\alpha\beta}^{p} F_{\nu\mu,\alpha\beta}^{l,p}(m,m') - \xi_{-l-1,\alpha\beta}^{p} G_{\nu\mu,\alpha\beta}^{l,p}(m,m') \right\}. \tag{B.5}$$

The number of the valence electrons in each APW sphere, which is partitioned into the angular momenta, and the number of the valence electrons in the interstitial region are given by the sums of $Q_{pl}^{\boldsymbol{k},n}$ and $Q_{\text{out}}^{\boldsymbol{k},n}$, respectively, over the occupied states with the weighting factor $\lambda_{\boldsymbol{k}}$ defined in the section 3.2.3. We get

$$n_{\text{out}} = \sum_{\substack{n \\ (E_{\boldsymbol{k},n} \le E_{\text{F}})}} \sum_{\boldsymbol{k}} \lambda_{\boldsymbol{k}} Q_{\text{out}}^{\boldsymbol{k},n}\ , \tag{B.6}$$

and

$$n_{p,l} = \sum_{\substack{n \\ (E_{k,n} \le E_F)}} \sum_{k} \lambda_k Q_{pl}^{k,n} \ . \tag{B.7}$$

The sum of n_{out} and all $n_{p,l}$ is equal to the total number of valence electrons in the primitive cell, N_e, i.e.

$$n_{\text{out}} + \sum_{p=1}^{P} N_p \sum_{l=0}^{l_{\max}} n_{p,l} = N_e. \tag{B.8}$$

Appendix C : Expressions for the Muffin-Tin Potentials

Here are the explicit expressions for the one-electron potential energy functions. By using Mattheiss' method (Mattheiss *et al.* 1968 ; Ewald 1921), the Coulomb potential inside the pth sphere, $V_{\mathrm{c,in}}^{p}(r)$, and the average Coulomb potential outside the spheres, $\overline{V}_{\mathrm{c,out}}$, are respectively given by

$$V_{\mathrm{c,in}}^{p}(r) = -\frac{2Z_p}{r} + \frac{2}{r}\int_0^r \sigma_p(r')\mathrm{d}r' + 2\int_r^{S_p} \frac{\sigma_p(r')}{r'}\mathrm{d}r' + C_p, \tag{C.1}$$

and

$$\overline{V}_{\mathrm{c,out}} = \sum_{p=1}^{P} Q_p \overline{\phi}_p, \tag{C.2}$$

where

$$Q_p = Z_p - \int_0^{S_p} \sigma_p(r)\mathrm{d}r + \frac{4\pi}{3} {S_p}^3 \overline{\rho}, \tag{C.3}$$

$$\overline{\phi}_p = \frac{4\pi N_p {S_p}^2 + \frac{4\pi}{3}\sum_{q=1}^{P}\left\{\frac{4\pi}{5}\frac{N_p}{\Omega}{S_q}^5 + U_{\mathrm{M}}(q,p){S_q}^3\right\}N_q}{\Omega - \frac{4\pi}{3}\sum_{q=1}^{P} N_q {S_q}^3}, \tag{C.4}$$

$$C_p = 2\frac{Z_p - Q_p}{S_p} - \sum_{q=1}^{P}\left\{\frac{4\pi}{3\Omega}N_q {S_p}^2 + U_{\mathrm{M}}(p,q)\right\}Q_q - \frac{2}{S_p}\int_0^{S_p}\sigma_p(r')\mathrm{d}r', \tag{C.5}$$

where Z_p is the atomic number of the pth-type atom, and $\sigma_p(r)$ and $\overline{\rho}$ are the muffin-tin charge density defined in section 3.2.3. The constant $U_{\mathrm{M}}(p,q)$ means the Madelung potential at the position of the pth-type atom in the sub-lattice which consists of qth-type atom. Q_p is the fictitious

charge, and $\overline{\phi}_p$ represent the average Coulomb potential for the unit charge. C_p is determined by the exterior charge distribution.

The exchange and correlation potentials are taken into account by the density functional theory in a local-density approximation, and use the non-relativistic formula of Gunnarson and Lundqvist (1976) throughout in this thesis because the relativistic effects on the exchange and correlation potentials are found to be small in an actual atom (Yamagami and Hasegawa 1990).

Appendix D : Classical estimate of effects of general relativity in atoms

A gravitational field is characterized by the metric which corresponds to the square of the element of spatial distance in the Riemann space. Using the metric, the action integral that means the distance between two world points in the Riemann space is defined as

$$I = \int ds, \tag{D.1}$$

where ds is the element of spatial distance and the metric is given by ds^2. From the principle of the least action, I has a minimum value for the actual motion, so that its variation δI is zero. This means that the actual motion of a point particle should be realized along the path having the smallest distance in the Riemann space, i.e. a point particle moves along the geodesic line. The equation of motion for a point particle can be obtained from the condition $\delta I = 0$, and it is just the Euler equation.

The metric is formed by the metric tensors which are given by solving the Einstein equation. Once the solution of the Einstein equation is found, in other words, the properties of the space-time are defined, the motion of a point particle can be derived in the above-mentioned way. In the following discussions, we consider the motion of a point particle under two special conditions, which are denoted as case [I] and case [II]. Throughout this appendix, c is the velocity of light, and G is the gravitational constant.

[I] *The centrally symmetric gravitational field around the spherical matter possessing mass M*

In this case, the Einstein equation can be solved exactly and its solution is called the Schwarzschild solution. It is given by

$$ds^2 = -\left(1-\frac{a}{r}\right)\left(dx^0\right)^2 + \left(1-\frac{a}{r}\right)^{-1}(dr)^2 + r^2\left\{(d\theta)^2 + \sin^2\theta(d\varphi)^2\right\}, \tag{D.2}$$

where $x^0 = ct$ and the gravitational radius a is defined as

$$a = \frac{2GM}{c^2}. \tag{D.3}$$

The action integral is given by

$$I = -\int\left[-\left(1-\frac{a}{r}\right)\left(\dot{x}^0\right)^2 + \left(1-\frac{a}{r}\right)^{-1}(\dot{r})^2 + r^2\left\{\left(\dot{\theta}\right)^2 + \sin^2\theta(\dot{\varphi})^2\right\}\right]d\tau, \tag{D.4}$$

where a dot denotes differentiation with respect to the proper time τ. The equation of motion for a point particle can be obtained by setting $\delta I = 0$. The trajectory of a point particle is given by

$$r = \frac{l}{1+e\cos(\eta\varphi)}, \tag{D.5}$$

where l and e are the semi latus rectum and the eccentricity, respectively. By using the areal velocity h, l is written as

$$l = \frac{2h^2}{ac^2}. \tag{D.6}$$

In eq.(D.5), η should be regarded as the parameter which represents the effect of general relativity, because the trajectory (D.5) agrees with the result of the Newton mechanics if η equals unity. η has the following form:

$$\eta = \sqrt{1-\frac{3a}{l}} \approx 1-\frac{3a}{2l} = 1-\frac{3a^2c^2}{4h^2}. \tag{D.7}$$

Next, we shall consider the precession of perihelion from eq.(D.5). The perihelion is defined as the point where the relation $\cos(\eta\varphi) = 1$ is satisfied, i.e.

$$\eta\varphi = 0,\ 2\pi,\ 4\pi,\ 6\pi,\ \cdots\cdots. \tag{D.8}$$

The angle difference between adjacent perihelions is

$$\varphi = \frac{2\pi}{\eta} \approx 2\pi\left(1+\frac{3a^2c^2}{4h^2}\right). \tag{D.9}$$

Therefore, the precession of perihelion per revolution is given by

$$\Delta\varphi = 2\pi\frac{3a^2c^2}{4h^2} = \frac{3\pi a}{l}. \tag{D.10}$$

It should be noted that the unit of angles is 1 radan in eqs.(D.9) and (D.10). For instance, let us estimate the precession of perihelion of Mercury. The gravitational radius of the sun, a, is 2.94 km, and the semi latus rectum l and the eccentricity e for the trajectory of Mercury is equal to 5.55×10^7 km and 0.206, respectively. Substituting these values into (D.10), we obtain the result:

$$(\Delta\varphi)_{\text{Mercury}} = 4.99\times10^{-7} \text{ radian / cycle.} \qquad \text{(D.11)}$$

By using the fact that the revolution period of Mercurry is 0.24 year, we get the famous result:

$$(\Delta\varphi)_{\text{Mercury}} = 0.43 \text{ ″/ year} = 43 \text{ ″/ century.} \qquad \text{(D.12)}$$

[II] *The centrally symmetric gravitational field around the spherical matter possessing charge q and mass M*

In this case, the exact solution of the Einstein equation has been found by Reissner and Wyle. It is called the Reissner-Wyle solution, and we get

$$ds^2 = -\left(1-\frac{a}{r}+\frac{Q^2}{r^2}\right)\left(dx^0\right)^2+\left(1-\frac{a}{r}+\frac{Q^2}{r^2}\right)^{-1}(dr)^2+r^2\left\{(d\theta)^2+\sin^2\theta(d\varphi)^2\right\}, \qquad \text{(D.13)}$$

where the gravitational radius a is given by eq.(D.3), and Q^2 is defined as

$$Q^2 = \frac{Gq^2}{4\pi\varepsilon_0 c^4}. \qquad \text{(D.14)}$$

It is easily understood that the term containing Q^2 in eq.(D.13) represents the effect of the Coulomb potential on the gravitational field. We shall renormalize the term containing Q^2 into the gravitational radius a. We define the renormalized gravitational radius a^* as

$$a^* = a\left(1-\frac{Q^2}{ar}\right). \tag{D.15}$$

From (D.15), we find that the critical radius r_c where the gravitational field originating from the Coulomb potential becomes comparable to the gravitational field based on the Newton potential is given by

$$r_c = \frac{Q^2}{a}. \tag{D.16}$$

As will be shown later, r_c is extremely smaller than the nuclear radius for atoms, so that the gravitational field originating from the Coulomb potential is extremely weak at an average radius of the electron orbit in atoms. Thus, we neglect the dependence of this term on r. In order to make a^* independent of r, in eq.(D.15) we shall replace r with $\bar{r}$ which represents an average radius of the orbit. Equation (D.15) is rewritten as

$$a^* \approx a\left(1-\frac{Q^2}{a\bar{r}}\right). \tag{D.17}$$

Using eqs.(D.13), (D.15) and (D.17), the trajectory of a point particle is given by

$$r = \frac{l}{1+e\cos(\eta\varphi)}, \tag{D.18}$$

where l and η are newly defined by

$$l = \frac{2h^2}{a^* c^2}\ , \tag{D.19}$$

$$\eta = \sqrt{1-\frac{3a^*}{l}} \approx 1-\frac{3a^*}{2l} = 1-\frac{3a^{*2}c^2}{4h^2}. \qquad \text{(D.20)}$$

As in case [I], the precession of perihelion per revolution can be obtained:

$$\Delta\varphi = 2\pi\frac{3a^{*2}c^2}{4h^2} = \frac{3\pi a^*}{l}. \qquad \text{(D.21)}$$

Note that the Coulomb potential is just of the same form as the usual form which is derived without the gravitational field.

According to the above discussions, we shall estimate the effect of general relativity on the electron motion in the hydrogen and uranium atoms on the basis of the Bohr model.

[II-1] *Hydrogen atom*

Parameters (D.3) and (D.14) which represent the effect of general relativity are calculated for the hydrogen atom as

$$a = \frac{2GM}{c^2} = \frac{2\times 6.672\times 10^{-11}\times 1.67\times 10^{-27}}{\left(3\times 10^8\right)^2}$$
$$\approx 2.5\times 10^{-54} \ \text{m},$$

$$Q^2 = \frac{Gq^2}{4\pi\varepsilon_0 c^4} = \frac{6.67\times 10^{-11}\times\left(1.6\times 10^{-19}\right)^2}{4\pi\times 8.85\times 10^{-12}\times\left(3\times 10^8\right)^4}$$
$$\approx 1.9\times 10^{-72} \ \text{m}^2.$$

From the experiment for the electron scattering, the nuclear radius of the atom with the mass number A is approximately given by

$$r_n = 1.25\times 10^{-15} A^{1/3} \ \text{m}. \qquad \text{(D.22)}$$

In order to see the effect of general relativity, we compare r_n with r_c given by eq.(D.16). In the case of the hydrogen atom, we get

$$r_c = \frac{Q^2}{a} = \frac{1.9\times10^{-72}}{2.5\times10^{-54}} \approx 7.6\times10^{-19} \text{ m},$$

$$r_n \approx 1.25\times10^{-13} \text{ m}.$$

We see that r_c is extremely smaller than r_n in the hydrogen atom. Since the radius of the electron orbit, i.e. the Bohr radius, is much larger than r_n, a^* defined by eq.(D.17) is found to be nearly equal to a, i.e. the difference between a^* and a is very small. Substituting the Bohr radius a_B into $\bar{r}$ in eq.(D.17), we have

$$\begin{aligned} a^* &= a\left(1-\frac{Q^2}{aa_B}\right) \\ &= 2.5\times10^{-54}\left(1-\frac{1.9\times10^{-72}}{2.5\times10^{-54}\times5.29\times10^{-11}}\right) \\ &= 2.5\times10^{-54}\left(1-1.4\times10^{-8}\right). \end{aligned}$$

Thus, the difference between a^* and a is very small:

$$\frac{a^*-a}{a} \approx 1.4\times10^{-8}.$$

The precession of perihelion per revolution can be obtained:

$$(\Delta\varphi)_{\text{Hydrogen}} = \frac{3\pi a^*}{l} = \frac{3\pi\times2.5\times10^{-54}}{5.29\times10^{-11}} \approx 4.5\times10^{-43} \text{ radian},$$

where a_B is used as l. The velocity of the K-shell electron, v, and the length of the orbit, L, are respectively calculated as

$$v = c\alpha = 3\times10^{8}\frac{1}{137}\ \mathrm{m/sec},$$

$$L = 2\pi a_B = 2\pi\times5.29\times10^{-11}\ \mathrm{m},$$

where α is the fine structure constant. The period of the orbital motion is given by

$$T = \frac{L}{v} \approx 1.5\times10^{-16}\ \mathrm{sec}.$$

The required rounds for the precession of 1 ° of perihelion are given by

$$P = \left(\frac{2\pi}{360}\right)\Big/(\Delta\varphi)_{\mathrm{Hydrogen}} = 3.9\times10^{40}\ \mathrm{rounds},$$

and, on that occation, the required time can be estimated as

$$t = TP = 5.8\times10^{24}\ \mathrm{sec} \approx 2\times10^{17}\ \mathrm{years}.$$

[II-2] *Uranium atom*

As well as case [II-1], some parameters concerned with the effect of general relativity in the uranium atom (Z=92 and A=238) can be calculated as follws:

$$a = \frac{2GM}{c^2} = \frac{2\times6.672\times10^{-11}\times238\times1.67\times10^{-27}}{\left(3\times10^{8}\right)^2}$$

$$\approx 5.9\times10^{-52}\ \mathrm{m},$$

$$Q^2 = \frac{Gq^2}{4\pi\varepsilon_0 c^4} = \frac{6.67\times10^{-11}\times\left(92\times1.6\times10^{-19}\right)^2}{4\pi\times8.85\times10^{-12}\times\left(3\times10^8\right)^4}$$

$$\approx 1.6\times10^{-68}\ \ \mathrm{m}^2,$$

$$r_c = \frac{Q^2}{a} = \frac{1.6\times10^{-68}}{5.9\times10^{-52}} \approx 2.7\times10^{-17}\ \ \mathrm{m},$$

$$r_n = 1.25\times10^{-13}\sqrt[3]{238} \approx 7.8\times10^{-15}\ \ \mathrm{m}.$$

As in the hydrogen atom, r_c is extremely smaller than r_n in the uranium atom. Substituting the radius of the K-shell electron, i.e. a_B/Z, into $\bar{r}$ in eq.(D.17), we evaluate a^*:

$$a^* = a\left(1-\frac{ZQ^2}{aa_B}\right)$$

$$= 5.9\times10^{-52}\left(1-\frac{92\times1.6\times10^{-68}}{5.9\times10^{-52}\times5.29\times10^{-11}}\right)$$

$$= 5.9\times10^{-52}\left(1-4.7\times10^{-5}\right).$$

The difference between a^* and a is small and is given by

$$\frac{a^*-a}{a} \approx 4.7\times10^{-5}.$$

Therefore, the precession of perihelion per revolution can be obtained:

$$(\Delta\varphi)_{\text{Uranium}} = \frac{3\pi a^*}{l} = \frac{3\pi\times92\times5.9\times10^{-52}}{5.29\times10^{-11}} \approx 9.7\times10^{-39}\ \ \text{radian},$$

where the radius of the K-shell electron is used as l. The velocity of the K-shell electron, v, and the length of the orbit, L, are respectively calculated as

$$v = cZ\alpha = 3\times 10^8 \frac{92}{137} \text{ m/sec},$$

$$L = 2\pi \frac{a_B}{Z} = 2\pi \frac{5.29\times 10^{-11}}{92} \text{ m}.$$

The period of the orbital motion is given by

$$T = \frac{L}{v} \approx 1.8\times 10^{-20} \text{ sec}.$$

The required rounds for the precession of 1 ° of perihelion are given by

$$P = \left(\frac{2\pi}{360}\right) \Big/ (\Delta\varphi)_{\text{Uranium}} = 1.8\times 10^{36} \text{ rounds},$$

and, on that occation, the required time can be estimated as

$$t = TP = 3.2\times 10^{16} \text{ sec} \approx 1\times 10^9 \text{ years}.$$

As a result of the above classical estimates, we are led to conclude that the general-relativity effect of the Coulomb potential on the gravitational field may hardly affect the electron motion in atoms, and may be neglected safely in an actual calculation of the electronic structures in atoms and crystals by quantum theory. Therefore, the electron motion in heavy atoms may be treated by the theory of special relativity. In quantum theory, the calculation of the electronic structures in the *f*-electron systems may be carried out within the

framework of the Dirac one-electron wave equation, which is invariant under the Lorentz transformation.